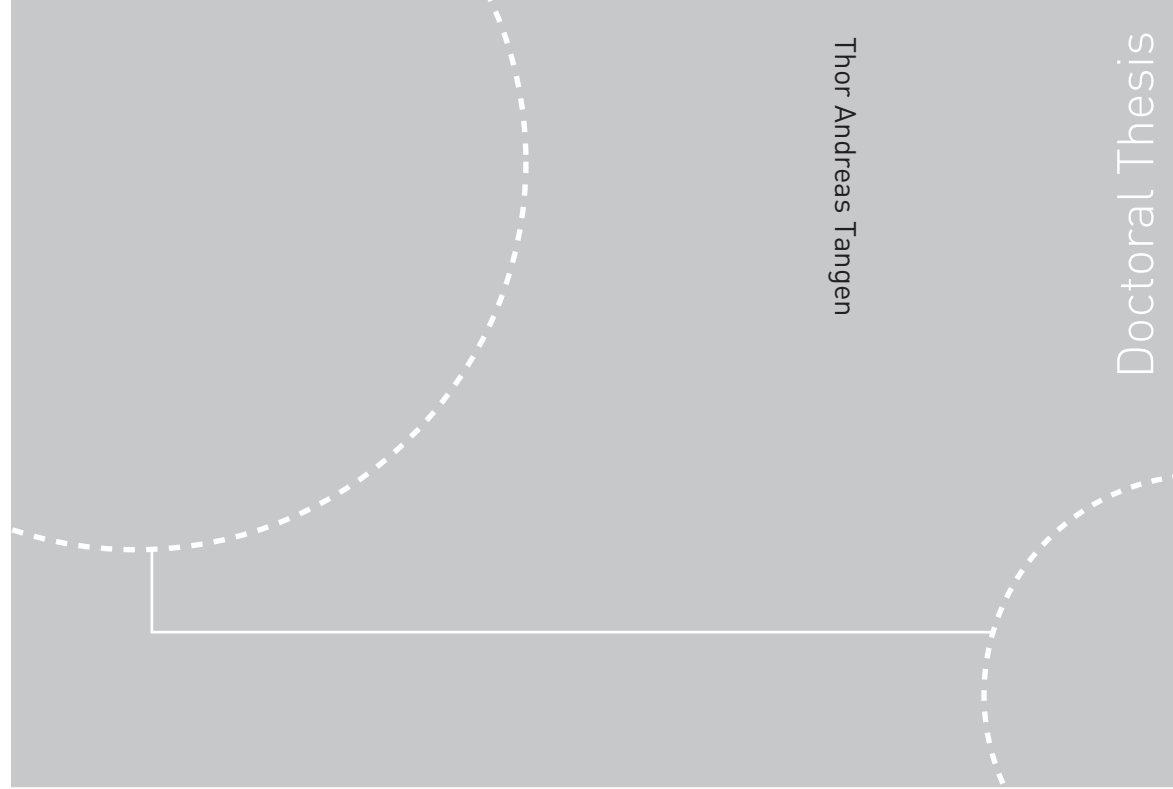


ISBN 978-82-471-2518-2 (printed ver.)
ISBN 978-82-471-2516-8 (electronic ver.)
ISSN 1503-8181



Doctoral theses at NTNU, 2010:258

Thor Andreas Tangen
**Imaging of Nonlinear-scattering
using Dual-frequency Band
Ultrasound**

Doctoral theses at NTNU, 2010:258

NTNU
Norwegian University of
Science and Technology
Thesis for the degree of
philosophiae doctor
Fakultet for Informasjonsteknologi, Matematikk og
Elektroteknikk
Institutt for Teknisk Kybernetikk

 **NTNU**
Norwegian University of
Science and Technology

 NTNU

 **NTNU**
Norwegian University of
Science and Technology

Thor Andreas Tangen

Imaging of Nonlinear-scattering using Dual-frequency Band Ultrasound

Thesis for the degree of philosophiae doctor

Trondheim, December 2010

Norwegian University of
Science and Technology
Fakultet for Informasjonsteknologi, Matematikk og
Elektroteknikk
Institutt for Teknisk Kybernetikk



Norwegian University of
Science and Technology

NTNU

Norwegian University of Science and Technology

Thesis for the degree of philosophiae doctor

Fakultet for Informasjonsteknologi, Matematikk og Elektroteknikk
Institutt for Teknisk Kybernetikk

©Thor Andreas Tangen

ISBN 978-82-471-2518-2 (printed ver.)

ISBN 978-82-471-2516-8 (electronic ver.)

ISSN 1503-8181

ITK report number: 2010-16-W

Doctoral Theses at NTNU, 2010:258

Printed by Tapir Uttrykk

Imaging of Nonlinear-scattering using Dual-frequency Band Ultrasound

Thor Andreas

Institutt for Teknisk Kybernetikk, NTNU

Hovedveiledere: Prof. Bjørn A.J. Angelsen, (ISB, NTNU)

1. Amanuensis Amund Skavhaug, (ITK, NTNU)

Finansieringskilde: Institutt for Teknisk Kybernetikk, NTNU

Ovennevnte avhandling er funnet verdig til å forsvares offentlig for graden philosophiae doctor (PhD) i teknisk kybernetikk. Disputas finner sted i Rådssalen i Hovedbygget, Gløshaugen, 17. Desember kl. 12:15.

Abstract

The work presented in this thesis is focused on developing a method for imaging of nonlinear scattering from stiff particles using dual-frequency band pulses. The pulse complexes are comprised of a low-frequency manipulation pulse and a high-frequency imaging pulse where the two pulses overlap in time and there is a frequency relationship of 1:8-10. It may be shown that the polarity of the nonlinear scattering follows the polarity of the low-frequency pulse, while linear scattering does not. By transmitting two such dual-frequency band pulses in each beam direction where the polarity of the low-frequency pulse is inverted from the first to the second, nonlinear scattering may be detected. The low-frequency pulse not only manipulates the scattering but also the propagation of the high-frequency imaging pulse. These nonlinear propagation effects will mask the nonlinear scattering and must be corrected for in order to suppress the linear scattering and detect the nonlinear scattering.

In the first paper of this thesis, the nonlinear propagation effects using confocal low-frequency and high-frequency beams are investigated in a water tank setup. A dual-frequency band annular array, where the low-frequency element is placed behind the high-frequency element, to form a stack, was used. When the high-frequency pulse is short compared to the low-frequency pulse period, the nonlinear propagation effects can be approximated by a nonlinear propagation delay and frequency shift. It is shown how the delay and frequency shift increases close to linearly with increasing manipulation pressure and how axis the profiles of the high-frequency beam are affected. On transmit, the size relationship between the low and high-frequency apertures can be varied, and it is shown how the nonlinear propagation effects is dependent on the array setup.

By transmitting an unfocused low-frequency beam together with a focused high-frequency beam, the position of the high-frequency pulse relative to the low-frequency pulse can be kept close to constant over the whole imaging region. By placing the imaging pulse at the peak of the manipulation pulse, the frequency shift due to nonlinear propagation can be minimized. In the second paper, the suppression of linear scattering using such a beam setup and only correcting for the propagation delay is investigated. Applying a low-frequency pressure of 85 to 500 kPa, the linear scattering could be suppressed 35 to 17 dB. It is shown that there is an amplitude difference between the first and second received pulse which is due to diffraction differences of the first and second beam. Since the low-frequency beam is unfocused, the manipulation pressure will vary over the focused high-frequency beam and distort the spherical

focusing. This distortion will be different for the first and second beam and produce different diffraction of the two beams, which will yield an amplitude difference. Frequency shift due to nonlinear propagation will also affect the diffraction but it is indicated that the nonlinear aberration is the dominating factor.

In the third paper three different beamforming strategies for dual-frequency band imaging is investigated; 1. Focused low freq. + Focused high freq., 2. Unfocused low freq. + Focused high freq. and 1. Unfocused low freq. + Unfocused high freq. The nonlinear propagation delay and frequency shift are estimated and predicted based on the estimated low-frequency manipulation pressure experienced by the high-frequency pulse. There is good accordance between the estimated and predicted values until diffraction becomes significant. When diffraction becomes significant, differences in diffraction between the first and second pulse will also introduce a frequency shift and delay other than that generated by the nonlinear manipulation pressure. Differences in the pulse form of the first and second pulse is thus not only due to manipulation of the propagation of the high-frequency pulse by the low-frequency, but also by differences in diffraction.

The nonlinear propagation and scattering are generated by equal processes but are different in the way that nonlinear propagation is an accumulative effect while scattering is a local effect. In the last part of the thesis the difference between nonlinear propagation and scattering is investigated using simulations, where the bandwidth of the high-frequency pulse relative to the center frequency of the manipulation pulse is varied. It is shown that when the high-frequency pulse is shorter in time than one period of the low-frequency pulse, the nonlinear propagation and scattering becomes different and the nonlinear scattering can be detected if the nonlinear propagation is corrected for.

The correction of nonlinear propagation can be in the form of a filter, and a method for estimating this filter is also presented in the last part. Based on statistical analysis of the filter, it is shown that the average suppression of linear scattering using the proposed correction filter, is dependent on the homogeneity of the relation between the first and second pulse over the receive beam. Said in another way; if this relation is not constant over the receive beam, the optimal correction for a given signal segment is dependent on the unknown distribution of scatterers within the beam.

The level of suppression of linear scattering using the proposed filter method will be dependent on the transmit beam setup. A simulation study where the effect of aperture size relationship between the low- and high-frequency beams and f-number of the high-frequency beam on the level of suppression of linear scattering is presented. In order to achieve a high degree of homogeneity, the diffraction of the HF and LF beams should be equal, which is not trivial to achieve in a medium with attenuation. Choosing the aperture sizes in order for the fresnel numbers to be equal for the two beams was thought to yield the optimal setup, but as attenuation affects the low and high-frequency pulses differently, this is not necessarily true. The level of suppression of linear scattering increases when the the high-frequency aperture is increased, making the beam narrower, but the low-frequency aperture must also be increased accordingly.

Preface

This thesis has been submitted in partial fulfillment of the requirements for the degree *philosophiae doctor* (PhD) at the Faculty of Informatics, Mathematics and Electronics of the Norwegian University of Science and Technology (NTNU). The research was funded by the Department of Engineering Cybernetics, NTNU, and was carried out under the supervision of Assistant Professor Amund Skavhaug at the Department of Engineering Cybernetics, NTNU, and Professor Bjørn A. J. Angelsen at the Department of Circulation and Medical Imaging, NTNU.

Acknowledgments

First of all I would like to thank my supervisors, Professor Bjørn A. J. Angelsen and Assistant Professor Amund Skavhaug for guiding me through the work with my PhD.

Professor Angelsen's support has been invaluable to my work. His knowledge, energy, optimism, patience and belief in me have been of great importance to me and for my work. He is always available for discussion, and has always respected my opinion and listened to me. I am very grateful to have had the opportunity to work with him.

The support of Assistant Professor Amund Skavhaug has been of great importance in completing this work. He has made sure that I at any time have kept my focus on working towards the goal of finishing my PhD on time. He follows up his students and makes sure they maintain progress, while also acknowledging the importance of having a life outside the office.

Researcher Svein-Erik Måsøy is besides Professor Angelsen, the person who I have worked the closest with during my PhD. His interest in my work and positive spirit has been very important to me, especially in times of frustration and despair. Our discussions, though sometimes quite heated, has been very fruitful and of great importance to my work.

I would also like to thank Assistant Professor Tonni F. Johansen for the support in the lab and for fruitful discussion. He is an incredible source of knowledge and is always available for discussion and explaining the mysteries of ultrasound.

It has been a great experience to get to work with the group of Professor Angelsen, and I would like to thank the rest of the group, Rune Hansen, Øyvind Standal, Halvard Kaupang, Tarjei Rommetveit, Jochen Deibele and Sven-Peter Näsholm, for their contributions and feedback during my PhD work. It has been a pleasure working with such great individuals, with their knowledge and interest for medical ultrasound.

During my PhD work I have had the pleasure of co-supervising several master students; Johan Svanem, Mercy Afadzi, Åsmund Herikstad, Jørgen Grythe and Bastien Denarie. It has been a great experience to work with these students as they have shown great interest in the work and produced interesting and very useful results. This work has been very interesting and important to me.

My family and friends are of great importance to me and I would not have been able to carry out this work without their support and encouragement. Thank you for listening to my frustration and always being positive, especially when I am not.

I would also like to thank Kris Dickie at Ultrasonix Medical Corp and Magnus Andersen at Norbit for their help and support in developing the real-time dual-frequency band system.

Last I would like to thank my colleagues at the Department of Circulation and Medical Imaging for providing a positive and good working environment.

Contents

Introduction	11
1.1 Nonlinear ultrasound imaging	12
1.2 SURF imaging	15
1.3 Imaging of Micro Calcifications	17
1.4 Summary of thesis	19
1.5 Contributions	24
References	27
A Nonlinear propagation acoustics of dual-frequency wide-band excitation pulses in a focused ultrasound system	33
A.1 Introduction	34
A.2 Theory	36
A.2.1 Dual-frequency excitation pulses	36
A.2.2 Nonlinear wave equation in a homogeneous medium	36
A.2.3 SURF imaging using a focused ultrasound system	38
A.3 Method	39
A.3.1 Annular array	39
A.3.2 Pulse-Echo Lab system	40
A.3.3 Water tank setup	41
A.3.4 Data processing	42
A.4 Results	42
A.5 Discussion	45
A.6 Conclusion	50
A.7 Acknowledgements	50
References	51
B Suppression of linear scattering for a dual-frequency band imaging technique	55
B.1 Introduction	56
B.2 Theory	57
B.2.1 Nonlinear wave equation	57
B.2.2 Dual-frequency propagation	59
B.2.3 Signal Model	61

B.2.4	Delay estimation	61
B.3	Methods	62
B.3.1	Scanner	62
B.3.2	Transmit beam setup	63
B.3.3	Measurements	64
B.3.4	Simulations	64
B.3.5	Processing	65
B.4	Results	65
B.5	Discussion	67
B.6	Conclusions	70
	References	73
C	Comparison of beamforming strategies for dual-frequency band imaging using a large frequency separation	75
C.1	Introduction	76
C.2	Theory	77
C.2.1	Nonlinear wave equation	77
C.2.2	Dual-frequency propagation	78
C.3	Methods	80
C.3.1	Scanner	80
C.3.2	Transmit beam setup	81
C.3.3	Water tank Measurements	82
C.3.4	Processing	82
C.4	Results	83
C.5	Discussion	89
C.6	Conclusion	96
	References	99
D	Imaging of Nonlinear Scattering using Dual-frequency Band Ultrasound	103
D.1	Introduction	103
D.2	Theory	104
D.2.1	Nonlinear wave equation	104
D.2.2	Nonlinear propagation	105
D.2.3	Nonlinear scattering	107
D.2.4	Received Signal Model	109
D.2.5	Correction of nonlinear propagation	110
D.3	Differentiating nonlinear scattering from nonlinear propagation	113
D.3.1	Introduction	113
D.3.2	Simulations	113
D.3.3	Processing	114
D.3.4	Results	115
D.3.5	Discussion	116
D.3.6	Conclusion	120

D.4 Effect of beamforming parameters on accuracy of nonlinear propagation correction	120
D.4.1 Introduction	120
D.4.2 Simulations	120
D.4.3 Processing	122
D.4.4 Results	123
D.4.5 Discussion	129
D.4.6 Conclusion	131
References	133

Introduction

Thor Andreas Tangen

Department of Engineering Cybernetics, NTNU

Among the general public, medical ultrasound is associated with imaging of the unborn child in the womb of the mother, and imaging of the human heart. Though these were some of the first applications of medical ultrasound, it is now a part of routine diagnostic practice in many fields of medicine. The major strength of ultrasound is its ease of use, relatively low cost and real-time image acquisition, *i.e.* the sonographer is provided the image while scanning the patient.

In screening for breast cancer, x-ray mammography is the primary tool, while ultrasound is used in the follow up of suspicious findings in the mammograms. Micro calcifications detected in mammography are diagnostic indicators of pathological changes in the breast [1]. Biopsies from the suspicious areas are performed where ultrasound is used for guidance, since the biopsy needle can be visualized clearly in the ultrasound image. Imaging of micro calcifications using ultrasound is crucial for achieving a high degree of accuracy in the biopsy procedure. As the breast is composed of heterogenous tissue, differentiating the micro calcifications from other specular reflectors in the image can be difficult, especially if the calcifications are not associated with a mass [2]. In women with dense breast, x-ray mammography fails to detect micro calcifications, making MR and ultrasound the primary tool for investigating these patients.

Nonlinear phenomena caught the attention of the ultrasound community after the publications of Carstensen and Muir [3, 4] in 1980. Tissue harmonic imaging, which utilizes the nonlinear accumulation of harmonics in the forward propagating pulse in order to suppress pulse reverberations, is one of the most important developments in diagnostic ultrasound since the introduction of Doppler ultrasound. Since then, little development within nonlinear ultrasound has been seen except for some limited interest in dual-frequency band ultrasound imaging.

Aim of thesis:

The work presented in this thesis is devoted to investigate how nonlinear scattering from stiff particles embedded in soft tissue can be detected using dual-frequency band ultrasound. In order to achieve this goal, the nonlinear propagation phenomena of

dual-frequency band ultrasound and their effect on suppression of linear scattering, as well as the effect of transmit beamforming must be well understood.

In the introductory chapter a short review of nonlinear ultrasound imaging is given, where the major applications of nonlinear ultrasound is presented. Further, a dual-frequency band imaging technique developed at the Department of Circulation and Medical Imaging, NTNU, coined SURF imaging is presented. This imaging technique can be used to suppress reverberation noise and image nonlinear scattering from ultrasound contrast agents and possibly stiff particles embedded in soft tissue, like micro calcifications. A short review of what has been presented in the literature on imaging of micro calcifications then follows, before the contributions of this thesis are presented.

1.1 Nonlinear ultrasound imaging

In the nonlinear regime, the relative volume compression of tissue is modeled to have a second order relationship to the applied pressure [5]

$$\frac{\partial V}{\Delta V} \approx (1 - \beta_n \kappa p) \kappa p \quad (1.1)$$

where ∂V is the volume compression of the material volume ΔV , κ is the compressibility, p is the applied pressure, and β_n is the nonlinearity parameter of the material. Using this model for the relative volume compression, the nonlinear wave equation for heterogenous tissue becomes

$$\underbrace{\nabla^2 p(\underline{r}, t) - \frac{1}{c_0^2(\underline{r})} \frac{\partial^2 p(\underline{r}, t)}{\partial t^2} + \frac{\beta_{na} \kappa_a}{c_0^2(\underline{r})} \frac{\partial^2 p^2(\underline{r}, t)}{\partial t^2}}_{\text{Nonlinear propagation}} - \underbrace{h_p \otimes_t \frac{1}{c_0^2(\underline{r})} \frac{\partial^2 p(\underline{r}, t)}{\partial t^2}}_{\text{Absorption}} = \underbrace{\frac{\sigma_l(\underline{r})}{c_0^2(\underline{r})} \frac{\partial^2 p(\underline{r}, t)}{\partial t^2} + \nabla(\gamma(\underline{r})) \nabla p(\underline{r}, t)}_{\text{Linear scattering}} - \underbrace{\frac{\sigma_n(\underline{r})}{2c_0^2(\underline{r})} \frac{\partial^2 p^2(\underline{r}, t)}{\partial t^2}}_{\text{Nonlinear scattering}} \quad (1.2)$$

where $p(\underline{r}, t)$ is the pressure pulse at spatial position \underline{r} , $c_0^2(\underline{r}) = \frac{1}{\rho_a(\underline{r}) \kappa_a(\underline{r})}$ is the linear propagation velocity, ρ is the mass density and h_p represents frequency dependent attenuation. The spatial variation of the material parameters can be modeled as an average, a , and fluctuating, f , component, where the average is taken over a few wavelengths

$$\begin{aligned} \kappa(\underline{r}) &= \kappa_a + \kappa_f(\underline{r}) \\ \rho(\underline{r}) &= \rho_a + \rho_f(\underline{r}) \\ \beta(\underline{r}) &= \beta_{na} + \beta_{nf}(\underline{r}) . \end{aligned} \quad (1.3)$$

The scattering coefficients are then given as

$$\begin{aligned}\sigma_l(\underline{r}) &= \frac{\kappa_f(\underline{r})}{\kappa_a(\underline{r})} \\ \gamma(\underline{r}) &= \frac{\rho_f(\underline{r})}{\rho(\underline{r})} \\ \sigma_n(\underline{r}) &= \{2\beta_{na}(2 + \sigma_l)\sigma_l + \beta_{nf}(1 + \sigma_l)^2\} \kappa_a.\end{aligned}\tag{1.4}$$

The squared pressure term on the left hand side of Equation (1.2) models the generation of nonlinear forward propagation effects. The squaring of the pressure generates harmonics of the center frequency of the forward propagating pulse. In Figure 1.1(b), the pulse in figure 1.1(a) has propagated a distance of 20 mm in water, and the nonlinear effect is clearly seen. The generation of nonlinear propagation effects is accumulative and thus increases with depth. Attenuation increases with frequency which counteracts the harmonic build-up.

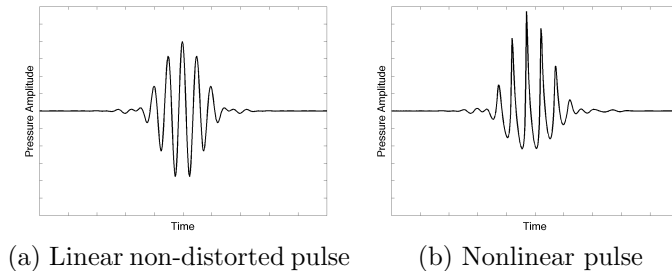


Figure 1.1: Nonlinear distortion

In harmonic imaging, the accumulation of higher harmonics with depth is used to suppress reverberation noise and is most commonly known as tissue harmonic imaging (THI) [6]. THI is based on the assumption that most of the reverberations originates from the body wall which consists of layers of muscle and fat. For a focused transmit beam, the pressure amplitude is low in the near field, which means that there is limited accumulation of harmonics in this region. The reverberation echoes which has their first scattering in the near field will contain low level of harmonic components, compared to the echoes with their first echo in the focal zone of the transmit beam. The generation of harmonics after the first scattering incident assumed to be insignificant. By filtering out the higher harmonics on receive, the contrast between the reverberations originating from the body wall and echoes from the region of interest will be enhanced. Since attenuation increases with frequency, penetration is a problem for THI. In addition, the transducers must have a high bandwidth to be able to transmit f_c and receive the higher harmonics, which limits the sensitivity of the method.

While THI utilizes the accumulation of nonlinear effects, contrast enhanced ultrasound (CEUS) utilizes the local nonlinear scattering from ultrasound contrast agents in order to image micro-vascularization. The ultrasound contrast agents are gas filled

micro bubbles with diameters in the range 1-6 microns, and they typically have resonance frequencies in the range 22 to 2 MHz. Commercially available contrast agents has a dominant diameter distribution at around 5-6 microns, which correspond to resonance frequencies at about 2 to 3 MHz [7]. If insonified at, or near, their resonance frequency, the bubbles will oscillate wildly, generating harmonics of the insonified frequency. The tissue does not respond in the same way but forward propagation will also accumulate harmonics which will decrease the specificity.

In a method known as Pulse Inversion (PI) [8], two pulses are transmitted in each direction with the second pulse being the inverse of the first. Then by adding the two received pulses, the linear scattered signal at f_c will add destructively while the harmonic signal at $2f_c$ will add constructively, enhancing the contrast-to-tissue ratio (CTR). Lately, more sophisticated methods using both PI and amplitude modulation (AM) schemes has been proposed to further increase the CTR [9]. In AM, three or more pulses are transmitted in each direction, where the phase and/or amplitude of the transmitted pulse is altered over the sequence. This method utilizes the fact that the third order nonlinearities has a signal component at the third harmonic as well as the fundamental frequency [10]. By transmitting a sequence of pulses with different amplitude and phase, the third order nonlinearities can be extracted while suppressing the linear signal components. Since the nonlinear signal components are in the fundamental band one can utilize the full sensitivity of the transducer compared to PI.

Over the last decade several groups have investigated the use of dual-frequency band methods for CEUS to improve the detection of micro bubbles to that of AM and PI. AM and PI methods works well for transmit frequencies close to that of the resonance frequency of the bubbles, while the dual-frequency methods aim to increase the imaging frequency. One of the first to propose such a method was Deng *et. al.* [11] and this has later been investigated by several groups [12–15]. In general these methods use a low-frequency pulse to manipulate the bubble while using a high-frequency pulse to image the bubble. The two pulses are overlapping in time, and the low-frequency pulse manipulates the radius and scattering properties of the bubble while the scattering from tissue is not affected in the same way. Dual-frequency band methods also utilizes other nonlinear effects than the resonant behavior of the bubble, thus making CEUS for higher imaging frequencies possible [13]. The frequency difference between the low-frequency and high-frequency pulse for these methods is in the range 1:7-20.

Dual-frequency band methods has also been applied for estimating the nonlinear parameter B/A in tissues and liquids [16–19]. The B/A parameter varies over the range 4 (blood) to 6.2 (fat) [20] in biological tissue. In Refs. [16, 17], the amplitude of the signal component at the difference frequency of the low and high-frequency pulses is used to estimate the nonlinearity parameter. They propose a computed tomography method in order to be able to correct for the attenuation. Fukukita *et. al.* [19] utilizes the compression/expansion of the high-frequency pulse which travels on the negative or positive spatial gradient of the low-frequency pulse in order to estimate the nonlinearity parameter. They propose a through transmission method, and also here the attenuation must be corrected for. None of the proposed methods has made

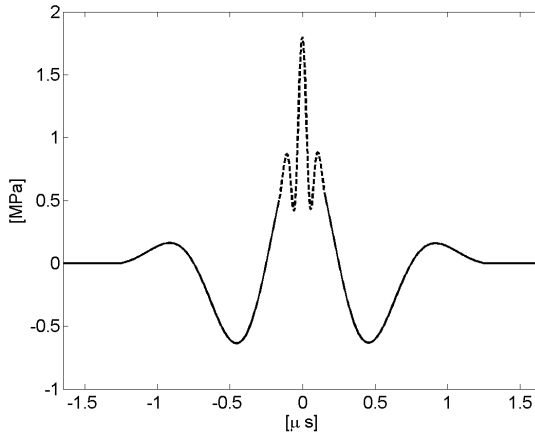


Figure 1.2: SURF pulse complex consisting of a high-frequency imaging pulse(dashed) and a low-frequency manipulation pulse(solid)

it into the clinic.

In vibroacoustography [21–23], two confocal beams with slightly different frequency (10-50 kHz) is used to image the mechanical properties of tissue. The two beams overlap in the focal region, and the nonlinear interaction between the two beams generates an oscillation at the difference frequency. The emitted acoustic signal due to this oscillation is then recorded using a sensitive hydrophone. The phase and amplitude of the recorded signal is dependent on the mechanical properties of the tissue and a qualitative image of the tissue stiffness can be generated. In order to acquire a complete 2D image, a raster scan over the region of interest must be performed. The detection of micro calcifications in breasts and imaging of calcified arteries are among the numerous suggested applications of this technique.

1.2 SURF imaging

SURF (Second order Ultrasound Field) imaging is a dual-frequency band technique developed at the Department of Circulation and Medical Imaging at the Norwegian University of Science and technology [24]. The method utilizes pulse complexes consisting of a low-frequency (LF) manipulation pulse and a high-frequency (HF) imaging pulse. An example pulse complex is shown in Figure B.1, where the HF pulse is centered at the peak of the LF pulse oscillation. The frequency relationship between the HF and LF is in the range 1:8-10. One or more pulse complexes are transmitted in each beam direction where the phase and/or amplitude of the LF pulse is altered over the pulse sequence in order to achieve the wanted nonlinear effect. The LF manipulation pulse manipulates the forward propagation and local scattering of the HF imaging pulse, and applications of SURF imaging utilizes one or both of these effects.

The nonlinear interaction between the HF and LF pulse will generate signal components at the sum ($f_{HF} + f_{LF}$) and difference ($f_{HF} - f_{LF}$) frequencies of the HF and LF, where the generated signal components will be dependent on the phase and amplitude of the LF pulse. In forward propagation, the nonlinear effects are accumulative, while for scattering they are a local effect. When the bandwidth of the HF pulse is large compared to the center frequency of the LF pulse, the nonlinear forward propagation effects can be approximated to be a propagation delay and compression/expansion of the HF pulse relative to a non-manipulated HF pulse. The average LF pressure over the HF pulse, p_{ma} , will generate an accumulative nonlinear propagation delay

$$\tau_n(z) = - \int_0^z \frac{ds}{c_0} \beta_n \kappa p_{ma}(s). \quad (1.5)$$

The average spatial LF pressure gradient Δp_m over the HF pulse will after propagating a distance Δz , produce a change in wavelength of the HF pulse of

$$\Delta \lambda_{HF}(\Delta z) = c_0 \beta_n \kappa \Delta p_m \Delta z, \quad (1.6)$$

which will produce a change in center frequency of

$$f_{HF}(z + \Delta z) = \frac{\lambda_{HF}}{\lambda_{HF} + \Delta \lambda_{HF}} f_{HF}(z) \quad (1.7)$$

in a loss-less medium. When the center frequency changes, so does diffraction of the beam. HF pulses transmitted at different phases and amplitudes of the LF pulse will then have different diffraction, introducing pulse form differences other than a pure delay and frequency shift. Imaging techniques based on the SURF imaging method has been developed for suppression of pulse reverberations [25] and imaging of contrast agents [12, 14].

For reverberation suppression, the nonlinear forward propagation effects are used to suppress reverberations originating from strong inhomogeneities in body wall. By careful design of the dual-frequency band transmit beams, the nonlinear manipulation of the HF pulse by the LF pulse, can be limited for shallow depths, while increasing rapidly after a certain depth. By transmitting two pulse complexes in each beam direction where the phase of the LF is shifted 180 degrees from the first to the second pulse, and then subtracting the two received signals, pulse reverberations can be suppressed. Echoes with their first reflection close to the transducer will have experienced little manipulation and will thus be strongly suppressed. This is somewhat similar to THI, but here imaging is performed at the fundamental frequency and there is greater flexibility in the design of transmit beams.

For imaging of ultrasound contrast agents, the local nonlinear scattering is used in order to increase the contrast-to-tissue ratio. In this application two pulse complexes are transmitted in each beam direction where the LF phase is shifted 180 degrees and the applied LF pressure is in the range 50-100 kPa for a 1:10 MHz setup. After propagating 20 mm, the nonlinear propagation delay of the HF pulse will be in the range 3-5 ns between the received signal from the first and second pulse complex. Since the pressure is low, the frequency shift is neglected and only the nonlinear propagation

delay is estimated and corrected for before the two received signals are subtracted. The LF pulse, which typically has a frequency below the resonance frequency of the bubble, manipulates the radius of the bubble which changes its resonant behavior. The bubble is thus imaged by the HF pulse at two different states, which will create a difference in the backscattered signal from the two pulses and provide a means of detection of the bubble since the surrounding tissue is not affected in the same way.

Another type of nonlinear scattering stems from inhomogeneities in the nonlinearity parameters, β_n , κ . From Equation (1.2) and (1.4) it is seen that strong inhomogeneities will generate nonlinear scattering. Such inhomogeneities is seen *e.g.* for stiff particles embedded in soft tissue, like micro calcifications. The local nonlinear scattering will generate signal components at the sum and difference frequencies of the LF and HF due to the nonlinear interaction between the LF and HF pulse. The polarity of the nonlinear scattering will thus be dependent of the polarity of the LF pulse and the amplitude of the scattering will be proportional to the LF pressure amplitude. For a LF pressure of 1MPa, the nonlinear scattering from a micro calcification particle is indicated to be 30 dB lower than that from a muscle/fat interface. Thus, in order to achieve significant nonlinear scattering, a high LF pressure should be applied. The high manipulation pressure will generate significant nonlinear propagation effects which will have to be estimated and corrected for in order to detect the nonlinear scattering. The work presented in this thesis focuses on how the nonlinear scattering can be imaged using SURF imaging.

1.3 Imaging of Micro Calcifications

The detection of micro calcifications is of great importance in the early diagnosis of breast tumors. Worldwide, breast cancer is the second most common type of cancer after lung cancer [26] and the fifth most common cause of cancer deaths [27], and in 2005 caused 502,000 deaths worldwide (7% of cancer deaths; almost 1% of all deaths) [27]. Micro calcifications are associated both with benign and malignant tumors and their size is less than 500 μm . Calcifications of greater size are coined macro calcifications and are usually not associated with cancer. Calcifications are also found in other types of cancer like in the thyroid and prostate gland [28, 29] though they are not associated with malignancy for prostate cancer [30].

The only accepted imaging modality for screening for breast cancer to date is x-ray mammography [31]. Many countries have screening programs for women over the age of 40 [32], where the women are screened annually or semi-annually. The micro calcifications appear as white dots on the mammography image, and based on the shape, number and distribution, some indication of malignancy can be given, but usually biopsies are needed for confirmation. There exist several methods for performing biopsies using x-ray, like stereotactic and wire localized biopsy, but in an increasing number of cases ultrasound is used for guiding the biopsy [33]. Ultrasound is arguably the most accurate method of performing core needle biopsies. The needle is shown in the image in real-time, providing better feedback on position and the patient is not exposed to unnecessary x-ray radiation associated with mammographic biopsy

techniques [34, 35].

Ultrasound has been suggested as an alternative screening method to mammography. The criteria for a screening method is that it must have high sensitivity for small breast cancers, high specificity and be cost effective, safe and acceptable to the population being screened [36]. Also, a good screening method would reduce morbidity while having a low false alarm rate and being relatively cheap [37]. To replace mammography ultrasound has to show at least the same sensitivity for small and pre-invasive breast cancers, including detection of clinically occult solid mass lesions, architectural distortions and micro calcifications [36].

Detection of micro calcifications by mammography in young women is made difficult by the radiologically dense breast, thus limiting the usefulness of x-ray mammography. For this group of women, ultrasound is the imaging method of first choice [38, 39].

The feasibility of detecting micro calcifications using conventional B-mode imaging has been investigated over the last 20 year both *in vivo* [2, 40, 41] and *in vitro* [42] as well as in simulations [43, 44].

In [42] glass beads in the size range 110-460 μm are embedded in agar solutions with varying level of ambient background scattering. It is shown that when the glass beads are situated in low echogenic areas, glass beads of 110 μm can be detected robustly. When the beads are situated in areas with a higher level of backscatter, even the 460 μm could not be detected. The scattered signal from the glass beads are masked by the scattering from the background since it exhibits the same echogenicity. This demonstrates one of the major limitations with conventional ultrasound; speckle noise reduces the ability to detect micro calcifications. Though linear arrays with higher frequency and larger bandwidth in addition to new methods for speckle reduction has been introduced since this study, micro calcifications are not detected robustly when the particles are not localized in low hypo-echoic or iso-echoic masses [2].

In [41], 84 patients with breast cancer where investigated with mammography and ultrasound. In this study it is reported a sensitivity of 95%, specificity of 88% and accuracy of 91% in detecting micro calcifications by ultrasound, using mammography as a gold standard. The patients in this study had malignant tumors and the calcifications where associated with hypo-echoic masses, which facilitates the detection of the calcifications by ultrasound.

While the results in [41] are encouraging, the study performed by Soo *et. al.* [2] is not as positive; Only 23% of the calcifications detection by mammography where detected by ultrasound. In this study the patients had calcifications detected by mammography, without identifiable masses. In the cases where the calcifications where detected by ultrasound they where located in hypo-echoic (95%) and iso-echoic(5%) masses and all but one of the ultrasound guided biopsy procedures for these cases where considered successful.

From these studies it is evident that conventional B-mode imaging lacks the ability detect micro calcifications when they are not associated with a mass or located in hypo-echoic and iso-echoic areas.

Over the last decade a method known as vibro-acoustography [21–23] has been proposed as method for imaging of micro calcifications in the breast. In [45] 74 excised tissue samples was imaged with vibro-acoustography and the calcifications where

detected in 78.4% of the cases. In most of the cases (81.3%) where the calcifications were missed, the image quality was graded as fair, while it was graded good for most of the cases (72.4%) where the calcifications were detected. Problems in tissue sample preparation or image artifacts degrade image quality. Though the method shows promising results, the scanning time of current implementations is 7 minutes for a 5x5 cm area, which should be minimized for the method to be suited for routine clinical application [46]. The method also suffers from artifacts due standing waves of the transmitted CW beams and multipath travel of the emitted acoustic signal. Methods for decreasing the scan time and suppressing multipath signals has been proposed [47, 48].

Toshiba Medical Corporation (Otagawa, Japan) has recently released a method coined MicroPureTM. The method is not published, but to the author's knowledge a method coined DTHI [49] is used to suppress speckle and then an advanced image filter is used in order to detect the calcifications. DTHI utilizes dual-frequency pulse complexes with a relatively small difference between the two frequencies, *e.g.* 6+9 MHz, and then the image is formed using the signal components at the sum and difference frequencies. To the author's knowledge, no clinical studies has been presented on this method to date.

1.4 Summary of thesis

This thesis focuses on the investigation and understanding of nonlinear propagation effects and how they affect the suppression of nonlinear scattering. It is also shown how nonlinear scattering is different from nonlinear propagation.

At the time when the work with this thesis started, the first dual-frequency band annular array prototype based on a dual stack design was available. This array was designed to replace the annular arrays where the LF element was a confocal ring placed outside the HF elements. This new array was used to investigate the nonlinear propagation effects in a focused system where the LF and HF was transmitted from a common surface. Until then, the length of the HF pulse was assumed to be adequately short compared to the LF pulse period, so that nonlinear propagation effects could be approximated as a nonlinear propagation delay. Especially in the application of imaging ultrasound contrast agents, where the manipulation pressure is low, the nonlinear propagation effects has been approximated to be a propagation delay.

The first measurements with this new array showed that the nonlinear propagation effects would, in addition to the nonlinear delay, produce significant compression/expansion of the HF pulse, *i.e.* a frequency shift compared to a non-manipulated HF pulse. The results from these measurements are presented in Paper A. It is also shown that the size relationship of the LF and HF apertures affect the accumulation of nonlinear propagation effects.

In the time after these findings, work was initiated to build a new dual-frequency band system with linear arrays and real time imaging. Until then, a GE VingMed System5 (GE VingMed, Horten, Norway) with annular arrays was used to record data which was later processed off line. The research group which the author is a member

of, has in collaboration with Ultrasonix Medical Corp. (Vancouver, BC, Canada) and Norbit (Trondheim, Norway) modified a Ultrasonix SonixRP system to make it capable of performing real-time dual-frequency band imaging. This modification work has included design, manufacturing and integration of a low-frequency transmitter, design of dual-frequency band linear arrays and implementation of signal processing algorithms. The author has been responsible for implementation of the signal processing algorithms specific to the dual-frequency band technique as well as standard signal processing routines like IQ demodulation, envelope detection and compression and transmit beamforming for the low-frequency pulse. The software had to be integrated with the existing imaging software on the scanner, which was achieved through a plug-in interface implemented by Ultrasonix. The author spent 1300 hours during the PhD period on implementation and integration of the software as well as general testing and getting the system ready for clinical trials.

When this new system was ready for use, one would like to determine what kind of suppression of linear scattering could be achieved using an unfocused LF beam together with a focused HF beam. Such a setup would provide little variation of the LF pressure over the HF imaging region and would be interesting for imaging of nonlinear scattering both from contrast agents and stiff particles in soft tissue. These investigations showed that the suppression of linear scattering decreased with increasing LF manipulation pressure and that in addition to the nonlinear delay there was a significant amplitude difference between the first and second pulse. This amplitude difference was thought to be caused by varying LF manipulation pressure over the HF beam since they were not confocal. As the LF pulse manipulates the speed of sound experienced by the HF, this variation can be seen as a kind of aberration. The aberration in this beam setup distorts the spherical focusing and thus shifts the focus of the beam. Since the LF is inverted from the first to the second pulse, the change in focus will be different and the diffraction of the beams becomes different. The suppression achieved with this kind of setup would not be adequate for imaging nonlinear scattering from stiff particles. The results from these measurements are presented in Paper B.

These findings triggered investigations on different beamforming strategies for dual-frequency band imaging. Three different strategies were investigated in the water tank; 1. Focused LF + Focused HF, 2. Unfocused LF + Focused HF and 3. Unfocused LF + Unfocused HF. It was shown that the nonlinear propagation effects would make the diffraction of the first and second pulse different, it is not just the accumulation of nonlinear propagation effects which contributes to the pulse form distortion. The relation between the LF pressure and pressure gradient experienced by the HF pulse and the nonlinear propagation delay and frequency shift respectively, is demonstrated. The delay and frequency shift could be predicted well until the diffraction becomes significant. The results from these measurements are presented in Paper C.

The investigations so far indicated that correcting only for the nonlinear propagation delay does not provide adequate suppression of nonlinear scattering, one should also correct for pulse form distortion due to accumulated nonlinear propagation effects other than delay, and differences in diffraction. These differences between the first and second pulse can be modeled as a filter, and a method for estimating this filter based on a minimum least squares method was proposed. When analyzing the

statistical properties of this filter, it was discovered that in order to achieve optimal suppression using the proposed estimation method, the relationship of the frequency spectrums between the first and second pulse should be constant over the HF beam. A simulation study was then initiated with the purpose to investigate how the transmit beams should be designed in order to satisfy the requirements set by the estimation method, and to investigate what level of suppression could be achieved with existing transducers. This simulation study is presented in Paper D.

The process which generates the nonlinear propagation effect and the nonlinear scattering is equal according to the nonlinear wave equation for heterogenous tissue. The difference is that the nonlinear propagation effects are accumulative while the nonlinear scattering is a local effect. In Paper D it is shown through simulations how these two effects are different and what conditions must be satisfied for the two effects to be separable.

Paper A: Nonlinear propagation acoustics of dual-frequency wide-band excitation pulses in a focused ultrasound system

In this paper an annular two layer dual-frequency band array is demonstrated. The nonlinear propagation effects in a focused ultrasound system are demonstrated *in vitro* in a water tank setup. When the HF pulse is short compared to the LF pulse the nonlinear propagation effects can be approximated by a nonlinear propagation delay and a frequency shift. The average LF pressure over the HF pulse produces a delay while the LF pressure gradient produces a compression/expansion of the HF pulse, i.e. a shift in frequency. It is shown how the nonlinear propagation effects increase with increasing LF pressure, and how the accumulation of propagation effects are dependent on the array configuration.

The work was a joint effort with Post. Doc. Svein-Erik Måsøy. Svein-Erik Måsøy conducted most of the writing while the experiments theoretical background was done in collaboration between Svein-Erik Måsøy and the author.

This paper was published in the Journal of the Acoustical Society of America (JASA), Vol 128, No. 5, 2010.

Paper B: Suppression of linear scattering for a dual-frequency band imaging technique

In the second paper, the level of suppression of linear scattering is investigated using a unfocused LF beam together with a focused HF beam, and where the nonlinear propagation delay is estimated and corrected for. This beam setup is of interest since it yields an even LF pressure over the whole imaging range of the HF. For increasing LF pressure the level of suppression of linear scattering decreases. It is shown that there is an increasing amplitude difference between the two HF pulses transmitted at opposite polarities of the LF pulse. This amplitude difference can be due to nonlinear

distortion of the HF pulse or nonlinear aberration due to the fact the LF pressure varies over the HF beam.

This paper is under review with IEEE Transactions on Ultrasonics, Ferroelectrics and Frequency Control.

Paper C: Comparison of beamforming strategies for dual-frequency band imaging using a large frequency separation

In the third paper different beamforming strategies for dual-frequency band imaging is investigated. The three different strategies are; 1. Unfocused LF + Focused HF, 2. Focused LF + Focused HF, and 3. Unfocused LF + Unfocused HF. Pulses along the beam axis are recorded in the water tank and the nonlinear propagation delay and frequency shift is estimated. The nonlinear propagation delay and frequency shift is produced by the average experienced LF pressure and LF pressure gradient over the HF pulse, respectively. The experienced LF pressure and pressure gradient can be estimated from the recorded pulses and the delay and frequency shift is computed based on these estimates. It is shown that there is good correspondence between the estimated and predicted values of the delay and frequency shift until diffraction becomes significant. The diffraction is dependent on the frequency of the HF pulse and when the frequency changes, so does the diffraction. Nonlinear aberration is shown to shift the focused depth of the beam and thus also the diffraction.

This paper is under review with IEEE Transactions on Ultrasonics, Ferroelectrics and Frequency Control.

Paper D: Imaging of Nonlinear Scattering using Dual-frequency Band Ultrasound

In the last part of the thesis, nonlinear scattering is investigated in more detail. The nonlinear propagation effects are generated by the same process which generates nonlinear scattering, it is the pressure squared. The difference is that the nonlinear propagation effects are accumulative while the scattering is local. The nonlinear interaction between the HF and LF pulse generates frequency bands at the sum and difference frequencies of the LF and HF and the polarity of these signal components are dependent on the polarity of the LF. Thus by transmitting two dual-frequency band complexes in each direction, the nonlinear scattering can be detected if it is separable from the nonlinear propagation. If the bandwidth of the HF is less than the center frequency of the LF pulse, the sum and difference bands will not overlap with the fundamental band and the accumulation of nonlinear propagation effects is equal to the nonlinear scattering and the effects are not separable.

A method for estimating the nonlinear propagation is proposed an analyzed statistically. A performance measure for the proposed method is presented. In order to achieve optimal suppression the relationship between the nonlinear pulse distortion for

the first and second pulse complex must be spatially invariant over the transmit/receive beam of the HF. A simulation study is presented where the effect of f-number and size relationship between the HF and LF aperture on the performance of the estimator is investigated.

This paper is being prepared for submission, where results presented in chapter D.3 will be submitted to the Journal of the Acoustical Society of America (JASA) and the results from chapter D.4 will be submitted to IEEE Transactions on Ultrasonics, Ferroelectrics and Frequency Control.

Discussion and Conclusion

From the investigations carried out in this thesis it has become clear that when using a frequency relationship between the HF and LF of 1:8-10, the nonlinear propagation effects cannot be approximated to be only a propagation delay but also includes distortion of the pulse form, especially for imaging of nonlinear scattering from stiff particles where a high LF manipulation pressure must be applied. When the pulse forms are distorted the diffraction of the beam becomes different which will introduce more differences between the pulses which has propagated on different phases of the LF pulse.

Imaging of nonlinear scattering from stiff particles embedded in soft tissue has proven to be challenging. The nonlinear scattering is weak compared to the linear scattering, requiring accurate estimation and correction of the nonlinear propagation effects. Unless the HF beams are homogenous over the receive beam, the correction required to compensate for the nonlinear propagation for a given signal segment is dependent on the position of the scatterers within the beam. By using a method for estimating the correction filter by finding the filter which is optimal on average, one is then sensitive to the scatterer distribution which is unknown. This problem can be solved by designing beams which are sufficiently homogenous, or developing new estimators for the correction filters which are not based on statistical methods. The former has been shown to be difficult for available linear arrays, and the latter should be investigated in future work.

The transmit beamforming can have a great influence on the accumulation of nonlinear propagation effects and time should be spent on designing the dual-frequency transmit beams in order to optimize the imaging application.

Much time was spent during this PhD to develop the new dual-frequency band system. With limited time and funding, this left little time for experiments demonstrating nonlinear scattering from micro calcifications. This thesis has therefore focused on investigating how the dual-frequency nonlinear propagation and beamforming affects the suppression of linear scattering, and how nonlinear scattering can be detected. It is shown, using simulations that with available linear arrays, it will be difficult to image nonlinear scattering using the proposed methods. With this knowledge, future work should focus on setting up experiments for demonstrating nonlinear scattering in the lab and new arrays should be designed where the new knowledge of dual-frequency beamforming is incorporated.

1.5 Contributions

What follows is a list of contributions I have made during my time as a PhD candidate.

Peer reviewed papers

1. Svein-Erik Måsøy, **Thor Andreas Tangen**, Øyvind Standal, Jochen M. Deibele, Sven Peter Näsholm, Rune Hansen, Bjørn Angelsen, and Tonni F. Johansen, “Nonlinear propagation acoustics of dual-frequency wide-band excitation pulses in a focused ultrasound system”, *Journal of the Acoustical Society of America*, vol. 128, no. 5, 2010
2. Rune Hansen, Svein-Erik Måsøy, **Thor Andreas Tangen**, Bjørn Angelsen, “Nonlinear propagation delay and pulse distortion resulting from dual frequency band transmit pulse complexes”, *Journal of the Acoustical Society of America*, vol. 129, no. 1, 2011

Submitted for publication

1. **Thor Andreas Tangen**, Svein-Erik Måsøy, Øyvind Standal, Rune Hansen, Jochen Deibele, Amund Skavhaug, and Bjørn Angelsen, “Suppression of linear scattering for a dual-frequency band imaging technique”, submitted to *IEEE Transactions on Ultrasonics, Ferroelectrics and Frequency Control*.
2. **Thor Andreas Tangen**, Svein-Erik Måsøy, Rune Hansen, Amund Skavhaug, and Bjørn Angelsen, “Comparison of beamforming strategies for dual-frequency band imaging using a large frequency separation”, submitted to *IEEE Transactions on Ultrasonics, Ferroelectrics and Frequency Control*.

Patent applications

1. Bjørn Angelsen, Rune Hansen, Tonni F. Johansen, Svein-Erik Måsøy, Sven Peter Näsholm and **Thor Andreas Tangen**, “Nonlinear Elastic Wave Measurement and Imaging with Two-Frequency Elastic Wave Pulse Complexes”, *United States Patent Application 2010036244*.
2. Bjørn Angelsen, Rune Hansen and **Thor Andreas Tangen**, “Method for imaging of nonlinear interaction scattering”, *United States Patent Application 61/375,403*.

Conference proceedings

1. Øyvind Standal, **Thor Andreas Tangen**, and Bjørn Angelsen, “A Phase Based Approach for Estimation and Tracking of Locally Variable Delays”, *Proc. IEEE Ultrason. Symp.*, vol. 2, pp. 1583–1585, 2007.

Talks and Presentations

1. **Thor Andreas Tangen**, Rune Hansen, Svein-Erik Måsøy and Bjørn Angelsen, “Imaging of micro-calcifications for improved cancer diagnostics”, *Symposium of the Norwegian Society of Ultrasound Diagnostics (NFUD) 2008*
2. **Thor Andreas Tangen**, Rune Hansen, Svein-Erik Måsøy, Tonni F. Johansen and Bjørn Angelsen, “Comparison of SURF and Pulse Inversion for CEUS - a simulation study”, *The 14th European symposium on Ultrasound Contrast Imaging, 2009*
3. **Thor Andreas Tangen**, Rune Hansen, Svein-Erik Måsøy, Tonni F. Johansen and Bjørn Angelsen, “Comparison of SURF and Pulse Inversion for CEUS - a simulation study”, *Symposium of the Norwegian Society of Ultrasound Diagnostics (NFUD) 2009*
4. **Thor Andreas Tangen**, “Elastography - Imaging of Tissue Stiffness”, Invited Talk, *Symposium of the Norwegian Society of Ultrasound Diagnostics (NFUD) 2010*

Awards

1. GE Best Presentation Award at Symposium of the Norwegian Society of Ultrasound Diagnostics (NFUD) 2008.
2. Ultrasonix Student Award for contribution to Ultrasonix research community.

References

- [1] T. Nagashima, H. Hashimoto, K. Oshida, S. Nakano, N. Tanabe, T. Nikaido, K. Koda, and M. Miyazaki, “Ultrasound demonstration of mammographically detected microcalcifications in patients with ductal carcinoma in situ of the breast,” *Breast Cancer*, vol. 12, no. 3, pp. 216–220, 2005.
- [2] M. S. Soo, J. A. Baker, and E. L. Rosen, “Sonographic detection and sonographically guided biopsy of breast microcalcifications,” *AJR. American Journal of Roentgenology*, vol. 180, pp. 941–948, Apr. 2003. PMID: 12646433.
- [3] E. Carstensen, W. Law, N. McKay, and T. Muir, “Demonstration of nonlinear acoustical effects at biomedical frequencies and intensities,” *Ultrasound in Medicine & Biology*, vol. 6, no. 4, pp. 359–368, 1980.
- [4] T. Muir and E. Carstensen, “Prediction of nonlinear acoustic effects at biomedical frequencies and intensities,” *Ultrasound in Medicine & Biology*, vol. 6, no. 4, pp. 345–357, 1980.
- [5] B. Angelsen, *Ultrasound imaging. Waves, signals and signal processing Vol I*. Trondheim: Emantec, 2000.
- [6] M. Averkiou and D. Roundhill, “A new imaging technique based on the nonlinear properties of tissues,” in *Ultrasonics Symposium, 1997. Proceedings., 1997 IEEE*, vol. 2, pp. 1561–1566 vol.2, 1997.
- [7] C. Shen, S. Su, C. Cheng, and C. Yeh, “Dual-high-frequency ultrasound excitation on microbubble destruction volume,” *Ultrasonics*, vol. 50, pp. 698–703, June 2010.
- [8] D. Simpson and P. Burns, “Pulse inversion doppler: a new method for detecting nonlinear echoes from microbubble contrast agents,” in *Ultrasonics Symposium, 1997. Proceedings., 1997 IEEE*, vol. 2, pp. 1597–1600 vol.2, 1997.
- [9] R. J. Eckersley, C. T. Chin, and P. N. Burns, “Optimising phase and amplitude modulation schemes for imaging microbubble contrast agents at low acoustic power,” *Ultrasound in Medicine & Biology*, vol. 31, pp. 213–219, Feb. 2005. PMID: 15708461.

-
- [10] B. Haider and R. Chiao, "Higher order nonlinear ultrasonic imaging," in *Ultrasonics Symposium, 1999. Proceedings. 1999 IEEE*, vol. 2, pp. 1527–1531 vol.2, 1999.
- [11] C. X. Deng, F. L. Lizzi, A. Kalisz, A. Rosado, R. H. Silverman, and D. J. Coleman, "Study of ultrasonic contrast agents using a dual-frequency band technique," *Ultrasound in Medicine & Biology*, vol. 26, no. 5, pp. 819 – 831, 2000.
- [12] R. Hansen and B. Angelsen, "SURF imaging for contrast agent detection," *Ultrasonics, Ferroelectrics and Frequency Control, IEEE Transactions on*, vol. 56, no. 2, pp. 280–290, 2009.
- [13] A. Bouakaz, M. Versluis, J. Borsboom, and N. de Jong, "Radial modulation of microbubbles for ultrasound contrast imaging," *Ultrasonics, Ferroelectrics and Frequency Control, IEEE Transactions on*, vol. 54, no. 11, pp. 2283–2290, 2007.
- [14] S. Måsøy, O. Standal, P. Nasholm, T. Johansen, B. Angelsen, and R. Hansen, "SURF imaging: In vivo demonstration of an ultrasound contrast agent detection technique," *Ultrasonics, Ferroelectrics and Frequency Control, IEEE Transactions on*, vol. 55, no. 5, pp. 1112–1121, 2008.
- [15] E. Cherin, J. Brown, S. Måsøy, H. Shariff, R. Karshafian, R. Williams, P. N. Burns, and F. S. Foster, "Radial modulation imaging of microbubble contrast agents at high frequency," *Ultrasound in Medicine & Biology*, vol. 34, pp. 949–962, June 2008.
- [16] D. Zhang, X. Chen, and X. fen Gong, "Acoustic nonlinearity parameter tomography for biological tissues via parametric array from a circular piston source—Theoretical analysis and computer simulations," *The Journal of the Acoustical Society of America*, vol. 109, pp. 1219–1225, Mar. 2001.
- [17] D. Zhang and X. Gong, "Experimental investigation of the acoustic nonlinearity parameter tomography for excised pathological biological tissues," *Ultrasound in Medicine & Biology*, vol. 25, pp. 593–599, May 1999.
- [18] N. Ichida, "Imaging the nonlinear ultrasonic parameter of a medium," *Ultrasonic imaging*, vol. 5, no. 4, p. 295, 1983.
- [19] H. Fukukita, "Ultrasound pulse reflection mode measurement of nonlinearity parameter B/A and attenuation coefficient," *The Journal of the Acoustical Society of America*, vol. 99, no. 5, p. 2775, 1996.
- [20] F. A. Duck, *Physical Properties of Tissues: A Comprehensive Reference Network*. Elsevier Science & Technology Books, Feb. 1990.
- [21] M. Fatemi and J. F. Greenleaf, "Vibro-acoustography: An imaging modality based on ultrasound-stimulated acoustic emission," *Proceedings of the National Academy of Sciences of the United States of America*, vol. 96, pp. 6603–6608, June 1999.

- [22] M. Fatemi, L. E. Wold, A. Alizad, and J. F. Greenleaf, "Vibro-acoustic tissue mammography," *IEEE Transactions on Medical Imaging*, vol. 21, pp. 1–8, Jan. 2002. PMID: 11838661.
- [23] A. Alizad, D. H. Whaley, J. F. Greenleaf, and M. Fatemi, "Potential applications of vibro-acoustography in breast imaging," *Technology in Cancer Research & Treatment*, vol. 4, pp. 151–158, Apr. 2005. PMID: 15773784.
- [24] R. Hansen, S. Masoy, T. F. Johansen, and B. A. Angelsen, "Utilizing dual frequency band transmit pulse complexes in medical ultrasound imaging," *The Journal of the Acoustical Society of America*, vol. 127, pp. 579–587, Jan. 2010.
- [25] S. Nasholm, R. Hansen, S.-E. Måsøy, T. Johansen, and B. Angelsen, "Transmit beams adapted to reverberation noise suppression using dual-frequency SURF imaging," *Ultrasonics, Ferroelectrics and Frequency Control, IEEE Transactions on*, vol. 56, no. 10, pp. 2124–2133, 2009.
- [26] S. B. W. and K. P., eds., *World Cancer report*. WHO, IARC Press. Lyon, 2003.
- [27] "World health organization, fact sheet no. 297: Cancer." <http://www.who.int/mediacentre/factsheets/fs297/en/index.html>, 2006.
- [28] J. D. Iannuccilli, J. J. Cronan, and J. M. Monchik, "Risk for malignancy of thyroid nodules as assessed by sonographic criteria: the need for biopsy," *Journal of Ultrasound in Medicine: Official Journal of the American Institute of Ultrasound in Medicine*, vol. 23, pp. 1455–1464, Nov. 2004. PMID: 15498910.
- [29] S. Egawa, T. M. Wheeler, D. R. Greene, and P. T. Scardino, "Unusual hyperechoic appearance of prostate cancer on transrectal ultrasonography," *British Journal of Urology*, vol. 69, pp. 169–174, Feb. 1992. PMID: 1311217.
- [30] F. T. Abul, N. Arun, M. A. Abu-Assi, and A. M. Asbeutah, "Transrectal ultrasound guided biopsy for detecting prostate cancer: can random biopsies be reduced using the 4-dimensional technique?," *International Urology and Nephrology*, vol. 39, no. 2, pp. 517–524, 2007. PMID: 17308874.
- [31] A. Karellas and S. Vedantham, "Breast cancer imaging: A perspective for the next decade," *Medical Physics*, vol. 35, pp. 4878–4897, Nov. 2008. PMID: 19070222 PMCID: 2673595.
- [32] J. G. Elmore, K. Armstrong, C. D. Lehman, and S. W. Fletcher, "Screening for breast cancer," *JAMA*, vol. 293, pp. 1245–1256, Mar. 2005.
- [33] L. Liberman, T. L. Feng, D. D. Dershaw, E. A. Morris, and A. F. Abramson, "US-guided core breast biopsy: use and cost-effectiveness," *Radiology*, vol. 208, pp. 717–723, Sept. 1998. PMID: 9722851.
- [34] S. H. Parker and F. Burbank, "A practical approach to minimally invasive breast biopsy," *Radiology*, vol. 200, pp. 11–20, July 1996. PMID: 8657896.

-
- [35] M. S. Soo, J. A. Baker, E. L. Rosen, and T. T. Vo, "Sonographically guided biopsy of suspicious microcalcifications of the breast: a pilot study," *AJR. American Journal of Roentgenology*, vol. 178, pp. 1007–1015, Apr. 2002. PMID: 11906892.
- [36] W. Teh and A. R. Wilson, "The role of ultrasound in breast cancer screening. a consensus statement by the european group for breast cancer screening," *European Journal of Cancer (Oxford, England: 1990)*, vol. 34, pp. 449–450, Mar. 1998. PMID: 9713292.
- [37] I. Mittra, M. Baum, H. Thornton, and J. Houghton, "Is clinical breast examination an acceptable alternative to mammographic screening?," *BMJ (Clinical Research Ed.)*, vol. 321, pp. 1071–1073, Oct. 2000. PMID: 11053185.
- [38] A. T. Stavros, D. Thickman, C. L. Rapp, M. A. Dennis, S. H. Parker, and G. A. Sisney, "Solid breast nodules: use of sonography to distinguish between benign and malignant lesions," *Radiology*, vol. 196, pp. 123–134, July 1995. PMID: 7784555.
- [39] L. Irwig, N. Houssami, and C. van Vliet, "New technologies in screening for breast cancer: a systematic review of their accuracy," *British Journal of Cancer*, vol. 90, pp. 2118–2122, June 2004. PMID: 15150556 PMID: 2410286.
- [40] W. K. Moon, J. G. Im, Y. H. Koh, D. Y. Noh, and I. A. Park, "US of mammographically detected clustered microcalcifications," *Radiology*, vol. 217, pp. 849–854, Dec. 2000. PMID: 11110953.
- [41] W. T. Yang, M. Suen, A. Ahuja, and C. Metreweli, "In vivo demonstration of microcalcification in breast cancer using high resolution ultrasound," *The British Journal of Radiology*, vol. 70, pp. 685–690, July 1997. PMID: 9245879.
- [42] F. Kasumi, "Can microcalcifications located within breast carcinomas be detected by ultrasound imaging?," *Ultrasound in Medicine & Biology*, vol. 14 Suppl 1, pp. 175–182, 1988. PMID: 3055590.
- [43] M. E. Anderson, M. S. Soo, R. C. Bentley, and G. E. Trahey, "The detection of breast microcalcifications with medical ultrasound," *The Journal of the Acoustical Society of America*, vol. 101, pp. 29–39, Jan. 1997.
- [44] M. Anderson, M. Soo, R. Bentley, and G. Trahey, "Evaluation of the ultrasonic detectability of microcalcifications," in *Ultrasonics Symposium, 1995. Proceedings., 1995 IEEE*, vol. 2, pp. 1161–1166 vol.2, 1995.
- [45] A. Alizad, M. Fatemi, L. Wold, and J. Greenleaf, "Performance of vibro-acoustography in detecting microcalcifications in excised human breast tissue: a study of 74 tissue samples," *Medical Imaging, IEEE Transactions on*, vol. 23, no. 3, pp. 307–312, 2004.
- [46] A. Alizad, D. H. Whaley, J. F. Greenleaf, and M. Fatemi, "Critical issues in breast imaging by vibro-acoustography," *Ultrasonics*, vol. 44 Suppl 1, pp. e217–220, Dec. 2006. PMID: 16843513.

- [47] G. T. Silva, J. F. Greenleaf, and M. Fatemi, “Linear arrays for vibro-acoustography: a numerical simulation study,” *Ultrasonic Imaging*, vol. 26, pp. 1–17, Jan. 2004. PMID: 15134390.
- [48] Y. Zheng, A. Yao, J. Lin, R. Kinnick, J. Greenleaf, and M. Fatemi, “Reverberation reduction in vibro-acoustography using channel estimation method,” in *Ultrasonics Symposium, 2008. IUS 2008. IEEE*, pp. 2025–2028, 2008.
- [49] S. Chiou, F. Forsberg, T. B. Fox, and L. Needleman, “Comparing differential tissue harmonic imaging with tissue harmonic and fundamental gray scale imaging of the liver,” *Journal of Ultrasound in Medicine: Official Journal of the American Institute of Ultrasound in Medicine*, vol. 26, pp. 1557–1563, Nov. 2007. PMID: 17957050.

Nonlinear propagation acoustics of dual-frequency wide-band excitation pulses in a focused ultrasound system

Svein-Erik Måsøy¹, Thor Andreas Tangen², Øyvind Standal¹, Jochen Deibele¹, Sven Peter Näsholm¹, Rune Hansen^{1,3}, Bjørn Angelsen¹ and Tonni F. Johansen¹

¹Department of Circulation and Medical Imaging, NTNU, Trondheim, Norway,

²Department of Engineering Cybernetics, NTNU, Trondheim, Norway,

³SINTEF Society and Health, Trondheim Norway

Abstract

In this article, acoustic propagation effects of dual-frequency wide-band excitation pulses in a focused ultrasound system are demonstrated in vitro. A designed and manufactured dual-frequency band annular array capable of transmitting 0.9/7.5 MHz center frequency wide-band pulses was used for this purpose. The dual-frequency band annular array, has been designed using a bi-layer piezo-electric stack. Water tank measurements demonstrate the function of the array by activating the low- and high-frequency layers individually and simultaneously. The results show that the array works as intended. Activating the low- and high-frequency layers individually, results in less than -50 dB signal level from the high- and low-frequency layers respectively. Activating both layers simultaneously, produce a well defined dual-frequency pulse. The presence of the low-frequency pulse leads to compression, expansion, and a time delay of the high-frequency pulse. There is a phase shift between the low- and high-frequency pulse as it propagates from the array to the focus. This makes the latter described effects also dependent on the array configuration. By varying the low-frequency pressure, a shift of up to 0.5 MHz in center frequency of a 8.0 MHz transmitted high-frequency pulse is observed at the array focus. The results demonstrate the high propagation complexity of dual-frequency pulses.

A.1 Introduction

The goal of this article is to present measurements detailing the complex nonlinear propagation acoustics of dual-frequency wide-band excitation pulses with a large separation in frequency, in a focused ultrasound system. For this purpose, a dual-frequency band annular array has been developed with a bi-layer piezo-electric transducer designed to transmit dual-frequency band pulses simultaneously using the same acoustic surface.

The authors of this article have developed a method named *Second-order Ultra-sound Field imaging*, abbreviated SURF imaging. [1–5] The SURF imaging technique is based on transmission of dual-frequency band pulses from the same acoustic source using a low-frequency (LF) manipulation pulse and a high-frequency (HF) imaging pulse, typically having a frequency separation of greater than 1:7. The two pulses are wide band, usually with a length less than 4 periods. The purpose of the LF pulse is to manipulate the scattering and propagation of the HF imaging pulse, and is only transmitted and not received. The HF imaging pulse is then used to image tissue or nonlinear scatterers under the influence of the manipulation pulse.

The concept of using dual-frequency band pulses is not new, and in the following a literature review of methods using dual-frequency band pulses is presented. In order to utilize dual-frequency band methods in ultrasound applications, probes capable of transmitting such pulses are required. Therefore a review of multi-frequency band probes and their possible use is also given to provide perspective on the wide range of potential applications for such probes.

Research on ultrasound methods that use dual-frequency band pulses started early in the 1980s. A series of papers where dual-frequency pulse complexes were used to estimate or image the nonlinear parameter B/A in tissues and liquids have been published. [6–13]

Ultrasound contrast agents are particularly sensitive to the manipulation pulse, and changes in their scattering properties may then be probed by the imaging pulse to form a high-frequency contrast agent detection technique. These effects have been demonstrated by several groups, including the authors of this article, through theory, simulations and laboratory measurements. [1, 2, 14–19] Måsøy *et al.* also demonstrated this *in vivo* in pigs using an experimental system with a 7.5 MHz imaging frequency. [3]

SURF imaging techniques may also be used to form transmit beams for reverberation noise suppression, similar to harmonic imaging, but with a range of adjustable parameters to control the region of noise suppression. A recent paper and a PhD study from the authors of this article demonstrates this in detail through theory and simulations. [4, 20]

An ultrasound probe is usually composed of a single acoustic element or an array of such elements. Each element is typically constructed as an impedance matching layer on the tissue side, followed by a single layer piezo-electric transducer, and a backing layer to remove multiple reflections in the element. The matching and backing layers are passive, while the piezo-electric transducer is active using two electrodes on either side of the transducer. In this article, the word *transducer* refers only to the active part of an element, that is the piezo-electric component together with the electrodes.

In order to create dual- or multi-band probes with a large separation in frequency, new designs need to be generated since state-of-the-art piezo-electric components do not have the necessary band width.

There has been interest in designing dual- or multi-frequency ultrasound probes for medical applications in both the research and industrial communities. These probes are generally aimed at improving harmonic imaging methods (tissue harmonic imaging and/or ultrasound contrast detection), [21–24] creating new ultrasound contrast detection schemes, [3, 25] optimizing imaging and Doppler velocity estimation, [26] sizing of micro-emboli, [27] combining imaging with ultrasound generated/mediated therapy schemes or a combination of any of the aforementioned methods. [28–33]

Takeuchi *et al.* [22], and Vos *et al.* [24] constructed double-peak frequency elements by tuning either the matching layer, or the matching and backing layers of a standard ultrasound element configuration. The purpose of these probes was to perform either sub-harmonic or second-harmonic imaging for ultrasound contrast agent detection. Schaetzle *et al.* [28] proposed to divide the single piezo-electric transducer into two regions by using a third coupling electrode in order to perform imaging and therapy alternately with the same probe.

Forsberg *et al.* [23] placed three separate linear arrays on a curved surface for nonlinear contrast imaging. Based on this construction, two different probes were made with center frequencies of 2.5/5.0/10.0 MHz and 1.75/3.5/7.0 MHz respectively. Ferin *et al.* [33] stacked two linear arrays of approximately 3 MHz center frequency on each side of a 7.5 MHz linear array. The total -6 dB bandwidth of the final probe ranged from 2-10 MHz, and the probe was intended for multi-purpose use.

Bouakaz *et al.* [25] created a probe where two different standard elements at 0.9 MHz and 2.8 MHz center frequency were interleaved to form an array for contrast agent imaging at frequencies higher than the second-harmonic component. [34] This solution has also been proposed for combining high-resolution imaging and therapy applications. [29] Palanchon *et al.* [27] used two independent concentric annular elements for transmission of a 130 kHz and a 360 kHz pulse, and a polyvinylidene fluoride (PVDF) transducer glued on top of the matching layer of the annular elements for reception. The purpose of this probe was to detect and size microemboli.

Fukukita *et al.* [13] used a five-element annular array to generate a 2.5 MHz pulse, and a coaxial concentric external ring element for a 0.3 MHz pulse in order to transmit these pulses simultaneously for B/A estimation. The same solution was used by Måsøy *et al.* [3] to generate a dual-frequency band transmit pulse of 0.9 MHz and 7.5 MHz for ultrasound contrast detection at 7.5 MHz.

Hossack *et al.* [21] implemented a bi-layer piezo-electric transducer in a single element probe optimized for second-harmonic imaging. Each of the piezo-electric transducers had the same thickness, and by switching the effective polarity of the two layers between transmit and receive a wide-band probe was achieved. Saitoh *et al.* [26] made a similar structure, but with a thickness ratio of 1/0.7 in the two piezo-electric layers. This resulted in a probe with 3.75 and 7.5 MHz frequencies for imaging at the high frequency and Doppler estimation at the low frequency. Azuma *et al.* [30, 31] designed a probe with 0.5 and 2 MHz center frequencies for therapy and Doppler monitoring using a bi-layer piezo-electric transducer.

In this article, acoustic propagation effects of dual-frequency wide-band pulses in a focused ultrasound system are demonstrated *in vitro*. A designed and manufactured dual-frequency band annular array with design center frequencies of 0.9/7.5 MHz was used for this purpose. In order to have a common acoustic radiation surface the LF and HF piezo-electric elements are stacked on top of each other in a bi-layer structure. A more detailed description of a similar design using the same bi-layer structure in a linear prototype array with 1.25/10 MHz center frequencies, can be found in Ref. 35. The array is controlled by an 8 channel experimental ultrasound system named Pulse-Echo Lab, equipped with an arbitrary waveform generator (AWG). The LF and HF layers are excited individually and simultaneously to demonstrate the capabilities of the array, and pulses are recorded using a needle hydrophone in a water tank setup. The observed acoustic properties of the dual-frequency band pulses show that the nonlinear interaction of the LF and HF pulses must be taken into account if such pulses are to be used for imaging purposes.

A.2 Theory

In order to analyze the propagation of dual-frequency wide-band pulses and the results in this paper, a presentation of the nonlinear wave equation and the pressure in the focal point of a circular symmetric transducer is provided below.

A.2.1 Dual-frequency excitation pulses

Figure A.1 illustrates two overlapping wide-band pulses with a frequency separation of $\sim 1:9$. This represents typical dual-frequency wide-band excitation pulses used in SURF imaging techniques, and are from now on referred to as dual-frequency excitation pulses.

A.2.2 Nonlinear wave equation in a homogeneous medium

A general derivation of the nonlinear wave equation with scattering terms can be found in Refs. 36, 37. In Ref. 1, 2, 5 a condensed version of this is provided. Unless otherwise stated, the equations given in this section are taken from Ref. 5.

Disregarding scattering and absorption, the nonlinear wave equation in a homogeneous medium may be written as

$$\nabla^2 \varphi - \frac{1}{c^2(p)} \frac{\partial^2 \varphi}{\partial t^2} = 0, \quad (\text{A.1})$$

where φ represents the momentum potential, and $c(p)$ is the propagation velocity in a medium with nonlinear elasticity. Spatial and time coordinates are omitted for notational convenience. The pressure dependent propagation velocity is given as

$$c(p) = \frac{1}{\sqrt{\rho\kappa(1 - 2\beta_n\kappa p)}} = \frac{c_0}{\sqrt{1 - 2\beta_n\kappa p}} \approx c_0(1 + \beta_n\kappa p), \quad (\text{A.2})$$

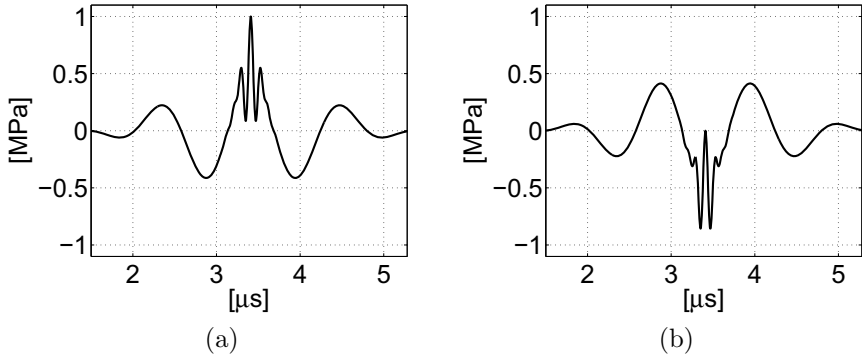


Figure A.1: Illustration of two different dual-frequency excitation pulses. Left panel: the imaging pulse is placed in a compression phase of the manipulation pulse. Right panel: the imaging pulse is placed in a rarefaction phase of the manipulation pulse. The horizontal axis displays time in μs and the vertical axis pressure in MPa. In this plot, the frequency of the manipulation pulse is 0.9 MHz and the imaging pulse 8.0 MHz.

where $c_0 = 1/\sqrt{\rho\kappa}$ and higher order terms are neglected. Here, ρ is the mass density, κ the bulk compressibility, and $\beta_n = 1 + B/2A$ the tissue nonlinearity parameter.

Using dual-frequency band pulses, it is convenient to analyze the propagation velocity $c(p)$ by separating the pressure into two components, $p = p_m + p_i$, where p_m represents the low-frequency manipulation pulse pressure and p_i the high-frequency imaging pulse pressure. Using the approximation in Eq. (A.2) and inserting the pressure gives

$$c(p_m, p_i) = c_0(1 + \beta_n \kappa p_m + \beta_n \kappa p_i) . \quad (\text{A.3})$$

The two last terms in Eq. (A.3) generate nonlinear distortion of the manipulation and imaging pulse. In addition to conventional harmonic distortion, the imaging pulse will experience a local change in the speed of sound proportional to the manipulation pulse pressure p_m . This modified sound velocity for the imaging pulse may be expressed as

$$c_i(p_m, p_i) \approx c(p_i)(1 + \beta_n \kappa p_m) , \quad (\text{A.4})$$

where $c(p_i)$ is the speed of sound for the imaging pulse with no manipulation pulse present. SURF imaging applications use short wide-band pulses, meaning that the length of the imaging pulse will only cover a sub-period length of the manipulation pulse (see Fig. A.1). If the imaging pulse travels close to a peak (or a trough) on the manipulation pulse, then it experiences a nearly constant positive (or negative) manipulation pressure over its duration, resulting in an increased (or decreased) sound velocity. If it travels on a flank of the manipulation pulse it will experience a nearly constant pressure gradient, resulting in a sound velocity varying almost linearly over the imaging pulse. The increased or decreased sound velocity causes a time delay,

and the linearly variable sound velocity a compression/expansion of the imaging pulse relative to the case when no manipulation pulse is present. This phenomenon is described and demonstrated by Fukukita *et al.*, [10, 11, 13] and may be used for B/A estimation.

A.2.3 SURF imaging using a focused ultrasound system

In a focused ultrasound system, special attention must be given to the propagating effects of dual-frequency excitation pulses. The pressure in the focal point of a circular symmetric vibrating surface in a rigid baffle may be given in the time and frequency domains as [36, Ch. 4-5]

$$\begin{aligned} p(F, t) &= \frac{\partial f(t - F/c)}{\partial t} \rho U_n \frac{A}{2\pi F} \leftrightarrow \\ \hat{p}(F, \omega) &= -i\omega \hat{f}(\omega) \rho U_n \frac{e^{-ikF}}{2\pi F} A. \end{aligned} \quad (\text{A.5})$$

Here, $f(t)$ is the time excitation of the signal, F the focus position of the surface, A the vibrating surface area, $k = \omega/c$ the wave number, and U_n the normal velocity amplitude of the vibrating surface, assuming a constant velocity distribution (no apodization).

Equation (A.5) shows that the time excitation at the focal point of a vibrating surface is the derivative of the transmit excitation (or $\pi/2$ phase shifted in the frequency domain). The differentiation may be explained in physical terms as an interference effect between the edge wave and the wave from the center of the vibrating surface. This effect strongly influences the phase relation between the manipulation and imaging pulse in a dual-frequency excitation pulse.

Assuming the manipulation and imaging arrays are coaxial and have the same focal point, Eq. (A.5) shows that in order to position the imaging pulse on a peak or a trough of the manipulation pulse at the focal point of the array, the imaging pulse must be transmitted on the gradient of the manipulation pulse (in the position of zero manipulation pressure). The imaging pulse will in both cases travel $T_m/4$, where T_m is the period of the manipulation pulse, relative to the manipulation pulse from the array surface to the focal point. That is, if the manipulation and imaging arrays have the same focal point, the propagating imaging pulse will experience both a varying gradient and manipulation pressure using dual-frequency excitation pulses. There are two sources for the varying gradient of the manipulation pulse relative to the imaging pulse, first: nonlinear harmonic distortion of the manipulation pulse as described by Eq. (A.3), second: linear diffraction of the manipulation pulse beam as described in Eq. (A.5).

This will lead to distortion of the imaging pulse in the form of compression/expansion and a time delay relative to an imaging pulse with no manipulation pulse present. This is a phenomenon which is dependent on the manipulation pressure, and the change in the manipulation pulse gradient experienced by the imaging pulse. [5]

For contrast agent detection using SURF imaging, the distortion of the imaging pulses must be compensated for in order to remove the tissue signal in a two-pulse

scheme where the contrast agent is interrogated with the imaging pulse first in a compression phase (peak), and then in an expansion phase (trough). In Ref. 3, only time delay compensation was used, which alone provided up to 6 dB increase in tissue suppression.

In order to form transmit beams adapted to multiple scattering noise reduction, [20] the distortion obtained between two imaging pulses propagating in different phases of the manipulation pulse is the key factor to generate a synthetic transmit beam suitable for reverberation suppression. A synthetic transmit beam may then be generated by simply subtracting the two imaging pulses at all recorded depths. At the array surface, the distortion is zero providing a strong suppression of the difference signal. As the two pulses propagate, the distortion accumulates, providing a stronger and stronger difference signal analogous to harmonic imaging techniques.

A.3 Method

A.3.1 Annular array

The designed dual-frequency band annular array was made to fit in a mechanically-scanned annular probe (APAT II) of a GE Vingmed Ultrasound System 5 scanner (GE Vingmed Ultrasound, Horten, Norway). This imposed limitations on the number of elements, frequency, and dimensions as detailed below. For this paper, the array was used with a custom made 8 channel bench top ultrasound system presented in Section A.3.2.

The array consists of 5 elements (the System 5 scanner handles only 5 elements for mechanical probes). Four equal area concentric HF elements with a design center frequency of 7.5 MHz, a total diameter of 10 mm, and a kerf of 0.2 mm. The fifth element is a single LF element, with a design center frequency of 0.9 MHz and diameter of 10 mm. In order to have a common acoustic radiation surface, the LF and HF elements are stacked on top of each other in a bi-layer structure as shown in Fig. A.2. The entire structure is geometrically focused at 20.6 mm.

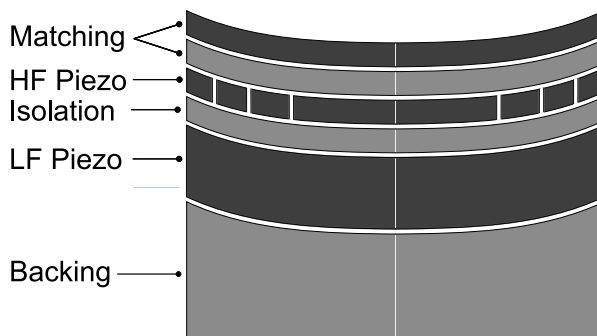


Figure A.2: Schematic drawing of the dual-band element structure.

The HF frequency was chosen to be as high as possible for use in the System 5 scanner (the scanner has a maximum receive frequency of 8 MHz). The LF frequency should be substantially lower than the HF. This in order to obtain as constant LF pressure as possible over the HF pulse when the HF is located on a peak or a trough of the LF. Here a ratio of HF/LF center frequency of approximately 8.3 was chosen as this was deemed sufficient.

In a previous design by the authors, [3] the LF element was a co-axial ring placed outside the HF rings and this allowed a total diameter of the entire array of 20 mm to fit inside the dome of the APAT II probe. Here, the LF is placed underneath the HF in a sandwich structure and due to its thickness, the total diameter of the array had to be limited to 10 mm.

The design¹ considerations of the bi-layer structure followed the same criteria as a previous design by the authors. [35] A brief description of the principles behind the design are provided here.

The array was manufactured by Imasonic (Imasonic, Besançon, France). No specific consideration about the LF and HF elements were made, and the producer manufactured these as if they were individual conventional elements. In order to remove ringing in the HF layer, an isolation layer was introduced. In a standard element, the backing usually has a low impedance compared with the piezo-electric layer in order to ensure $\lambda/2$ resonance and minimum losses into the backing. Here, the isolation layer should have a substantially lower impedance and have a $\lambda/4$ thickness in the center of the HF pass band. After manufacturing the nominal center frequencies and band widths of the LF and HF elements were {926 kHz, 54%} and {8.0 MHz, 46%} respectively.

A.3.2 Pulse-Echo Lab system

The Pulse-Echo Lab (PE-Lab) is a custom made PC-based 8 channel transmit and receive ultrasound system. For brevity, only the transmit part of the system is described here, as this was used for controlling the array in the water tank setup. A schematic of the system is given in Fig. A.3.

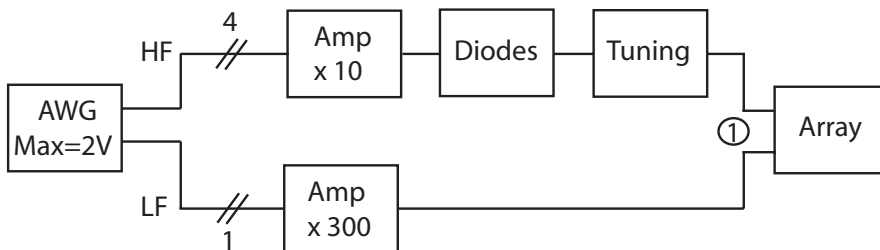


Figure A.3: Pulse-Echo Lab system.

The arbitrary waveform generator (AWG) consists of several components. Two

¹The design of the array was made by authors T. Johansen and B. Angelsen

ACQUITEK DA4300 D/A PCI boards (Acquitek, Massy, France), each with 4 channels producing a 12 bit resolution analog output voltage with a maximum of 2 V peak-to-peak. The boards are synchronized with the receive boards using an ACQUITEK CG400 clock synthesizer, and triggered with an 8 channel ACQUITEK Pulse Blaster ESR-Pro pulser. All components of the AWG and receive chain (not presented here) are connected through a PCI bus. In-house software with a graphical user interface written in MATLAB code (The Mathworks Inc., Natick, U.S.A), is used to program the AWG.

For the HF signal chain, a 4 channel TABOR ELECTRONICS 3322, 20 dB wide-band amplifier (Tabor Electronics Ltd., Tel Hanan, Israel) was used together with an in-house diode expander to reduce noise and protect the receive chain. Finally, the HF transmit signal chain was impedance tuned with serial inductors to maximize the output. The LF signal chain used the AWG for generating pulses and the signal was then amplified with a single channel 50 dB wide band ENI 2100L RF Power Amplifier (ENI, Rochester, U.S.A).

Table A.1 presents the maximum peak-to-peak voltages applied to the LF and HF elements given as a percentage value of the maximum output of the AWG (= 2 V). The maximum applied LF voltage was limited to 30 % of the AWG output to prevent delamination of the array. The linearity of the applied voltages to the elements were checked for values below the maximum and was approximately linear for both signal chains.

Table A.1: Maximum peak-to-peak voltages measured at the LF element and HF elements (measured at point 1 in Fig. A.3 using an oscilloscope). The values are given as a percentage of the maximum output of the AWG (= 2 V).

	Max AWG output	Max voltage at element(s)
LF	30%	377 V
HF	100%	33 V

A.3.3 Water tank setup

For the water tank measurements, an 85 μm ONDA HGL-0085 hydrophone with a 20 dB pre-amplifier was used (Onda Corporation, Sunnyvale, U.S.A.). The hydrophone was attached to a xyz translation stage robot (Physik Instrumente (PI) GmbH & Co. KG, Karlsruhe, Germany). Acoustic pulses were recorded with a LECROY WaveSurfer 42Xs oscilloscope (LeCroy Corporation, Chestnut Ridge, U.S.A), using a sampling frequency of 500 MHz and set to average 128 recordings in each spatial position. The whole setup is controlled by a PC with in-house software written in MATLAB.

The speed of sound of the water was estimated by measuring the temperature with a thermocouple connected to a multimeter, and using the simplified equations from Lubbers and Graaf. [39] The speed of sound found for the measurements presented here was $c \approx 1490$ m/s.

In order to find the acoustic beam axis of the array, 2D beam profiles were recorded at three suitable depths. The beam axis was found by fitting a straight line through the centers of symmetry of the 2D profiles.

A.3.4 Data processing

All data processing was performed in MATLAB. For processing HF and LF signals from measured dual-frequency excitation pulses, a second-order Butterworth IIR digital band-pass filter with zero phase distortion was used. The cut-off frequencies for the HF and LF filters were set to {5 MHz, 50 MHz} and {100 kHz, 2 MHz} respectively.

In order to estimate center frequencies, a weighted average of pulse power spectrums from the recorded pulses was calculated according to Eq. (A.6)

$$\tilde{\omega}_c = \frac{\int_{\omega_1}^{\omega_2} d\omega \omega \hat{p}(\omega)}{\int_{\omega_1}^{\omega_2} d\omega \hat{p}(\omega)}, \quad (\text{A.6})$$

where $\tilde{\omega}_c$ is the estimated center angular frequency, and $\hat{p}(\omega)$ the power spectrum. The limits of the integral, ω_1 and ω_2 , was chosen as the frequencies corresponding to the -6 dB values of the power spectrum to each side of its maximum.

Time delays between imaging pulses were determined by calculating the phase at zero lag from cross-correlation between the complex envelopes of these pulses.

A.4 Results

For all measurements presented, the AWG of the PE-Lab system was programmed with a 1.5 period 8 MHz center frequency sine pulse for the HF signal, and a 2.5 period 0.9 MHz center frequency sine pulse for the LF signal. To demonstrate the propagation aspects of dual-frequency band pulses in a focused ultrasound system, a three-pulse scheme was used where the HF pulse was transmitted with no LF pulse present, or on the positive or negative part of the LF pulse, and given the designations 0, + and $-$, respectively. The timing was chosen so that the peak of the HF envelope coincided with the zero crossing of the LF pulse on transmit. By Eq. (A.5), the HF pulse will then be located on a peak or in a trough of the LF pulse at the geometrical focus of the array.

The LF and HF data was filtered with band-pass filters as described in Section A.3.4, unless otherwise stated. All measured pressures of the LF and HF pulses are presented as a function of the applied voltage to the AWG in the PE-Lab system as described Section A.3.2.

Figure A.4 presents pulses and their corresponding frequency spectrums when the LF- and HF-parts of the array are excited separately. No filters are applied to these data. It is clear from Fig. A.4 that the HF- and LF-parts produce less than -50 dB of LF and HF signal strength at their respective center frequencies for this pulse setup.

Calibration of obtained pressure at the geometrical focus as a function of voltage applied to the array with LF- and HF-parts excited separately, is shown in Fig. A.5. For the LF element, the relationship is approximately linear for both the LF +, and $-$

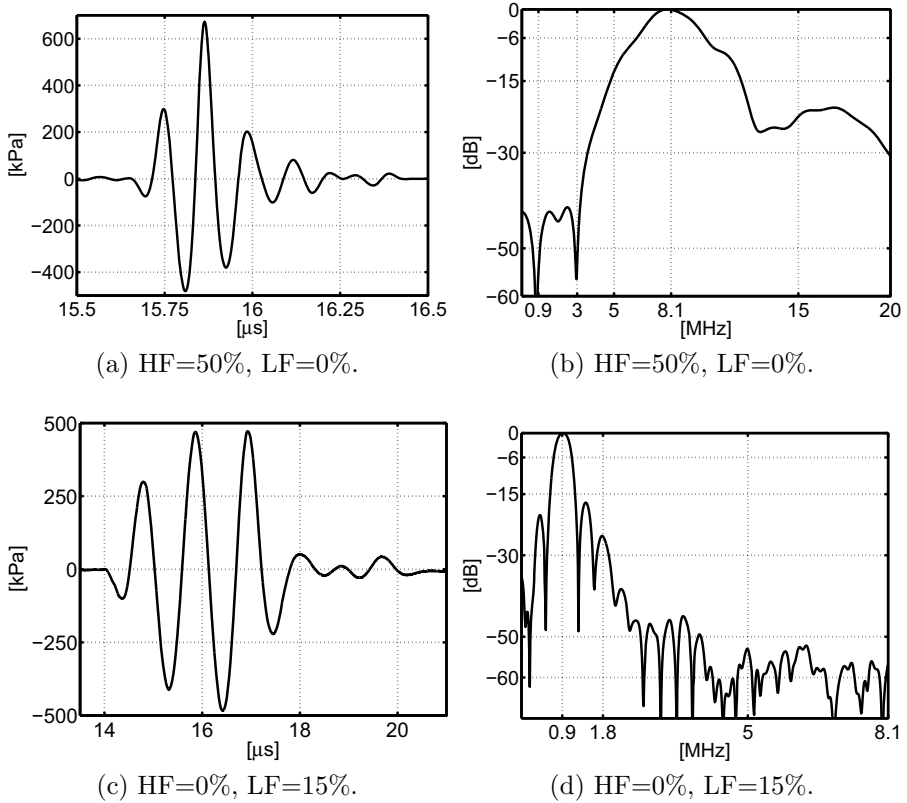


Figure A.4: HF and LF pulses in the geometrical focus of the array (20.6 mm). Here, 2 active HF elements were used. To the left, the pulses are presented in the time domain and to the right in the frequency domain. For the frequency spectrums, the estimated center frequencies are given in the plots. No filters are applied to these data.

excitation. The HF elements show some non-linearity which is due to the high degree of second-harmonic generation in water.

In Fig. A.6, dual-frequency excitation pulses for two different LF settings are presented. The upper panels represent typical dual-frequency excitation pulses for contrast agent imaging. The lower panels show typical pulses for reverberation suppression, [4, 20] where a much higher LF pressure is used.

A dual-frequency excitation pulse and its frequency spectrum is shown in Fig. A.7. The frequency spectrum shows that the LF band is clearly separated from the HF band. The second-harmonic component of the LF and HF pulses are also visible.

The effect of maintaining a given HF pressure while varying the LF pressure for a dual-frequency excitation pulse at the focal point of the array is shown in Fig. A.8. The HF center frequency, amplitude and time delay are plotted as functions of LF

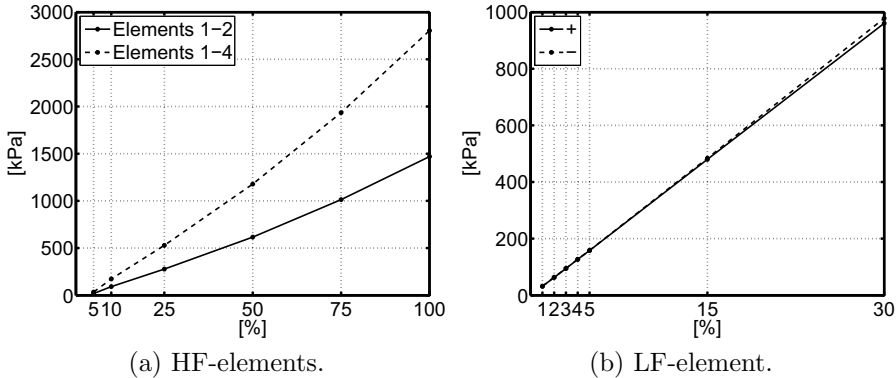


Figure A.5: Calibration curves of the high-frequency elements and the low-frequency element measured in the geometrical focus of the array. For the HF-elements, the calibration has been performed with 2 and 4 active elements. The values are given as the maximum absolute value of the filtered pulse envelopes.

pressure on transmit. All these parameters appear to depend linearly on the LF pressure. The HF center frequencies are $\{7.8, 8.3, 8.9\}$ MHz for $\text{LF}=\{-30, 0, +30\}$. The HF amplitudes are $\{518, 616, 702\}$ kPa and the time delays between the different HF pulses are $\{-4.7, 0.0, +5.7\}$ ns for the same LF transmit amplitudes. This means that there is a center frequency shift of 1.1 MHz, amplitude variation of 184 kPa and a time delay of 10.4 ns between the HF pulse on a peak and in a trough using $\text{LF}=\pm 30\%$ for this particular setup.

Figure A.9 presents examples of the filtered HF pulses and their corresponding frequency spectrums used to find the parameters in Fig. A.8. The compression and expansion effects are clearly visible for these cases.

Axial scans of the dual-frequency excitation beams for different LF settings are presented in Fig. A.10. For safety reasons, the hydrophone recordings started 6 mm from the array surface. The axial LF pressure experienced by the HF is found by determining the LF pressure at the center position of the HF envelope. This is calculated using Eq. (A.6) with the complex envelope instead of the power spectrum, and -6 dB as the lower and upper integration limits. Note that this curve indirectly demonstrates Eq. (A.5) showing that close to the array, the LF pressure experienced by the HF pulse is approximately zero (deviations are due to near-field diffraction). This means that the HF pulse is indeed located on the zero crossing of the LF pulse. Approaching the focal point, the LF pressure experienced by the HF pulse increases rapidly resembling the axial profile of the LF pulse. At the focus, the experienced pressure is very close to the actual LF pressure showing that the HF pulse has moved from the zero crossing to the peak/trough of the LF pulse. The deviations may be due to the use of Eq. (A.6) for determining the location of the HF pulse.

The HF frequency varies rapidly in the near-field due to near-field edge wave effects, making the estimation of the center frequency challenging. From approximately

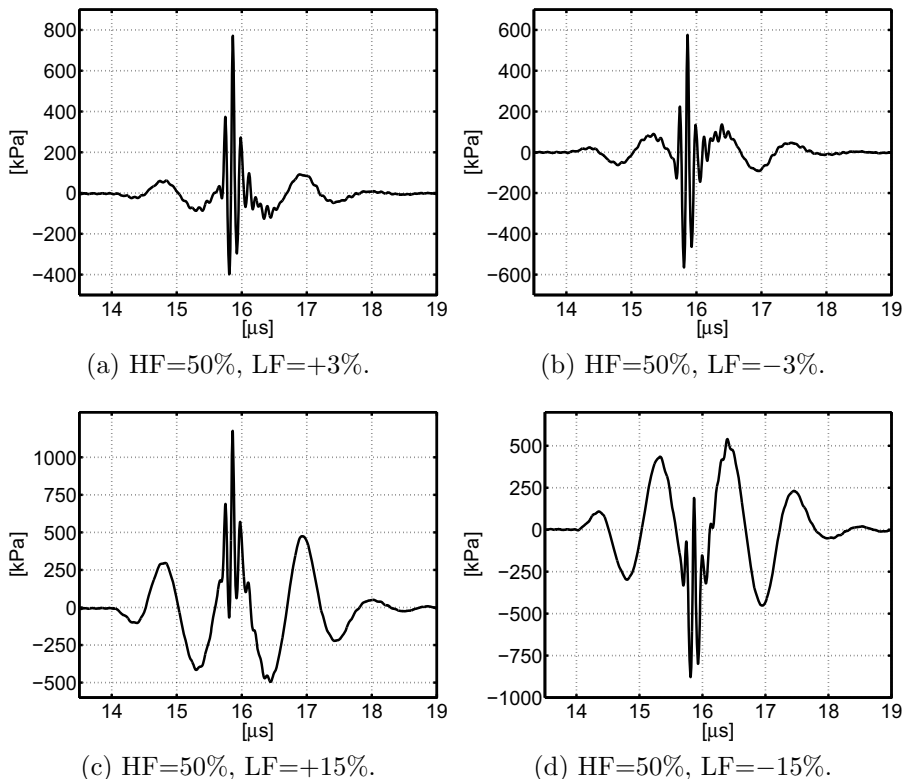


Figure A.6: Dual-frequency excitation pulses in the geometrical focus of the array with 2 active HF elements and different LF pressures. No filters are applied to these data.

15 mm, a marked center frequency shift is observed as a function of depth. The HF pressure amplitude also varies accordingly as a function of depth. The total time delay between the LF+ and LF- excitation reaches approximately 31 ns at 40 mm depth.

A.5 Discussion

The results in this article demonstrate that the designed and manufactured dual-frequency band annular array is capable of transmitting dual-frequency excitation pulses. Exciting the LF and HF elements separately produce very little excitation of the HF and LF elements, respectively, as demonstrated in Fig. A.4. Exciting them simultaneously produces well defined dual-frequency wide-band pulses.

Applying a 33 V peak-to-peak voltage to the HF elements results in a maximum focal pressure of {1.5, 2.8} MPa [which is also approximately the maximum axial pressure, see Fig. A.10 (c)], when exciting 2 and 4 elements, respectively, as demonstrated in Fig.A.5. Using 377 V on the LF element results in approximately 1.0 MPa in the

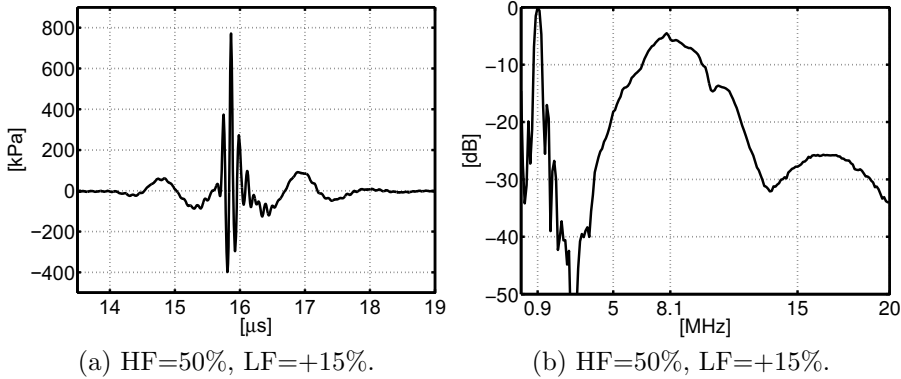


Figure A.7: Dual-frequency excitation pulse in the geometrical focus of the array with 2 active HF elements, and corresponding frequency spectrum. No filters are applied to these data.

focal point, but 1.5 MPa maximum axial pressure [see Fig. A.10 (a)].

Potential cross-talk between the LF and HF elements was evaluated (at point 1 in Fig. A.3) using the oscilloscope for the different transmit voltages used. Transmitting using only the LF element alone, or both the LF and HF elements did not result in any change in the measured voltages on the elements. This indicates that the amplitude differences in the imaging pulses for different manipulation pressures are due solely to propagation.

The large separation of the locations of maximum axial pressure for the LF- and HF-elements is due to the large difference in the Fresnel parameter. The Fresnel parameter describes the diffraction and focusing characteristics of an array, and the parameter may be defined for an annular array as [36, pp. 5.69]

$$S = \frac{4f_{\#}}{D/\lambda}, \quad (\text{A.7})$$

where, $f_{\#} = F/D$, is the f-number, and D is the diameter of the array. Using all four HF elements, the LF and HF apertures, and thus also their f-numbers are equal and become $f_{\#} = 2.1$. Using only two HF elements, the f-number is $f_{\#} = 2.9$. The Fresnel parameter for the LF and HF elements using 2 or 4 active elements are then $S = \{1.36, 0.31, 0.15\}$ respectively. Now, a low Fresnel parameter provides efficient focusing of the array. Typical values for efficient focusing of annular arrays are in the order of 0.1 to 0.3. [36, pp. 5.72] Therefore, the LF is not efficiently focused and the maximum axial pressure occurs at 10 mm, only half the way to the focus point of the element.

From Fig. A.10 (a) it is clear that the imaging pulse experiences a negative manipulation pressure from approximately 6-8 mm. This is due to near-field edge wave interference, making the imaging pulse slide back and forth relative to the zero crossing of the manipulation pulse.

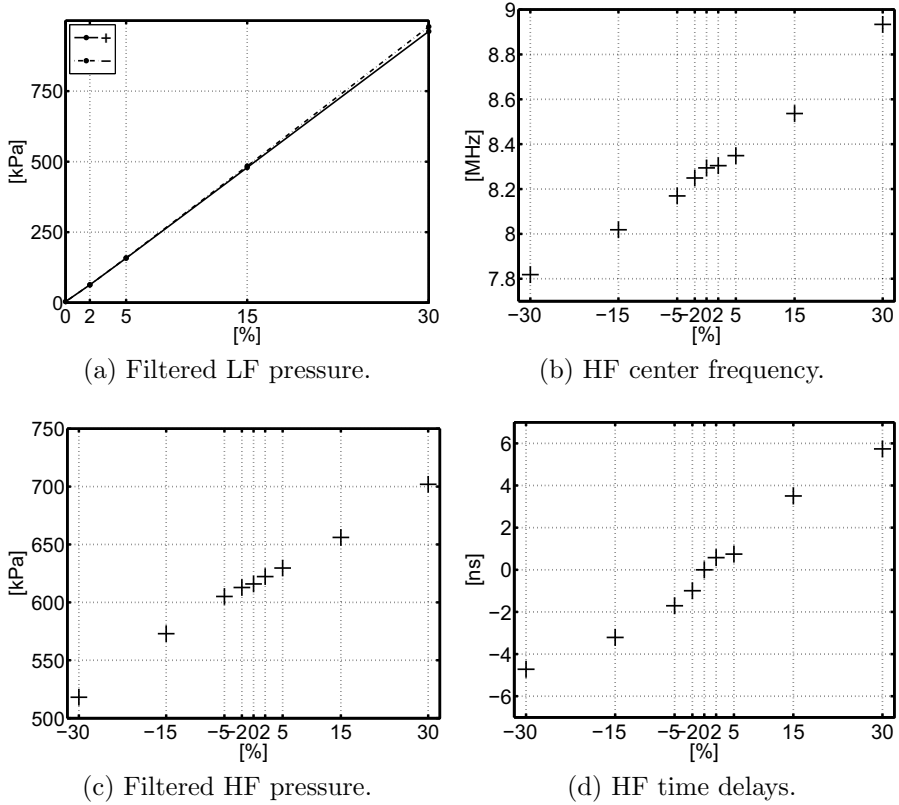


Figure A.8: HF (50%, two active HF elements) center frequency, pressure, and time delay as a function of LF pressure in the geometrical focus of the array. The pressure values are given as the maximum absolute value of the filtered pulse envelopes.

The results also demonstrate the complexity of using SURF imaging with a focused ultrasound system, where compression and expansion effects of the imaging pulses are observed. For the maximum manipulation pressure used here, the compression/expansion is substantial, leading to a 0.5 MHz change in center frequency for an imaging pulse transmitted on a positive gradient compared to when no manipulation pulse is present. It is clear from Eqs. (A.4) and (A.5) that this effect is dependent on nonlinear distortion of the manipulation pulse and the diffraction difference between the manipulation and imaging transmit beams. Both these effects influence the manipulation pressure experienced by the imaging pulse, as demonstrated in Fig. A.10.

In the general situation, a whole range of parameters influence the amount of compression/expansion of the imaging pulse in a focused system. These are:

1. Aperture sizes of both the manipulation and imaging pulse.

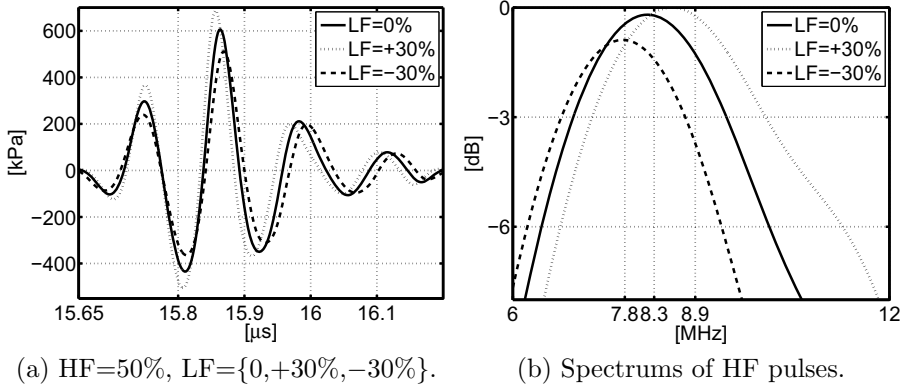


Figure A.9: Filtered HF pulses and corresponding frequency spectrums as a function of LF pressure in the geometrical focus of the array. The estimated center frequency is also given in the spectrum plots.

2. Focal depth of both apertures.
3. Frequencies of both the manipulation and imaging pulse.
4. Manipulation pulse amplitude.
5. Absorption in the medium.
6. Temporal position of imaging pulse relative to manipulation pulse on transmit.

The change in the manipulation pulse gradient due to nonlinear distortion of this pulse is mainly dependent on the first five points. Aperture size, focal depth, frequency, amplitude, and absorption all contribute to the amount of nonlinear distortion generated by the manipulation pulse. Also, for a given array configuration, the difference in diffraction patterns between the manipulation and imaging transmit beams is determined by the first five points. In this case, the compression/expansion effect can still be manipulated by altering the timing between the two pulses on transmit. As described in the introduction, having a frequency separation of greater than 1:7 and wide-band pulses with a pulse length less than 4 periods, pulse length should have minimum influence on the effects described above.

As described in Section A.2.3, the imaging pulse will travel a quarter period relative to the manipulation pulse from the array surface to the focal point. Placing the imaging pulse in different temporal positions on the manipulation pulse on transmit, will alter the compression and expansion of the imaging pulse due to variations in pulse pressure along the axis (due to diffraction) and harmonic distortion of the manipulation pulse. This effect may also be altered by changing the focusing efficiency of the manipulation pulse by using *e.g.* a larger aperture. This will reduce the Fresnel parameter, moving the maximum axial pressure closer to the geometrical focus of the

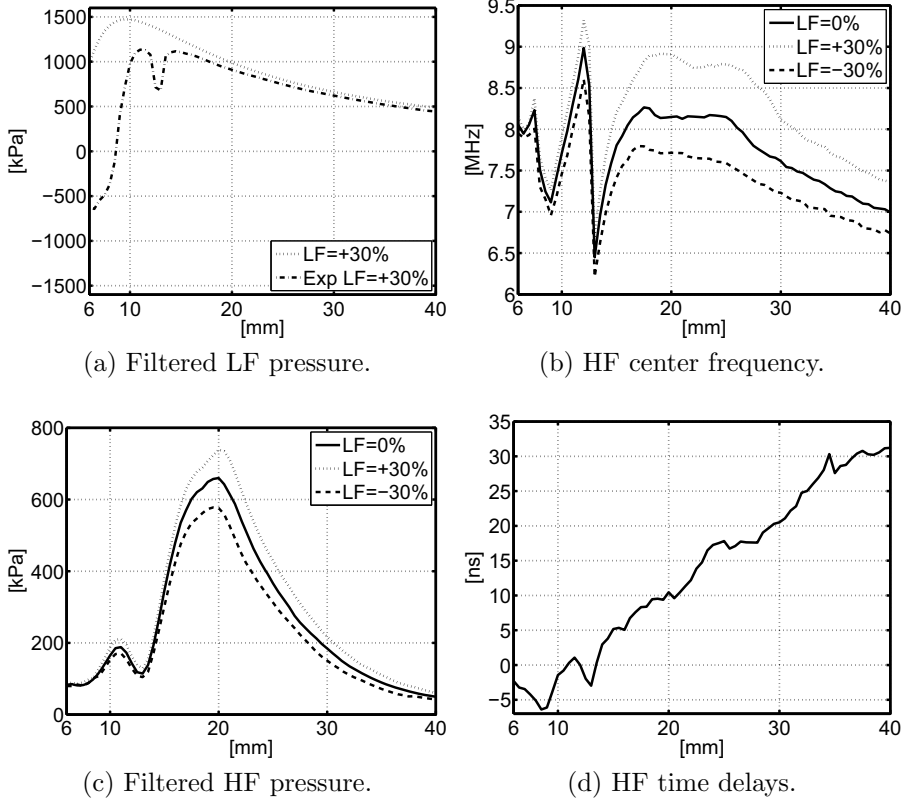


Figure A.10: LF pressure, and LF pressure experienced by the HF (denoted *Exp LF*), HF center frequencies, HF pressures, and HF time delays as a function of depth for the HF=50%, LF={+30%, -30%} case. The upper left panel presents the axial LF pressure profile given as the maximum absolute value of the filtered pulse envelopes (only LF=+30% shown here). The experienced LF pressure by the HF pulse is given as the LF pressure at the center position of the HF envelope. The time delays are here given as the time delay between the LF+ and LF- excitation.

array. In this case the manipulation pulse aperture may be chosen larger than the imaging pulse aperture.

For an efficiently focused manipulation pulse array, maintaining a constant mechanical index (MI) leads to a reduced transmit pressure due to the improved focusing capabilities. In this situation, the manipulation pulse pressure will be low close to the array with a rapid pressure increase close to the focal point. If transmitted on a gradient, the imaging pulse will then maintain its position on the gradient at a low manipulation pressure and rapidly slide over the gradient approaching the focal point. This should lead to less compression/expansion effects compared to a manipulation

pulse array with a high Fresnel number.

A.6 Conclusion

In this article, the measured acoustics of transmitted dual-frequency excitation pulses in a focused ultrasound system are presented and explained by theoretical considerations. A designed and manufactured 0.9/7.5 MHz dual-frequency band annular array capable of transmitting dual-frequency co-axial wide-band pulses using the same acoustic surface was used for this purpose.

Hydrophone measurements demonstrate the function of the array and the acoustic propagation effects of superimposed wide-band dual-frequency excitation pulses. The results show that there are substantial compression, expansion and time-delay effects of the high-frequency imaging pulse when it is propagating in different phases of the low-frequency manipulation pulse, relative to the case when no manipulation pulse is present. The compression and expansion of the imaging pulse leads to changes in axial pressure amplitudes and center frequency.

It is very important to characterize and understand these effects in order to fully utilize the potential of dual-frequency excitation techniques like SURF imaging. In a previous paper by this group, it has been shown that by compensating for the generated time-delay between the imaging pulses in a two-pulse SURF imaging contrast agent detection scheme, tissue suppression was increased by up to 6 dB *in vivo* using only 100 kPa of manipulation pulse pressure. [3] In such a situation, the time delay between the two imaging pulses is $\sim 1\text{-}2$ ns. Including compensation of the compression and expansion effect in the same situation will probably further increase the tissue suppression.

The bi-layer piezo-electric structure used in the annular array presented here, has also been manufactured and tested in a prototype of a linear array. [35] This technology allows the techniques of dual-frequency band pulse imaging to be implemented on modern medical ultrasound imaging scanners using phased, linear and curvilinear arrays.

A.7 Acknowledgements

This work was sponsored by The Research Council of Norway, the Norwegian University of Science and Technology, and the Central Norway Regional Health Authority.

References

- [1] B. A. J. Angelsen and R. Hansen, “SURF Imaging - A new Method for Ultrasound Contrast Agent Imaging”, *IEEE Ultrasonics Symposium Proceedings* 531–541 (2007).
- [2] R. Hansen and B. J. Angelsen, “SURF imaging for contrast agent detection”, *IEEE Transactions on Ultrasonics, Ferroelectrics, and Frequency Control* **56**, 280–90 (2009).
- [3] S.-E. Måsøy, Ø. Standal, P. Näsholm, T. F. Johansen, B. A. J. Angelsen, and R. Hansen, “SURF Imaging: In vivo demonstration of an ultrasound contrast agent detection technique”, *IEEE Transactions on Ultrasonics, Ferroelectrics, and Frequency Control* **55**, 1112–1121 (2008).
- [4] S. P. Näsholm, R. Hansen, S. Måsøy, T. F. Johansen, and B. A. J. Angelsen, “Transmit beams adapted to reverberation noise suppression using dual-frequency SURF imaging”, *IEEE Transactions on Ultrasonics, Ferroelectrics, and Frequency Control* **56**, 2124–2133 (2009).
- [5] R. Hansen, S. Måsøy, T. F. Johansen, and B. A. Angelsen, “Utilizing dual frequency band transmit pulse complexes in medical ultrasound imaging”, *The Journal of the Acoustical Society of America* **127**, 579–587 (2010).
- [6] N. Ichida, T. Sato, and M. Linzer, “Imaging the nonlinear ultrasonic parameter of a medium”, *Ultrasonic Imaging* **5**, 295–299 (1983).
- [7] T. Sato, A. Fukusima, N. Ichida, H. Ishikawa, H. Miwa, Y. Igarashi, T. Shimura, and K. Murakami, “Nonlinear parameter tomography system using counterpropagating probe and pump waves”, *Ultrasonic Imaging* **7**, 49–59 (1985).
- [8] T. Sato, Y. Yamakoshi, and T. Nakamura, “Nonlinear tissue imaging”, *IEEE Ultrasonics Symposium Proceedings* 889–900 (1986).
- [9] C. A. Cain, “Ultrasonic reflection mode imaging of the nonlinear parameter B/A: I. A theoretical basis”, *Journal of the Acoustical Society of America* **80**, 28–32 (1986).

-
- [10] H. Fukukita, S.-I. Ueno, and T. Yano, “Application of Nonlinear Effect to Ultrasonic Pulse Reflection Method - Modulation Characteristics of Received Pulse”, *Japanese Journal of Applied Physics* **26**, 49–51 (1987).
- [11] H. Fukukita, S.-I. Ueno, and T. Yano, “Application of Nonlinear Effect to Ultrasonic Pulse Reflection Method - Influence of a Probe Pulse with Finite Amplitude Duration”, *Japanese Journal of Applied Physics* **27**, 70–72 (1988).
- [12] K. Daehoon, J. F. Greenleaf, and C. M. Sehgal, “Ultrasonic imaging of the nonlinear parameter B/A: Simulation studies to evaluate phase and frequency modulation methods”, *Ultrasound in Medicine & Biology* **16**, 175–181 (1990).
- [13] H. Fukukita, S.-I. Ueno, and T. Yano, “Ultrasound pulse reflection mode measurement of nonlinearity parameter B/A and attenuation coefficient”, *Journal of the Acoustical Society of America* **99**, 2775–2782 (1996).
- [14] C. X. Deng, F. L. Lizzi, A. Kalisz, A. Rosado, R. H. Silverman, and D. J. Coleman, “Study of ultrasonic contrast agents using a dual-frequency band technique”, *Ultrasound in Medicine & Biology* **26**, 819–831 (2000).
- [15] R. Hansen, “New Techniques for Detection of Ultrasound Contrast Agents”, Phd, Department of Engineering Cybernetics, Norwegian University of Science and Technology, Trondheim, Norway (2004), ISBN 82-471-6209-1.
- [16] A. Bouakaz and N. de Jong, “New contrast imaging method using double frequency exposure”, *IEEE Ultrasonics Symposium Proceedings* 339–342 (2004).
- [17] H. H. Shariff, P. Bevan, R. Karshafian, R. Williams, and P. N. Burns, “Radial Modulation Imaging: Raising the Frequency for Contrast Imaging”, *IEEE Ultrasonics Symposium Proceedings* 104–107 (2006).
- [18] A. Bouakaz, M. Versluis, J. Borsboom, and N. de Jong, “Radial modulation of microbubbles for ultrasound contrast imaging”, *IEEE Transactions on Ultrasonics, Ferroelectrics, and Frequency Control* **54**, 2283–2290 (2007).
- [19] E. Chérin, J. Brown, S.-E. Måsøy, H. Shariff, R. Karshafian, R. Williams, P. N. Burns, and F. S. Foster, “Radial modulation imaging of microbubble contrast agents at high frequency”, *Ultrasound in Medicine & Biology* **34**, 949–962 (2008).
- [20] S. P. Näsholm, “Ultrasound beams for enhanced image quality”, Phd, Department of Circulation and Medical Imaging, Norwegian University of Science and Technology, Trondheim, Norway (2008), ISBN 978-82-471-9130-9.
- [21] J. Hossack, P. Mauchamp, and L. Ratsimandresy, “A high bandwidth transducer optimized for harmonic imaging”, *IEEE Ultrasonics Symposium Proceedings* **2**, 1021–1024 (2000).
- [22] S. Takeuchi, M. Rashed, A. A. Zaabi, T. Sato, and N. Kawashima, “Ultrasound Transducer with Double-Peak Frequency Characteristics for Subharmonic Imaging”, *Japanese Journal of Applied Physics* **42**, 3253–3254 (2003).

- [23] F. Forsberg, W. T. Shi, B. Jadidian, and A. A. Winder, “Multi-frequency harmonic arrays: initial experience with a novel transducer concept for nonlinear contrast imaging”, *Ultrasonics* **43**, 79–85 (2004).
- [24] H. J. Vos, M. E. Frijlink, E. Droog, D. E. Goertz, G. Blacquière, A. Gisolf, N. de Jong, and A. F. W. van der Steen, “Tranducer for Harmonic Intravascular Ultrasound Imaging”, *IEEE Transactions on Ultrasonics, Ferroelectrics, and Frequency Control* **52**, 2418–2422 (2005).
- [25] A. Bouakaz, F. ten Cate, and N. de Jong, “A new ultrasonic transducer for improved contrast nonlinear imaging”, *Physics in medicine and biology* **49**, 3515–3525 (2004).
- [26] S. Saitoh, M. Izumi, and Y. Mine, “A dual frequency ultrasonic probe for medical applications”, *IEEE Transactions on Ultrasonics, Ferroelectrics, and Frequency Control* **42**, 294–300 (1995).
- [27] P. Palanchon, A. Bouakaz, J. Klein, and N. de Jong, “Multifrequency Transducer for Microemboli Classification and Sizing”, *IEEE Transactions on Ultrasonics, Ferroelectrics, and Frequency Control* **52**, 2087–2092 (2005).
- [28] U. Schaetzle, T. Sheljaskov, and A. Lerch, “Ultrasound transducer for diagnostic and therapeutic use”, US Patent 5,823,962 (1998).
- [29] P. Mauchamp and A. Fleisch, “Multi-purpose ultrasonic slotted array transducer”, US Patent 6,537,224 B2 (2003).
- [30] T. Azuma, S.-I. Umemura, and H. Furuhashi, “Dual frequency array transducer for ultrasonic-enhanced transcranial thrombolysis”, *IEEE Ultrasonics Symposium Proceedings* 680–683 (2003).
- [31] T. Azuma, S.-I. Umemura, and H. Furuhashi, “Prototype dual frequency bilaminar array transducer capable of therapeutic exposure at 500 kHz and Doppler monitoring at 2 MHz”, *IEEE Ultrasonics Symposium Proceedings* 141–144 (2004).
- [32] W. Gueck and X.-M. Lu, “Transducer for multi-purpose ultrasound”, US Patent 2006/025326 A1 (2006).
- [33] G. Ferin, M. Legros, N. Felix, C. Notard, and L. Ratsimandresy, “Ultra-wide bandwidth array for new imaging modalities”, *IEEE Ultrasonics Symposium Proceedings* 204–207 (2007).
- [34] A. Bouakaz, S. Frigstad, F. J. ten Cate, and N. de Jong, “Super Harmonic Imaging: A new imaging technique for improved contrast detection”, *Ultrasound in Medicine & Biology* **28**, 59–68 (2002).
- [35] T. Johansen, J. Deibele, S.-E. Måsøy, R. Hansen, and B. Angelsen, “Design and Test of a Dual-Layer, Dual Frequency SURF Array”, *Proceedings of the 31st Scandinavian Symposium on Physical Acoustics*, ISBN 978-82-8123-007-1, (2008).

- [36] B. Angelsen, *Ultrasound imaging. Waves, signals and signal processing*, volume I (Emantec, Trondheim) (2000).
- [37] B. Angelsen, *Ultrasound imaging. Waves, signals and signal processing*, volume II (Emantec, Trondheim) (2000).
- [38] The design of the array was made by authors T. Johansen and B. Angelsen.
- [39] J. Lubbers and R. Graaff, “A simple and accurate formula for the sound velocity in water”, *Ultrasound in Medicine & Biology* **24**, 1065–1068 (1998).

Suppression of linear scattering for a dual-frequency band imaging technique

Thor Andreas Tangen², Svein-Erik Måsøy¹, Øyvind Standal¹, Rune Hansen^{1,3}, Jochen Deibele¹, Amund Skavhaug² and Bjørn Angelsen¹

¹Department of Circulation and Medical Imaging, NTNU, Trondheim, Norway,

²Department of Engineering Cybernetics, NTNU, Trondheim, Norway,

³SINTEF Society and Health, Trondheim Norway

Abstract

Second order Ultrasound Field (SURF) imaging uses dual-frequency band pulse complexes with overlapping high-frequency (HF) and low-frequency (LF) pulses. The technique can be used to image nonlinear scattering from e.g. ultrasound contrast agents and micro-calcifications embedded in soft tissue. The LF pulse manipulates both the local scattering and the forward propagation of the HF pulse. The forward propagation effects produce a nonlinear propagation delay and pulse form distortion of the HF pulse compared to a conventional single band pulse. In this paper an unfocused LF wave is transmitted together with a focused HF wave and the forward propagation effects are estimated. The nonlinear propagation delay is corrected for to demonstrate the ability of the SURF technique to suppress linear scattering from tissue. The linear scattering from tissue is suppressed with -35 to -17 dB dependent on the low-frequency manipulation pressure. Though the nonlinear propagation delay can be well estimated and corrected for other nonlinear propagation effects considerably limits the level of tissue suppression achieved.

B.1 Introduction

Suppression of scattering from tissue is essential in several ultrasound imaging techniques, e.g. Doppler [1] and ultrasound contrast imaging [2–4]. The ultrasound contrast agents have a highly nonlinear behavior when insonified at around the resonance frequency of the bubble [5] and this property is used to differentiate the scattering of the contrast agents from the linear scattering of tissue. For doppler imaging the scatterer velocity is used to differentiate the scattering of tissue from that of blood.

Ultrasound contrast agents are gas filled micro-bubbles with resonance frequencies in the range 2 to 4 MHz [5]. When insonified at such frequencies the bubbles are driven into harmonic oscillation, generating a backscattered signal which contains harmonics of the insonifying frequency. The level of harmonics in the scattered signal from the micro-bubbles can be higher than that scattered from tissue. This has led to the development of several nonlinear contrast agent detection techniques. The main purpose of such techniques is to suppress the linear scattered signal from tissue while maintaining as much as possible of the nonlinear scattered signal from the contrast agent. Most of the techniques used in routine clinic today are based on Pulse Inversion (PI) schemes [2], Amplitude Modulation (AM) schemes [3], or a combination of these [4].

In an effort to raise the imaging frequency for contrast agents, dual-frequency band techniques has been proposed by several groups [6–9]. In general, these methods use a low-frequency (LF) manipulation pulse to manipulate the scattering of a high-frequency (HF) imaging pulse.

When pulse inversion imaging methods were applied to normal B-mode imaging they improved the overall imaging quality [10, 11]. The contrast and resolution in the image was improved at the expense of penetration. The pulse reverberations were somewhat suppressed providing clearer images with improved contrast resolution. The reason behind this is that after the first scattering of the pulse, the pressure drops so that there is negligible accumulation of harmonics. Since some of the reverberation noise has its first scattering close to the probe, the noise originating from this area can be suppressed. This imaging method is known as Tissue Harmonic Imaging (THI) and is available on most commercial scanners.

Dual frequency methods can also be used to suppress reverberations [12]. The LF pulse manipulates the forward propagation of the HF pulse. By transmitting two pulses in each scanline direction where the LF pulse is inverted for the second pulse, the accumulation of nonlinear propagation effects can be used in the same way as for THI to suppress reverberation noise.

In addition to image nonlinear scattering from contrast bubbles and to suppress reverberation noise, dual-frequency techniques can be used for tissue characterization [13–15].

A method coined SURF imaging is such a dual-frequency band technique [8, 12, 16]. The frequency relation between the LF and HF is in the range 1:8-10. A simulated SURF pulse complex is shown in Figure B.1. The LF pulse not only manipulates the local scattering but also the propagation of the HF pulse. To be able to detect the nonlinear scattering effectively and to suppress reverberation noise, these nonlinear

propagation effects must be estimated and corrected for.

In this paper, the nonlinear propagation effects are investigated *in vitro* using a dual-frequency linear array. Using an unfocused LF manipulation pulse together with a focused HF pulse, the nonlinear propagation delay is estimated and corrected for and the tissue suppression capabilities determined for increasing LF manipulation pressures. The lower manipulation pressures are applicable for contrast imaging, while the higher pressures are more suited for suppressing reverberations.

The achievable tissue suppression is quantified and the limiting factors for suppression of linear scattering is investigated. Investigating suppression in a practical setting.

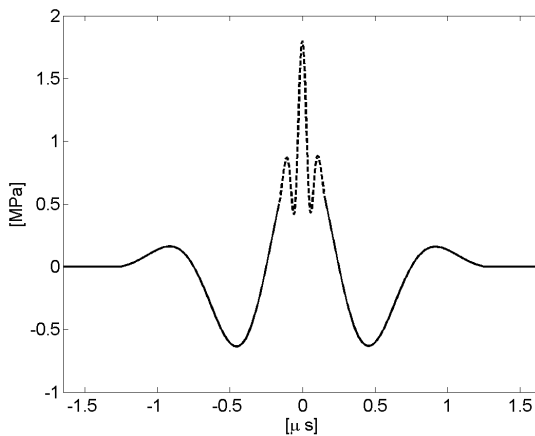


Figure B.1: SURF pulse complex consisting of a high-frequency imaging pulse(dashed) and a low-frequency manipulation pulse(solid)

B.2 Theory

B.2.1 Nonlinear wave equation

A brief derivation of the nonlinear wave equation for heterogenous tissue is given here and a full derivation can be found in [17, 18].

In the nonlinear regime the relative volume compression of a small material element ΔV is in the 2nd order approximation defined as

$$\frac{\partial V}{\Delta V} = -\nabla\psi(\underline{r}, t) \approx \kappa p - \beta_n \kappa^2 p^2, \quad (\text{B.1})$$

where ψ is the particle displacement, κ is the tissue compressibility, β_n is the tissue nonlinearity parameter and p is the pressure. Applying Newtons 2nd law on the

element with mass $\Delta m = \rho_0 \Delta V$, the net force on the element will give an acceleration of

$$\frac{\partial u(\underline{r}, t)}{\partial t} = -\frac{1}{\rho_0} \nabla p(\underline{r}, t), \quad (\text{B.2})$$

where u is the particle velocity and ρ_0 is the mass density at equilibrium.

Introducing the momentum potential

$$\begin{aligned} \nabla \varphi(\underline{r}, t) &= -\rho u(\underline{r}, t) \\ p(\underline{r}, t) &= \frac{\partial \varphi(\underline{r}, t)}{\partial t} \end{aligned} \quad (\text{B.3})$$

and combining this with (C.1) and (C.2) gives the nonlinear wave equation for homogenous tissue

$$\nabla \varphi(\underline{r}, t) - \frac{1}{c^2(\underline{r}, t)} \frac{\partial^2 \varphi(\underline{r}, t)}{\partial t^2} = 0, \quad (\text{B.4})$$

where $c(\underline{r}, t)$ is the nonlinear wave propagation velocity

$$\begin{aligned} c(\underline{r}, t) &= c_0 \sqrt{1 - 2\beta_n \nabla \frac{\partial \psi(\underline{r}, t)}{\partial t}} \\ &\approx c_0 (1 - \beta_n \kappa p(\underline{r}, t)), \end{aligned} \quad (\text{B.5})$$

and $c_0 = \frac{1}{\sqrt{\kappa \rho}}$ is the linear wave velocity.

For the heterogenous tissue, the material parameters are spatially variant. This variability can be modeled as the sum slowly varying component, a , and a rapidly varying component, f ,

$$\begin{aligned} \rho(\underline{r}) &= \rho_a(\underline{r}) + \rho_f(\underline{r}) \\ \kappa(\underline{r}) &= \kappa_a(\underline{r}) + \kappa_f(\underline{r}) \\ \beta_n(\underline{r}) &= \beta_{na}(\underline{r}) + \beta_{nf}(\underline{r}), \end{aligned} \quad (\text{B.6})$$

where the slow variations are at the scale of a wavelength. Inserting this into Equation (C.3) gives the nonlinear wave equation for heterogenous tissue

$$\begin{aligned} &\underbrace{\nabla^2 \varphi(\underline{r}, t) - \frac{1}{c^2(\underline{r}, t)} \frac{\partial^2 \varphi(\underline{r}, t)}{\partial t^2}}_{\text{Nonlinear propagation}} \\ &\quad - \underbrace{h_p \otimes_t \frac{1}{c_0^2(\underline{r})} \frac{\partial^2 \varphi(\underline{r}, t)}{\partial t^2}}_{\text{Absorption}} \\ &= \underbrace{\frac{\sigma_l(\underline{r})}{c_0^2(\underline{r})} \frac{\partial^2 \varphi(\underline{r}, t)}{\partial t^2} + \nabla(\gamma(\underline{r}) \nabla \varphi(\underline{r}; t))}_{\text{Linear scattering terms}} \\ &\quad - \underbrace{\frac{\sigma_n(\underline{r}; p)}{c_0^2(\underline{r})} \frac{\partial^2 \varphi(\underline{r}, t)}{\partial t^2}}_{\text{Nonlinear scattering terms}} \end{aligned} \quad (\text{B.7})$$

where

$$\gamma(\underline{r}) = \frac{\rho_f(\underline{r})}{\rho(\underline{r})} \quad \sigma_l(\underline{r}) = \frac{\kappa_f(\underline{r})}{\kappa_a(\underline{r})} \quad (\text{B.8})$$

are the linear scattering coefficients and

$$\sigma_n(\underline{r}, p) \approx 6\beta_{na}(\underline{r}) \kappa_a(\underline{r}) p(\underline{r}) \sigma_l(\underline{r}) \quad (\text{B.9})$$

is the nonlinear scattering coefficient. The convolution term represents frequency dependent absorption.

The left hand side of (B.7) represents the propagation of the wave, while right hand side terms represent scattering sources. The pressure dependency of the wave velocity $c(\underline{r}, t)$ implies that the high pressure part of the wave propagates with a higher velocity than the low pressure part. This produces a nonlinear propagation distortion of the wave oscillation which accumulates with propagation distance. The nonlinear propagation distortion introduces harmonic frequency components in the propagating pulse and is commonly known as *harmonic self distortion*.

B.2.2 Dual-frequency propagation

Using dual-frequency band pulses, it is convenient to analyze the propagation velocity by separating the pressure into two components, $p = p_m + p_i$, where p_m represents the low-frequency manipulation pulse pressure and p_i the high-frequency imaging pulse pressure [16]. Inserting the pressure components into (C.4) and for clarity dropping the dependency on \underline{r} gives

$$c(p_m, p_i) \approx c_0 (1 + \beta_{na}\kappa_a p_m + \beta_{na}\kappa_a p_i) . \quad (\text{B.10})$$

The last term produces nonlinear harmonic distortion of the imaging pulse while the second to last term will in addition to nonlinear harmonic distortion of the manipulation pulse, give a local change in the wave velocity experienced by the imaging pulse. Defining the propagation velocity of the imaging pulse as

$$c(p_i) = c_0 (1 + \beta_{na}\kappa_a p_i) , \quad (\text{B.11})$$

the change in wave velocity will be proportional to the manipulation pressure p_m , and the modified sound velocity for the imaging pulse may then be expressed as

$$\begin{aligned} c_i(p_m, p_i) &\approx c_i(p_i) (1 + \beta_{na}\kappa_a p_m) \\ &= c_0 \left(1 + \beta_{na}\kappa_a p_i + \beta_{na}\kappa_a p_m + (\beta_{na}\kappa_a)^2 p_i p_m \right) \\ &\approx c_0 (1 + \beta_{na}\kappa_a p_m + \beta_{na}\kappa_a p_i) . \end{aligned} \quad (\text{B.12})$$

where squared term can be neglected since it is low value relative to the other terms, and c_0 is the wave velocity for the imaging pulse with no manipulation pulse present.

For a short imaging pulse compared to the LF period, the manipulation pressure over the HF pulse length can be divided into two components, an average, p_{ma} , and a

varying, p_{mf} , component. Compared to a pulse propagating without any manipulation the average pressure will produce an accumulated nonlinear propagation delay [16],

$$\tau(z) = - \int_0^z \frac{ds}{c_0} \beta_n(s) \kappa(s) p_{ma}(s) . \quad (\text{B.13})$$

The varying part will produce nonlinear distortion of the imaging pulse. For example; an imaging pulse centered at the zero crossing of the manipulation pulse, the pulse will experience zero delay and only nonlinear distortion. The nonlinear distortion will produce compression of the imaging pulse if it is placed on a negative gradient of the manipulation pulse and expansion if it is placed on a positive gradient.

Consider a short imaging pulse compared to the manipulation pulse wavelength; if the imaging pulse is centered at the zero crossing of the manipulation pulse the imaging pulse will experience zero delay and only compression/expansion. After propagating a distance Δz the shift in wavelength will be [14]

$$\Delta\lambda_{HF}(\Delta z) = c_0 \beta_n \kappa \Delta p_{mf} \Delta z , \quad (\text{B.14})$$

where Δp_{mf} is the difference in manipulation pressure between two zero crossings of the imaging pulse. This change in wavelength will produce a shift in center frequency of

$$f_{HF}(z + \Delta z) = \frac{\lambda_{HF}(z)}{\lambda_{HF}(z) + \Delta\lambda_{HF}(\Delta z)} f_{HF}(z) . \quad (\text{B.15})$$

If, on the other hand, the imaging pulse is placed at the peak or trough of the manipulation pulse, the imaging pulse will experience mainly a delay as given by (C.6) but also some nonlinear distortion [16]. The amount of nonlinear distortion will be a function of the length of the imaging pulse relative to the manipulation pulse. The experienced manipulation pressure at the time t from the peak or trough of the manipulation pulse may be modeled as

$$p_{LF}(t) = p_{LF} \cos(2\pi f_{c,LF} t) . \quad (\text{B.16})$$

For a gaussian imaging pulse with relative bandwidth B and center frequency $f_{c,HF}$, the X dB level of the envelope has the position t_{XdB}

$$t_{XdB} = \frac{\sqrt{2 \ln(2)}}{B f_c \pi} \sqrt{\frac{X}{10} \ln(10)} \quad (\text{B.17})$$

Equation (B.16) and (B.17) can be used to compute the relative difference in manipulation pressure between the center and the edges of the HF pulse.

From the nonlinear wave Equation (B.7), the pressure dependent nonlinear scattering coefficient is

$$\frac{\sigma_n(\underline{r}; p)}{c_0^2(\underline{r})} \frac{\partial^2 \varphi(\underline{r}, t)}{\partial t^2} . \quad (\text{B.18})$$

Using SURF imaging and e.g. transmitting two pulse complexes in each direction where the high-frequency pulse travels on the peak or trough of the manipulation pulse, the linear and nonlinear scattering can be separated [7].

B.2.3 Signal Model

The received echo from a pulse with no manipulation pressure can be modeled as a complex bandlimited signal with real positive amplitude, a , center frequency, ω_c and modulating phase, φ

$$s(t) = a(t) e^{i[\varphi(t) + \omega_c t]} \quad (\text{B.19})$$

By applying manipulation pressure and combining the nonlinear wave equation (C.3) and (B.19), the received HF echo from a SURF complex can be modeled as

$$s_k(t) = (a_l(t + \alpha_k \tau(t)) + \alpha_k a_{nl}(t + \alpha_k \tau(t))) e^{i[\varphi(t + \alpha_k \tau(t)) + \omega_c(t + \alpha_k \tau(t))]} \quad (\text{B.20})$$

where α_k is the polarity of the manipulation pressure for pulse k , τ_k is the nonlinear propagation delay, a_l and a_{nl} is the amplitude of the linear and nonlinear signal respectively. By transmitting two pulses in each direction with alternating LF pressure, i.e. $\alpha_{1,2} = [1, -1]$, and estimating and correcting for the nonlinear propagation delay, the linear scattered signal can be suppressed and the nonlinear detected by subtracting the two corrected signals

$$\hat{d}(t) = \hat{s}_1(t - \hat{\tau}(t)) - \hat{s}_2(t + \hat{\tau}(t)) \quad (\text{B.21})$$

B.2.4 Delay estimation

To estimate the nonlinear propagation delay, the algorithm by Standal *et al.* [19] is used. The algorithm uses a crosscorrelation technique to estimate the phase difference of the two signals. It also estimates the instantaneous center frequency and uses a parametric model for the delay. The delay is then found through some minimization procedure, e.g. minimum least squares.

Using the signal model in Equation (B.20) and assuming symmetric delays and unit sampling, the received signal from two SURF pulses with alternating LF polarity can be written as

$$\begin{aligned} s_1[n] &= s[n + \tau_n] \\ &= a[k + \tau_n] \exp\{i(\varphi[n + \tau_n] + \omega_c(k + \tau_n))\} \\ s_2[n] &= s[n - \tau_n] \\ &= a[n - \tau_n] \exp\{i(\varphi[n - \tau_n] + \omega_c(k - \tau_n))\} \end{aligned} \quad (\text{B.22})$$

Cross multiplication gives the phase difference

$$\begin{aligned} \psi_n &= \arg\{s_1[n] \bar{s}_2[n]\} \\ &= \varphi[n + \tau_n] - \varphi[n - \tau_n] + \omega_c \tau_n, \end{aligned} \quad (\text{B.23})$$

which for a small (sub sample) τ_n can be approximated as

$$\psi_n \approx (\dot{\varphi}[n] + \omega_c) \tau_n, \quad (\text{B.24})$$

where $\dot{\varphi}[n] + \omega_c$ is the instantaneous frequency. The instantaneous frequency may be estimated as

$$\begin{aligned} \theta_n &= (\arg \{s_1[n+1]\bar{s}_1[n-1] + s_2[n+1]\bar{s}_2[n-1]\}) \\ &\approx \dot{\varphi}[n] + \omega_c . \end{aligned} \tag{B.25}$$

The following relationship can then be formed

$$\psi_n \approx \theta_n \tau_n \tag{B.26}$$

and the delay is found by some minimization procedure

$$\min_{\hat{\tau}} \|\psi - \theta \hat{\tau}\| . \tag{B.27}$$

In this work, a local linear model for the delay is used

$$\hat{\tau}_{n+\ell} := a_n + b_n \ell \tag{B.28}$$

and the model parameters are found in a least squares fashion by minimizing

$$J(a_n, b_n) = \sum_{\ell} w_{n+\ell} |\psi_{n+\ell} - \theta_{n+\ell} (a_n + b_n \ell)|^2 , \tag{B.29}$$

where w_n is a weighting function, a_n is the local delay and b_n is the local slope of the delay at depth n . Any parametric model can be used for the delay, but the linear model is chosen since the delay varies slowly over the window size and it allows for efficient computation.

B.3 Methods

B.3.1 Scanner

A modified Ultrasonix SonixRP (Ultrasonix Medical Corp, Vancouver, Canada) scanner was used to record the data. The probe used is an inhouse designed dual-frequency linear array manufactured by Vermon (Tours, France). The LF and HF elements are organized in a stack, i.e. the LF elements are behind the HF elements, see Figure C.1 [20]. The probe has 192 HF elements in azimuth direction, while the 156 LF elements are arranged in three rows in elevation with 52 elements each. The outer LF rows are connected in parallel. Only the center LF row covers the HF elements, and each LF element covers 4 HF elements in the azimuth direction. The probe dimensions are listed in Table C.1. In [20] a more detailed description of a similar design is given. The center frequency of the LF and HF part is 0.9MHz and 7.5MHz respectively.

To be able to drive such a probe, the Ultrasonix scanner had to be modified. A 128 channel transmitter has been built for driving the low-frequency part of the array and attached to the scanner. A new probe-connector board was also manufactured due to the extra number of channels.

The Ultrasonix SonixRP scanner is a system designed for research and provides unfiltered beamformed RF data @ 40MHz at full framerate.

	HF	LF
# Elements Azimuth	192	52
# Elements Elevation	1	3
Element Size Elevation	7 mm	7mm
Pitch Azimuth	237 μm	948 μm
Elevation Focus	40 mm	40 mm

Table B.1: Probe Dimensions



Figure B.2: Dual-layer transducer stack with the LF frequency element placed behind the HF elements

B.3.2 Transmit beam setup

For a focused beam from a circular symmetric aperture the diffraction will give a $\lambda/4$ phase shift from the array to the focus [17]. For a linear array the amount of phase shift will be dependent on the azimuth and elevation aperture sizes and foci, and is not as well defined as for the circular symmetric case. The phase shift will be close to that of the circular symmetric case unless the azimuth and elevation foci are very different. Using a focused LF beam the phase between the two pulses will vary along the axis which would contribute to increased compression/expansion.

To limit the compression/expansion and to keep the experienced LF pressure for the HF as constant as possible over the imaging region, an unfocused LF beam is used. But even in the case of an unfocused LF beam there will be diffraction, but this will be limited in the near-field. The limit of the near-field for an unfocused beam using a circular symmetric aperture is given by [17]

$$\frac{D^2}{2\lambda} \tag{B.30}$$

where D is the aperture size and λ is the wave length. This formula can be used as an approximation for the linear array, considering the elevation and azimuth dimension separately. For the setup used here the near-field of the LF aperture is 41mm in the azimuth direction. For the elevation part its more complex since the center row is focused in 40mm. To achieve effective focusing, the focus point should be within the

near field [17]. For the center LF row, the near field is 18mm, so the focusing is not effective, thus the center row can be treated as being unfocused. If assuming that the center row is not focused in elevation for the LF part, the near field limit is 140 mm for the LF in the elevation dimension. It is therefore limited diffraction of the LF beam within the region of interest ($z < 30\text{mm}$), thus the phase relation between the pulses will not vary much in this region. The HF is focused at 22.5mm with an F-number of 2 and the transmit frequencies are 0.9MHz and 8MHz for the LF and HF, respectively.

Voltage	Pressure
0	0 kPa
5	85 kPa
10	150 kPa
20	290 kPa
40	500 kPa

Table B.2: Voltage and pressure levels for low-frequency manipulation pulse

B.3.3 Measurements

For the measurements a CIRS model 049 (CIRS, Virginia, USA) elastography phantom was used. There are no wires or other resolution scatterers in the phantom while the inclusions are deeper than 30 mm, so the part of the phantom which is imaged is homogenous with only ambient scattering. The probe is fixed to a Physik Instruments (Karlsruhe, Germany) multistage robot. One hundred images spaced 1.5 mm apart in the elevation direction are recorded. For each image, 50 frames are recorded and averaged to increase the SNR.

This is done for five pressure levels of the LF manipulation pulse. In Table B.2 the voltage levels together with the calibrated maximum pressure on the axis is shown. The calibrated pressures are derated values from watertank measurements using an attenuation of 0.3 dB/cm/MHz, which is standard for acoustic safety measurements [21].

B.3.4 Simulations

Differences in amplitude, frequency and errors in delay correction will effect the level of suppression. To see how these differences and errors effect the suppression, a 2.5 period 6MHz gaussian pulse is simulated. Different delays, amplitudes and frequency shifts and combinations of these are applied, and the level of suppression computed. The suppression is computed as

$$SUP = 20 \log_{10} \left(\frac{\text{RMS}(x_{\Delta} - x_0)}{\text{RMS}(x_0)} \right) \quad (\text{B.31})$$

where RMS is the root-mean-square value and x_0, x_{Δ} is the non-distorted and distorted signal respectively. Delays of 0.5 and 1.25 ns, amplitude differences of 0.2

and 1.0 dB and frequency shifts of 0.1 and 0.3 MHz are investigated separately. In addition is 1.0 dB and 0.2 dB amplitude difference in combination with a delay off 1.25 ns investigated to analyze the effect of more than one signal parameter.

B.3.5 Processing

The processing was done using MATLAB (The Mathworks, Massachusetts, U.S.A). The received RF data was first filtered with a 60 tap bandpass filter with cutoff frequencies at 3 and 8MHz. The IQ data was produced using the *hilbert* transform in Matlab.

The nonlinear propagation delay between the positively and negatively manipulated pulse is estimated using the algorithm described in Section B.2.4. The window size used was 2.0mm. For correction of the estimated nonlinear propagation delay, cubic spline interpolation was used. The corrected signals were then subtracted to suppress the linear scattered signal as described in Section B.2.3. With reference to the signal model (B.20),(B.21) and using a pulse sequence of $\alpha_{1,2} = [-1, 1]$, the two delay-corrected signals are denoted

$$\begin{aligned}\hat{c}_1(t) &= \hat{s}_1(t - \hat{\tau}(t)) \\ \hat{c}_2(t) &= \hat{s}_2(t + \hat{\tau}(t)) \ ,\end{aligned}\tag{B.32}$$

and the nonlinear detection signal

$$\hat{d}(t) = \hat{c}_1(t) - \hat{c}_2(t) \ .\tag{B.33}$$

The relative tissue suppression (RTS) is then computed as

$$\text{RTS} = \frac{\sum_{k=1}^{100} |\hat{d}(t)|}{\sum_{k=1}^{100} |\hat{c}_1(t)|} \ .\tag{B.34}$$

For the 0V case, no delay estimation and correction is done. This case serves as the benchmark, as it provides the optimal level of suppression.

To analyze the difference between the received signals from the positive and negative manipulated pulse, the relative amplitude difference is useful. It may provide indication of beam difference and nonlinear distortion, especially compression/expansion. The relative amplitude difference (RAD) is computed as

$$\text{RAD} = \frac{\sum_{k=1}^{100} |\hat{c}_1(t)|}{\sum_{k=1}^{100} |\hat{c}_2(t)|} \ .\tag{B.35}$$

B.4 Results

In Table B.4 the suppression levels for the simulated pulses is shown.

In Figure B.3 the nonlinear propagation delay is shown for the different low-frequency voltage levels. The delay is averaged over all $N = 100$ frames. The standard

Case	Suppression
$\Delta\tau = 0.5$ ns	-35.85 dB
$\Delta\tau = 1.25$ ns	-27.89 dB
$\Delta a = 0.2$ dB	-32.66 dB
$\Delta a = 1.0$ dB	-18.27 dB
$\Delta f_c = 0.1$ MHz	-26.8 dB
$\Delta f_c = 0.3$ MHz	-18.02 dB
$\Delta a = 1.0$ dB, $\Delta\tau = 1.25$ ns	-17.57 dB
$\Delta a = 0.2$ dB, $\Delta\tau = 1.25$ ns	-25.57 dB

Table B.3: Suppression values

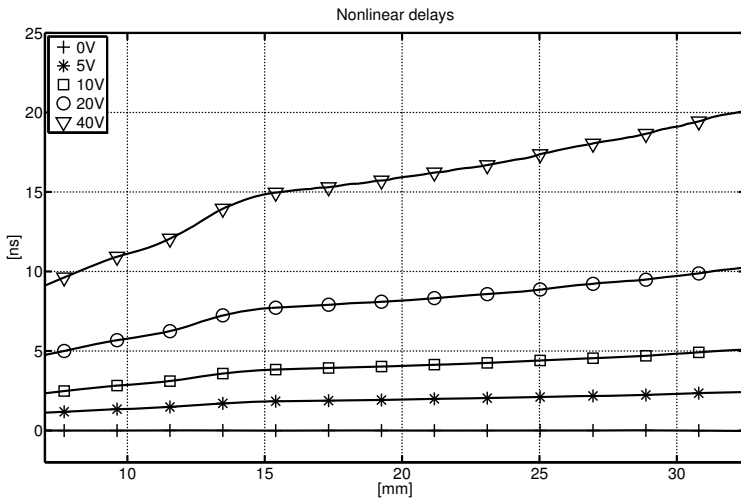


Figure B.3: Estimated nonlinear propagation delays for different low-frequency voltage levels

deviation for the delays over the 100 frames is shown in Figure B.4. The first 7 mm in all plots has been left out, due to near field artifacts with the prototype probe.

In Figure B.5 the relative tissue suppression is shown. The level of suppression decreases with increasing LF manipulation pressure and depth.

When transmitting an unfocused LF wave together with a focused HF wave the phase relation between the HF and LF will vary across the HF beam. The phase relationship across the beam for the setup used here, is shown in Figure B.6, where zero degrees means that the HF is centered at the peak or trough of the LF.

The relative amplitude difference between the received signal from the positive and negative manipulated pulses are shown in Figure B.7.

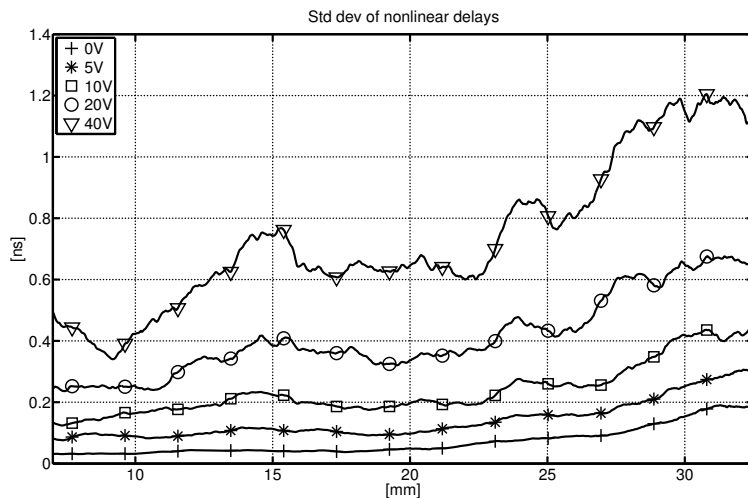


Figure B.4: Standard deviation for the estimated nonlinear propagation delays

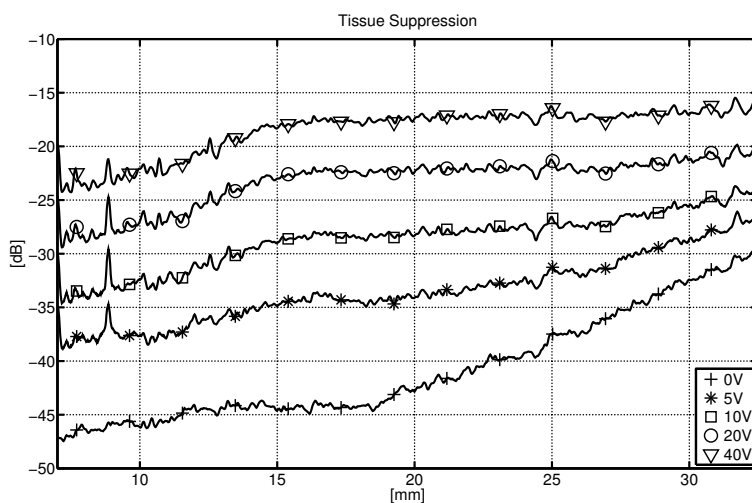


Figure B.5: Level of linear scattering suppression for different voltage levels

B.5 Discussion

When transmitting an unfocused LF wave together with a focused HF wave, the manipulation pressure experienced by the HF pulse varies across the HF beam, producing a variation in the propagation velocity. The variation in phase relation between the HF and LF over the transmit beam is shown in Figure B.6. For the setup used here, the maximum transmit focusing delay is 477 ns, which is approximately 43% of an LF

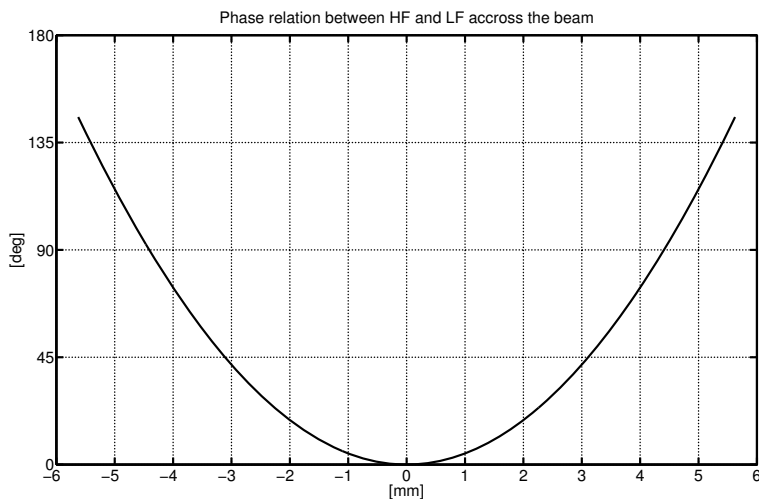


Figure B.6: Phase relation between HF and LF across the beam on transmit

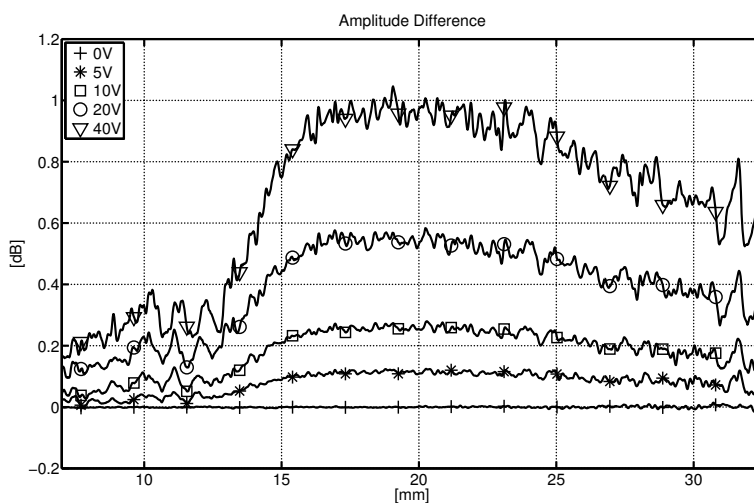


Figure B.7: Amplitude difference between the positively and negatively manipulated pulses

period.

The variable phase relation over the HF beam will produce different nonlinear delays and distortion across the beam. Even though the central part of the HF beam is placed at the peak/trough of the LF pulse and experience little compression/expansion, the outer parts will be propagating on the gradient of the LF producing compression/expansion and more complex nonlinear distortion. Compression/expansion will

produce amplitude differences and frequency shifts. When using focused beams, the edge-waves will have an increasing contribution until the focus, before their contribution decreases again. The amplitude difference in Figure B.7, increases rapidly at around 13-14 mm and decreases after 20 mm. This can be explained by the edge waves which has experienced a higher level of compression/expansion than the central parts of the beam, and has their main region of contribution in this depth range.

The variation in wave velocity over the HF beam will produce nonlinear aberration, and since the manipulation pulse is inverted from the first to the second pulse, the aberration will be different for the two beams. For the positive manipulated beam, the outer edges of the HF beam will propagate slower than the central parts since the manipulation pressure is lower, shifting the focus of the beam outwards, while for the negative manipulated pulse the focus will be shifted inwards. Shift in focus will produce different beam profiles and thus an amplitude difference between the two signals. The depth profile of the amplitude difference in Figure B.7 has the shape of an axis beam-profile which may be an indication that the amplitude difference is produced mainly by the contribution of edge-waves which has experienced compression/expansion rather than aberration.

Aberration will also produce a difference in diffraction which gives a frequency difference between the two signals. From the results in Table B.4, it is seen that the maximum achievable level of suppression for a frequency shift of as little as 0.1 MHz is $\sim 27dB$, while for 0.3 MHz shift, it is $\sim 18dB$. Thus the slightest difference in diffraction and can limit the suppression considerably .

When transmitting an unfocused LF wave, and the HF pulse is placed on the peak or through and it is short compared to the LF pulse, one would expect minimal compression/expansion. The prototype probe has a bandwidth of approximately 45%, so from (B.16) and (B.17) the -10 and -20 dB limit of the HF pulse has a relative experienced LF pressure, $\frac{p_{LF}(t_{XdB})}{p_{LF}(t_0)}$, of ~ 0.61 and ~ 0.27 respectively. The -20 dB length of the HF pulse covers approximately 41% of the LF period. Even for a HF pulse traveling at the peak or through of the LF pulse, such large variation of the LF pressure over the HF pulse might produce significant nonlinear distortion, decreasing the level of tissue suppression.

The standard deviation of the delay estimates shown in Figure B.4 increases both with depth and manipulation pressure. The 0V case gives the optimal level of suppression and indicates the SNR in the system. The SNR decreases with depth, and a lower SNR will give larger errors in the delay estimates and thus make the errors increase. Frequency difference between the two pulses introduced by aberration and nonlinear propagation will increase with increasing manipulation pressure and introduce errors in the delay estimates.

When transmitting an unfocused LF wave the pressure and phase can be assumed to be close to constant within the near-field of the LF beam, which should give a linear relation with depth of the nonlinear propagation delay. As seen in Figure B.3, the estimated delays are linear with a break at around 14 mm. As mentioned above, the nonlinear aberration will produce different diffraction of the positively and negatively manipulated beams. From Figure B.7 the amplitude difference and thus possibly the

difference in diffraction increases at around 14 mm which could effect the delay estimation and introduce a bias. The manipulation pressure decreases from the center of the HF wave to the edges as shown in Figure B.6. Thus, the accumulated nonlinear delay decreases as one moves away from the center of the HF beam. When the edge waves, which has accumulated less nonlinear delay starts contributing to the signal at the center of the HF beam, the observed nonlinear delay will become less than what is expected based on the manipulation pressure on the center of the beam.

The level of tissue suppression shown in Figure B.5, decreases with increasing pressure. Higher manipulation pressure gives increasing delays and delay errors, which suggests that the suppression decreases. The relative amplitude difference shown in Figure B.7 also increases with increasing manipulation pressure giving poorer suppression of the tissue signal. From Table B.4, it is seen that when the amplitude difference is 1 dB, an error in delay correction of 1.25 ns has little influence on signal suppression, so the amplitude difference is the dominating factor, while for a delay error of 1.25 ns, a difference in amplitude of 0.2 dB has only minor effect. The amplitude differences and delay errors used in this analysis are representable for the range of values seen in Figure B.7 and Figure B.4.

The SNR level decreases almost linearly from 18 mm and out while the suppression levels stays more or less constant. This can be attributed to that the relative amplitude difference, shown in Figure B.7, decreases from around 18 mm and deeper, thus improving the level of suppression. When approaching the far-field, the difference in diffraction will also become less, contributing to an improved level of tissue suppression.

B.6 Conclusions

In this paper, suppression of linear scattering for a dual-frequency band technique has been investigated. An unfocused LF beam has been used together with a focused HF beam. The unfocused LF beam was chosen to achieve close to constant phase relationship between the LF and HF pulse and thus close to constant manipulation pressure in the imaging region. Such a setup is expected to produce little compression/expansion of the HF pulse, but introduces other propagation effects like aberration.

The level of tissue suppression for the setup used in this study varies from 35dB to 17dB in the focus. The level decreases for increasing pressure. For contrast imaging where LF pressures in the range 50-120 kPa are common, which corresponds to the 5-10V setting investigated here, the suppression level demonstrated is sufficient. The SURF technique for contrast imaging is demonstrated in vivo [22] in pigs, though with a different system.

For high pressure application, the suppression of linear scattering seen here might not be sufficient. For such applications the aberration and pulse form compression/expansion can not be neglected and must be estimated and corrected for. The beamforming setup investigated here might not be the one producing the optimum level of suppression. Thus, alternative beamforming strategies for minimizing the nonlinear propagation effects should be sought, e.g. confocal LF and HF beams where

both can be focused at the same depth or both unfocused.

Methods for estimating and correcting for the nonlinear propagation effects other than the nonlinear delay should also be investigated. To achieve optimal suppression the pulse form distortion and diffraction differences should be corrected for.

It is shown that when there is an amplitude difference of 1 dB, an error in the delay correction of 1.25 ns yields 0.7 dB less signal suppression than with no delay error. Compared to the case with only 1.25 ns delay error and no amplitude difference, the signal suppression is 10dB less. When there is little amplitude difference, 0.2 dB, it is shown that that the delay has more significant effect. From this analysis it is indicated that for the values of amplitude difference and delay error investigated here, the amplitude difference, which stems from pulse form distortion and aberration, has a greater impact on the level of tissue suppression than the delay error.

References

- [1] D. H. Evans and W. N. McDicken, *Doppler Ultrasound: Physics, Instrumentation and Signal Processing*. Wiley, 2 ed., Feb. 2000.
- [2] D. Simpson and P. Burns, “Pulse inversion doppler: a new method for detecting nonlinear echoes from microbubble contrast agents,” in *Ultrasonics Symposium, 1997. Proceedings., 1997 IEEE*, vol. 2, pp. 1597–1600 vol.2, 1997.
- [3] G. A. Brock-Fisher, “Means for increasing sensitivity in non-linear ultrasound imaging systems,” *The Journal of the Acoustical Society of America*, vol. 101, no. 6, p. 3240, 1997.
- [4] R. J. Eckersley, C. T. Chin, and P. N. Burns, “Optimising phase and amplitude modulation schemes for imaging microbubble contrast agents at low acoustic power,” *Ultrasound in Medicine & Biology*, vol. 31, pp. 213–219, Feb. 2005. PMID: 15708461.
- [5] T. G. Leighton, *The acoustic bubble*. Academic Press, 1997.
- [6] C. X. Deng, F. L. Lizzi, A. Kalisz, A. Rosado, R. H. Silverman, and D. J. Coleman, “Study of ultrasonic contrast agents using a dual-frequency band technique,” *Ultrasound in Medicine & Biology*, vol. 26, no. 5, pp. 819 – 831, 2000.
- [7] B. Angelsen and R. Hansen, “7A-1 SURF imaging - a new method for ultrasound contrast agent imaging,” in *Ultrasonics Symposium, 2007. IEEE*, pp. 531–541, 2007.
- [8] R. Hansen and B. Angelsen, “SURF imaging for contrast agent detection,” *Ultrasonics, Ferroelectrics and Frequency Control, IEEE Transactions on*, vol. 56, no. 2, pp. 280–290, 2009.
- [9] A. Bouakaz, M. Versluis, J. Borsboom, and N. de Jong, “Radial modulation of microbubbles for ultrasound contrast imaging,” *Ultrasonics, Ferroelectrics and Frequency Control, IEEE Transactions on*, vol. 54, no. 11, pp. 2283–2290, 2007.
- [10] M. Averkiou and D. Roundhill, “A new imaging technique based on the nonlinear properties of tissues,” in *Ultrasonics Symposium, 1997. Proceedings., 1997 IEEE*, vol. 2, pp. 1561–1566 vol.2, 1997.

-
- [11] B. Haider and R. Chiao, "Higher order nonlinear ultrasonic imaging," in *Ultrasonics Symposium, 1999. Proceedings. 1999 IEEE*, vol. 2, pp. 1527–1531 vol.2, 1999.
- [12] S. Nasholm, R. Hansen, S.-E. Måsøy, T. Johansen, and B. Angelsen, "Transmit beams adapted to reverberation noise suppression using dual-frequency SURF imaging," *Ultrasonics, Ferroelectrics and Frequency Control, IEEE Transactions on*, vol. 56, no. 10, pp. 2124–2133, 2009.
- [13] C. Cain, "Ultrasonic reflection mode imaging of the nonlinear parameter B/A: a theoretical basis," in *IEEE 1985 Ultrasonics Symposium*, pp. 887–890, 1985.
- [14] H. Fukukita, "Ultrasound pulse reflection mode measurement of nonlinearity parameter B/A and attenuation coefficient," *The Journal of the Acoustical Society of America*, vol. 99, no. 5, p. 2775, 1996.
- [15] D. Zhang and X. Gong, "Experimental investigation of the acoustic nonlinearity parameter tomography for excised pathological biological tissues," *Ultrasound in Medicine & Biology*, vol. 25, pp. 593–599, May 1999.
- [16] R. Hansen, S. Masoy, T. F. Johansen, and B. A. Angelsen, "Utilizing dual frequency band transmit pulse complexes in medical ultrasound imaging," *The Journal of the Acoustical Society of America*, vol. 127, pp. 579–587, Jan. 2010.
- [17] B. Angelsen, *Ultrasound imaging. Waves, signals and signal processing Vol I*. Trondheim: Emantec, 2000.
- [18] B. Angelsen, *Ultrasound imaging. Waves, signals and signal processing Vol II*. Trondheim: Emantec, 2000.
- [19] . Standal, T. Tangen, and B. Angelsen, "P2D-4 a phase based approach for estimation and tracking of locally variable delays," in *Ultrasonics Symposium, 2007. IEEE*, pp. 1583–1585, 2007.
- [20] T. Johansen, J. Deibele, S. Måsøy, R. Hansen, and B. Angelsen, "Design and test of a Dual-Layer, Dual-Frequency SURF array," *Proceedings of the 31st Scandinavian Symposium on Physical Acoustics*, vol. 31, 2001.
- [21] "Information for manufacturers seeking marketing clearance of diagnostic ultrasound systems and transducers." Center for Devices and Radiological Health.
- [22] S. Måsøy, O. Standal, P. Nasholm, T. Johansen, B. Angelsen, and R. Hansen, "SURF imaging: In vivo demonstration of an ultrasound contrast agent detection technique," *Ultrasonics, Ferroelectrics and Frequency Control, IEEE Transactions on*, vol. 55, no. 5, pp. 1112–1121, 2008.

Comparison of beamforming strategies for dual-frequency band imaging using a large frequency separation

Thor Andreas Tangen², Svein-Erik Måsøy¹, Rune Hansen^{1,3}, Amund Skavhaug² and Bjørn Angelsen¹

¹Department of Circulation and Medical Imaging, NTNU, Trondheim, Norway,

²Department of Engineering Cybernetics, NTNU, Trondheim, Norway,

³SINTEF Society and Health, Trondheim Norway

Abstract

In dual frequency band imaging techniques a low frequency (LF) manipulation pulse is used to manipulate the propagation and scattering of a high frequency (HF) imaging pulse. Understanding how the choice of transmit beam setups affects the nonlinear propagation is crucial for optimal performance of the imaging method. Three transmit beamforming strategies have been investigated; 1. Focused LF + Focused HF, 2. Unfocused Wave LF + Focused HF, 3. Unfocused Wave LF + Unfocused Wave HF. On axis pulses are recorded using a watertank setup. The nonlinear delay and frequency shift between pulses with opposite polarity of the LF pulse is estimated. Based on the estimated local LF pressure and pressure gradient experienced by the HF pulse the nonlinear delay and frequency shift is predicted. A good accordance between the predicted and estimated values is seen as long as diffraction is limited. The difference in nonlinear propagation effects between the transmit setups is shown. For the second setup, nonlinear aberration introduces a shift in focusing of the HF beam.

C.1 Introduction

Nonlinear effects in biomedical ultrasound was not widely recognized until Carstensen and Muir focused their attention on this subject in the 1980 [1, 2]. This spawned a wide research effort on nonlinear biomedical ultrasound which led to the development of tissue harmonic imaging [3–5] and techniques for imaging ultrasound contrast agents [6–8].

In recent years, dual-frequency imaging techniques has been a field of some interest. In such techniques, the nonlinear interaction between two co-propagating pulses with different frequency is used for imaging [9–11], tissue characterization [12–14], and to manipulate the scattering properties of ultrasound contrast agents in an effort to increase the sensitivity at high imaging frequencies [?, ?, 15–18].

In [9], dual-band pulse complexes with a large frequency separation is utilized where the low frequency (LF) is used to manipulate the propagation velocity of the high frequency (HF) imaging pulse with the means to suppress reverberation noise. Differential tissue harmonic imaging (DTHI) [11], uses less separation of the frequency bands, e.g. 3 and 6 MHz, and utilizes the mixing of the frequency bands to improve contrast and penetration compared to conventional B-mode imaging.

In vibro acoustography [12], two confocal beams with a slight frequency difference (~ 50 Hz) are used to probe the tissue. In the focus, the nonlinear interaction of the two beams excites an oscillatory movement in the tissue which generates an acoustic signal at the difference frequency, where the phase and amplitude of the emitted signal depends on the mechanical properties of the tissue. This can be used to image micro calcifications in tumors [19].

For contrast imaging, dual-frequency techniques utilizes a LF pulse to manipulate the radius of the micro-bubble and thus manipulate the scattering of the HF imaging pulse. By transmitting two pulse complexes in each scanline direction where the polarity of the low frequency pulse is changed from the first to the second pulse, and subtracting the two received signal, the scattering from the bubble can be detected. In [20] such a dual-frequency contrast imaging technique is demonstrated in vivo.

Dual-frequency methods have also been used to estimate the nonlinearity parameter B/A [13, 14]. In these two methods the LF pulse is used to manipulate the propagation of the HF imaging pulse. The nonlinear propagation of the HF pulse produced by the LF pulse can be estimated and since nonlinear propagation is linked to the nonlinearity parameter, its value can be estimated.

In contrast imaging, the nonlinear scattered signal from the bubble is of interest while the linearly scattered signal from tissue should to be suppressed. As with pulse inversion and other conventional techniques, dual-frequency methods will experience nonlinear propagation which limits the contrast to tissue ratio. In methods like the one presented in [9], it is on the other hand the nonlinear propagation effects which are used for imaging. The generation of nonlinear propagation effects is dependent on the transmit beamforming, so a thorough understanding of this is important to achieve optimal performance of the different imaging techniques.

In this paper the nonlinear propagation effects using dual-frequency band pulse complexes with a frequency separation of 0.9:8 MHz is investigated for three different

transmit beam setups:

- Setup 1: Focused LF + Focused HF
- Setup 2: Unfocused LF + Focused HF
- Setup 3: Unfocused LF + Unfocused HF

The three setups are investigated using a prototype dual-frequency band linear array. The nonlinear propagation produces a propagation delay and frequency shift of the HF pulse relative to a non-manipulated pulse. These two effects are estimated and their relation to the manipulation pressure is investigated by predicting the accumulation of these effects from the experienced LF manipulation pressure by the HF pulse.

For each transmit beam setup, three pulse complexes are investigated; One with no LF manipulation pulse present and two dual-frequency pulse complexes where the LF pulse is inverted for the second pulse.

C.2 Theory

C.2.1 Nonlinear wave equation

A general derivation of the nonlinear wave equation with scattering terms can be found in [21, 22]. In [23] a condensed version of this is provided. Here, a brief derivation of this equation for a homogeneous medium is presented. The notation follows Angelsen [23].

In the nonlinear regime the relative volume compression of a small material element ΔV is in the 2nd order approximation defined as

$$\frac{\partial V}{\Delta V} = -\nabla\psi(\underline{r}, t) \approx \kappa p - \beta_n \kappa^2 p^2 \quad (\text{C.1})$$

where ψ is the particle displacement, κ is the tissue compressibility, β_n is the tissue nonlinearity parameter, p is the pressure, and \underline{r} is the spatial position. Applying Newtons 2nd law on the element with mass $\Delta m = \rho_0 \Delta V$, the net force on the element will give an acceleration of

$$\frac{\partial u(\underline{r}, t)}{\partial t} = -\frac{1}{\rho_0} \nabla p(\underline{r}, t) \quad (\text{C.2})$$

where u is the element velocity and ρ_0 is the mass density at equilibrium.

Combining (C.1) and (C.2) gives the nonlinear wave equation for homogenous tissue.

$$\nabla\psi(\underline{r}, t) - \frac{1}{c^2(\underline{r}, t)} \frac{\partial^2 \psi(\underline{r}, t)}{\partial t^2} - h_p \otimes_t \frac{1}{c_0^2(\underline{r})} \frac{\partial^2 \psi(\underline{r}; t)}{\partial t^2} = 0 \quad (\text{C.3})$$

where the convolution term is frequency dependent attenuation and $c(\underline{r}, t)$ is the nonlinear wave propagation velocity

$$\begin{aligned} c(\underline{r}, t) &= c_0 \sqrt{1 - 2\beta_n \nabla \psi(\underline{r}, t)} \\ &\approx c_0 (1 - \beta_n \kappa p(\underline{r}, t)) \end{aligned} \quad (\text{C.4})$$

where $c_0 = \frac{1}{\sqrt{\kappa\rho}}$ is the linear wave velocity and the second order term from (C.1) is neglected due to its low magnitude.

C.2.2 Dual-frequency propagation

The local experienced LF pressure and the local variation of the LF pressure over the HF pulse gives a nonlinear delay and compression/expansion of the HF pulse.

When investigating propagation effects of overlapping dual-frequency band complexes it is convenient to divide the pressure into two components; p_i , the high-frequency imaging pressure and, p_m the low-frequency manipulation pressure. Inserting this into (C.4) gives

$$c(p_i, p_m) = c_0 (1 - \beta_n \kappa p_i + \beta_n \kappa p_m) \quad (\text{C.5})$$

where the spatial and temporal dependency of the pressure components are omitted for notational convenience. The last two components gives nonlinear harmonic distortion of the HF and LF pulse respectively. The nonlinear self distortion of the LF pulse also produces a delay and compression/expansion of the HF pulse. The manipulation pressure varies over the HF pulse, and can be divided into two components; p_{ma} , an average and; p_{mf} , a varying component. The average component produces a nonlinear propagation delay compared to a non-manipulated HF pulse

$$\tau_n(z) = - \int_0^z \frac{ds}{c_0} \beta_n(s) \kappa(s) p_{ma}(s) \quad (\text{C.6})$$

while the varying component produces compression/expansion of the HF pulse. Let Δp_{mf} be the difference in manipulation pressure between two zero crossings of the HF pulse. Then, after propagating a distance Δz , the change in wavelength will be

$$\Delta \lambda_{HF}(\Delta z) = \beta_n \kappa \Delta p_{mf} \Delta z \quad (\text{C.7})$$

which gives a change in center frequency of

$$f_{HF}(z + \Delta z) = \frac{\lambda_{HF}}{\lambda_{HF} + \Delta \lambda_{HF}(\Delta z)} f_{HF}(z) \quad (\text{C.8})$$

Consider a symmetric HF pulse which is short compared to the LF period. If the HF is centered at a zero crossing of the LF, the varying LF pressure will produce a compression/expansion of the HF. If placed at the peak or trough, the HF pulse length will not change, but the pulse will be compressed/expanded internally.

When the HF and LF beam is not co-focused another nonlinear propagation effect is introduced, aberration. Since the two beams are not co-focused the experienced LF pressure by the HF pulse varies over the beam, i.e. the sound of speed varies.

Considering the case of an unfocused LF beam with no diffraction together with a HF beam focused at F , and tracing rays from the focus to the array at an angle, α , relative to the beam axis, the accumulated nonlinear propagation delay along this ray is

$$\begin{aligned}\tau_n(F; \alpha) &= \gamma \int_0^F \frac{ds}{\cos \alpha} \cos(k_L [(F-s)(1-\cos \alpha) + z_0]) \\ &= \gamma \frac{F}{\cos \alpha} \frac{\sin(k_L [F(1-\cos \alpha) + z_0]) - \sin(k_L z_0)}{k_L F (1-\cos \alpha) \cos(k_L z_0)}\end{aligned}\quad (\text{C.9})$$

where $\gamma = -\frac{\beta_n \kappa p_L}{c_0}$, $z_0 = c_0 t_0$ is the phase relation between the HF and LF at the center of the beam, and $k_L = \frac{\omega_L}{c_0}$ is the LF wave number.

For a HF centered at the peak of the LF, i.e. $z_0 = 0$, the nonlinear steering delay is

$$\begin{aligned}\tau_{ns}(\alpha) &= \tau_n(\alpha; F) - \tau_n(0; F) \\ &= -\gamma F \left\{ 1 - \frac{\sin(k_L F (1-\cos \alpha))}{k_L F \cos(\alpha) (1-\cos \alpha)} \right\}\end{aligned}\quad (\text{C.10})$$

The ordinary transmit focusing delay is

$$\tau_s(\alpha) = \frac{F}{c_0} \left(\frac{1-\cos \alpha}{\cos \alpha} \right)\quad (\text{C.11})$$

and the total steering delay then becomes

$$\tau_{ts}(\alpha) = \tau_s(\alpha) + \tau_{ns}(\alpha)\quad (\text{C.12})$$

Combining (C.10) and (C.11), the equivalent focus becomes

$$F_{eq}(\alpha) = F - \tau_{ns}(\alpha) \frac{c_0 \cos \alpha}{(1-\cos \alpha)}\quad (\text{C.13})$$

For a focus depth of 20 mm and an F number of 3, the maximum angle is $\alpha = 9.5^\circ$, and using material parameters for muscle at 37°C [24] and a manipulation pressure of 0.5 MPa, the effective focus for the outer ray is 21.1 mm.

The nonlinear focusing delay accumulates with depth, so the effective focal depth changes while the wave is propagating forward. In addition will the nonlinear steering delay vary across the beam, meaning that the focusing will not longer be spherical and the effective focus is not trivial to determine.

Diffraction produces a phase shift of the propagating pulse. For a circular focused aperture, the pulse at the focus depth F , is the spatial derivative of the excitation pulse $f(t)$ [21],

$$\hat{p}(\omega, F) = i\omega \hat{f}(\omega) \rho U_n \frac{e^{ikF}}{2\pi F} A\quad (\text{C.14})$$

where $k = \frac{\omega}{c}$ is the wave number, U_n is the normal velocity on the transducer and A is the vibrating surface area. That is, the pulse will have a $\lambda/4$ phase shift from the

transducer to the focus. This means that the phase relationship between the LF and HF pulse will vary with depth. Using confocal beams, the HF will have to be centered at the zero crossing of the LF at the array surface in order to be at the peak or trough at the focus. For a linear array the amount of phase shift from the transducer to the focus is not as clear as for a circular symmetric case and will be dependent on the azimuth and elevation foci and apertures, but it will in general be less.

C.3 Methods

C.3.1 Scanner

For the measurements, a modified Ultrasonix (Ultrasonix Medical Corp., Vancouver, Canada) SonixRP system was used. In order to transmit dual-frequency band pulses, a low frequency transmit frontend was manufactured and attached to the system. For integration of the LF frontend and the SonixRP system, a new probe connector board was also made. The LF transmit frontend is controlled from the PC on the scanner.

In order to transmit dual-frequency band pulse complexes, a prototype transducer was used. The transducer is designed at the Department of Circulation and Medical Imaging, NTNU, and manufactured by Vermon (Tours, France). The LF part of the array is located behind the HF part, forming a dual layer stack, see Figure C.1 [25]. The LF elements covers four HF elements in the azimuth direction and have the same dimension as the HF elements in the elevation direction. The LF part has in addition three rows in the elevation direction, making the LF aperture three times as large as the HF part. The HF part and the center LF row is refocused at 40 mm in elevation with a lens. The probe specifications are listed in Table C.1



Figure C.1: Dual-layer transducer stack with the LF frequency element placed behind the HF elements [25]

The Ultrasonix SonixRP scanner is designed for research and provides unfiltered data @ 40MHz at full frame rate.

	HF	LF
# Elements Azimuth	192	52
# Elements Elevation	1	3
Element Size Elevation	7 mm	7mm
Pitch Azimuth	237 μm	948 μm
Elevation Focus	40 mm	40 mm

Table C.1: Probe Dimensions

C.3.2 Transmit beam setup

In this study three different transmit beamforming strategies was investigated:

- Setup 1: Focused LF + Focused HF
- Setup 2: Unfocused LF + Focused HF
- Setup 3: Unfocused LF + Unfocused HF

When using dual-frequency band pulse complexes, a certain phase relationship between the HF and LF pulse is desirable. The optimal phase relation is application dependent, *e.g.* for reverberation suppression [9] the experienced pressure should be low in the near-field and increase as the pulses approaches the imaging region, while for imaging of microbubbles the optimal phase relationship is dependent on the resonance frequency of the bubble. The optimal phase relationship can also be the one *e.g.* minimizing or maximizing the nonlinear propagation effects.

For the setups investigated here, the phase relation at transmit is adjusted so that the HF is at the peak or trough of the LF in the HF focus. For Setup 3, the calibration is done in the depth corresponding to the focus depth of HF in the other setups.

The intention of transmitting an unfocused LF is to achieve a more or less constant phase relationship between the HF and LF within the imaging region. For the focused beam, diffraction will produce a phase shift from the transducer to the focus, as described in section C.2.2, and produce a depth varying phase relationship. The HF is said to "slide" along the LF pulse. There will be diffraction also for the unfocused wave cases, but the diffraction within the near field of the beam will be limited. For a beam from a circular symmetric aperture the near field limit is

$$\frac{D^2}{2\lambda} \tag{C.15}$$

where D is the diameter of the aperture. By choosing the aperture of the LF so that the imaging region of the HF falls within the near field of the LF, there will be a more or less constant phase relationship between the two pulses. The center row of the transducer has a fixed elevation focus which will give some diffraction of the LF, even within the near field.

When transmitting a focused HF together with an unfocused LF beam, the phase relation over the HF beam will vary, producing nonlinear aberration. To avoid this

aberration, an unfocused HF can be transmitted together with an unfocused LF. This is a special case of the confocal setting where the two beams are focused in infinity. For imaging, transmitting an unfocused HF wave will limit the lateral resolution, but this can be compensated for by applying spatial compounding techniques [26].

For the focused beams, the focal depth is set to 20 mm. For the HF, an aperture of 6.4 mm was used for all setups, which gives an F-number of 2.7 for the focused setups. For the LF, an azimuth aperture of 13.2 mm was used, which gives an F-number of 1.5 for the focused setup. For the unfocused wave cases the azimuth near field limit is 59 mm. For the unfocused LF cases, all LF elevation rows were activated, giving an elevation aperture of 21 mm, while for the focused LF case only the center row was activated. The transmit frequencies are 0.9 and 8.0 MHz for the LF and HF respectively. Even though the elevation near field limit is 133 mm, there will as mentioned above be some diffraction of the LF since the center row is focused in the elevation direction.

The transmit pressures were calibrated in order for the LF pressure to be the same at 20 mm for all cases, and since the phase relation at transmit was calibrated to have the HF at the peak of the LF at 20 mm, the experienced LF pressures at this depth is also the same for all settings.

C.3.3 Water tank Measurements

For the water tank measurements, an 85 μm ONDA HGL-0085 hydrophone with a 20-dB pre-amplifier was used (Onda Corporation, Sunnyvale, U.S.A.). The hydrophone was fixed to a Physik Instruments (Karlsruhe, Germany) multi-stage robot and the pulses were recorded using a LECROY WaveSurfer 42Xs (LeCroy, Geneva, Switzerland) oscilloscope. The whole setup was controlled using an in-house developed software programmed in MATLAB (The Mathworks, Massachusetts, U.S.A.).

Axis scans and azimuth beam profile scans were recorded for each setup. For each setup a positively, negatively and non-manipulated scan was recorded. The axis scans were performed by measuring the acoustic pulse along the beam axis in the depth interval [3,35] mm at 0.25 mm steps. The beam profile scans were performed by recording the acoustic pulses in the azimuth positions [-3.5,3.5] mm at 0.25 mm steps at a depth of 20 mm. The data was recorded using a sampling frequency of 500MHz and 64 recordings were averaged for each position.

C.3.4 Processing

All processing was done using MATLAB (The Mathworks, Massachusetts, U.S.A.).

The recorded pressure pulses were filtered using a 500 tap bandpass filter with cutoff frequencies [3,10] MHz and [0.1 2] MHz for the HF and LF respectively.

The phase relation between the HF pulse and the LF pulse was found as the time difference between the maximum of the HF pulse envelope and the closest LF peak.

The experienced LF manipulation pressure by the HF imaging pulse was computed as the weighted average of the LF pressure over the HF pulse, using the HF pulse envelope as the weight. The experienced LF pressure gradient was computed

as the weighted average of the time derivative of the LF pulse over the HF pulse and multiplied with the HF period. The time derivative of the LF pressure was computed as the first difference of the LF pulse.

The nonlinear propagation delay was estimated by finding the max of the cross correlation function. To achieve sub sample accuracy the final delay was found by cosine interpolation around the peak. To compute the predicted nonlinear propagation delay, the estimated experienced LF pressure was used together with equation (C.6), and the material parameters for water at 23 °C [24]

$$\check{\tau}_n(z_i) = \frac{\beta_n \kappa}{c_0} \sum_{k=0}^{k=i} [\hat{p}_{ma,+}(z_k) - \hat{p}_{ma,-}(z_k)] \Delta z. \quad (\text{C.16})$$

where $\hat{p}_{ma,+}$ and $\hat{p}_{ma,-}$ is the estimated experienced LF pressures for the positively and negatively manipulated HF pulses respectively. Note that $\check{\cdot}$ denotes predicted value while $\hat{\cdot}$ denotes estimated value.

The HF center frequency for the pulses was computed as the weighted average of the amplitude spectrum, using

$$\hat{f}_{+/-}(z_i) = \frac{1}{2\pi} \frac{\sum_{k=K_1}^{K_2} \omega_k |X_{+/-}(\omega_k; z_i)|}{\sum_{k=K_1}^{K_2} |X_{+/-}(\omega_k; z_i)|} \quad (\text{C.17})$$

where K_1 and K_2 corresponds to the indexes of the -20 dB limits of the spectrum and $+/-$ denotes the polarity of the manipulation pulse. The pulses were windowed using a hamming window of length 450 samples, centered at the maximum of the HF pulse envelope to make the spectrums smooth. The center frequency shift was computed as the difference in estimated center frequency between the positively and negatively manipulated pulses.

The shift in wave length from depth to depth, $\Delta\hat{\lambda}_{+/-}(z_i)$, was computed according to equation (C.7), where Δp_{mf} is the estimated experienced LF pressure gradient multiplied with the HF pulse period. The predicted center frequency from depth to depth was then computed as

$$\check{f}_{+/-}(z_i + \Delta z) = \frac{\check{\lambda}_{+/-}(z_i)}{\check{\lambda}_{+/-}(z_i) + \Delta\hat{\lambda}_{+/-}(\Delta z)} \check{f}_{+/-}(z_i) \quad (\text{C.18})$$

where $\check{\lambda}_{+/-}(z_i) = \frac{c_0}{\check{f}_{+/-}(z_i)}$, $\Delta\hat{\lambda}_{+/-}(\Delta z) = \beta_n \kappa \Delta \hat{p}_{mf} \Delta z$ and the frequency shift was computed as

$$\Delta\check{f}(z_i) = \check{f}_+(z_i) - \check{f}_-(z_i) \quad (\text{C.19})$$

The axis and beam profiles for the HF imaging pulses were computed as the maximum of the pulse envelope at each position.

C.4 Results

In Setup 2, the focus depth is different for the two beams, so the phase relation between the HF and LF will vary across the HF beam. In Figure C.2 the phase relation between the HF and LF across the beam, relative to the center of the HF beam is shown.

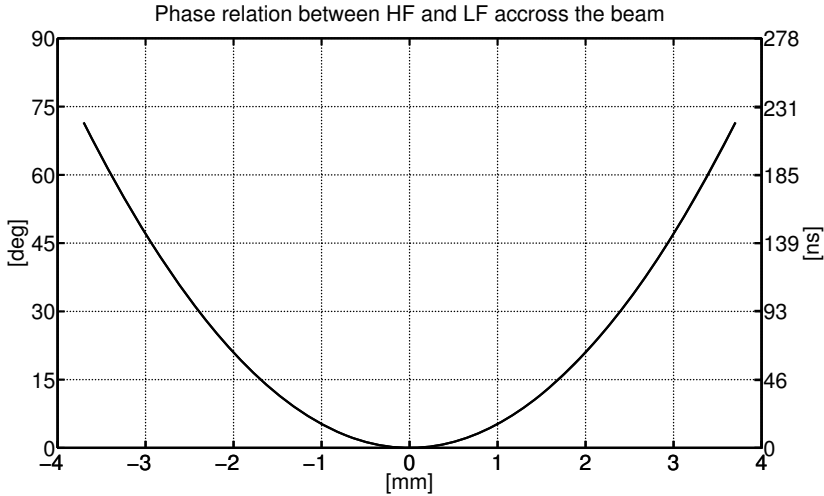


Figure C.2: Phase relation between the HF imaging pulse and the LF imaging pulse across the HF beam at transmit for Setup 2.

In Figure C.3 the estimated phase relation between the HF imaging pulse and LF manipulation pulse is shown. The phase relation is shown in degrees relative to the manipulation pulse period and in nanoseconds. Zero degrees means that the imaging pulse is centered at the peak of the manipulation pulse. The timing between the two pulses was calibrated so that the phase relation between the two pulses was zero at 20 mm. The resolution of the delay adjustment on the scanner is 25 ns, which is 8 degrees relative to the manipulation pulse period, and for all beam setups the difference in phase relation at 20 mm is seen to be less than the resolution of the system.

The LF axis profiles are shown in Figure C.4.

The estimated LF manipulation pressure experienced by the HF pulse is shown in Figure C.5. The experienced LF pressure depends on the LF pressure and the position of the HF relative to the LF pulse. Note that at 20 mm, the experienced manipulation pressure is approximately the same for the three setups, since the phase is calibrated to be zero at this depth.

The nonlinear distortion of the HF imaging pulse by the LF manipulation pulse is produced by the experienced manipulation pressure gradient. The experienced manipulation gradient is shown in Figure C.6, and is shown as the pressure difference over a period of the HF pulse.

The estimated nonlinear propagation delay is shown together with the predicted nonlinear propagation delays in Figure C.7. The predicted curves are marked with circles. The predicted curves for Setup 2 and 3 more or less coincide since the experienced pressure is almost equal for these two setups.

The estimated center frequencies for the positive-(Pos), negative-(Neg) and non-(Zero) manipulated HF pulses is shown in the upper panels of Figure C.8, C.9 and C.10.

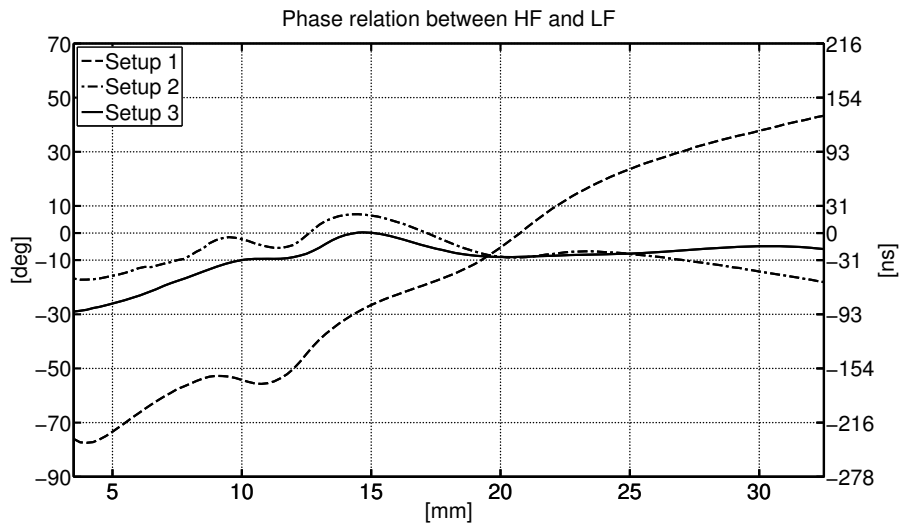


Figure C.3: Phase relation between the HF imaging pulse and the LF imaging pulse.

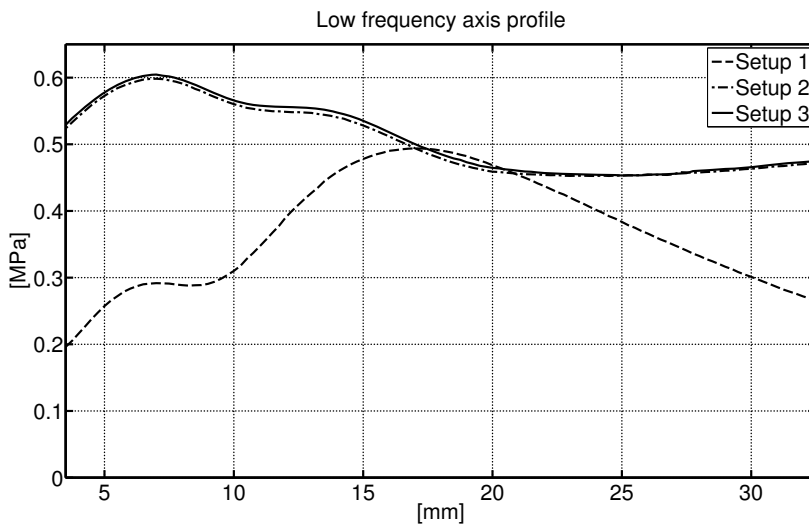


Figure C.4: LF manipulation pressure axis profile

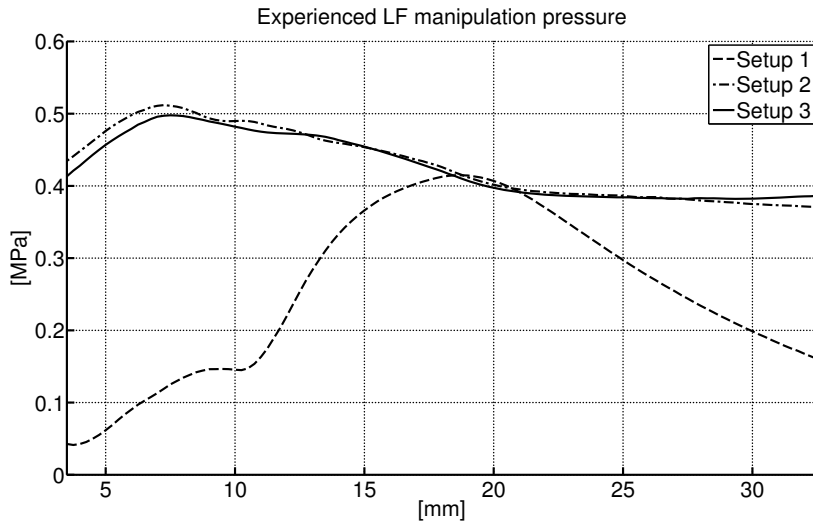


Figure C.5: LF manipulation pressure experienced by the HF imaging pulse

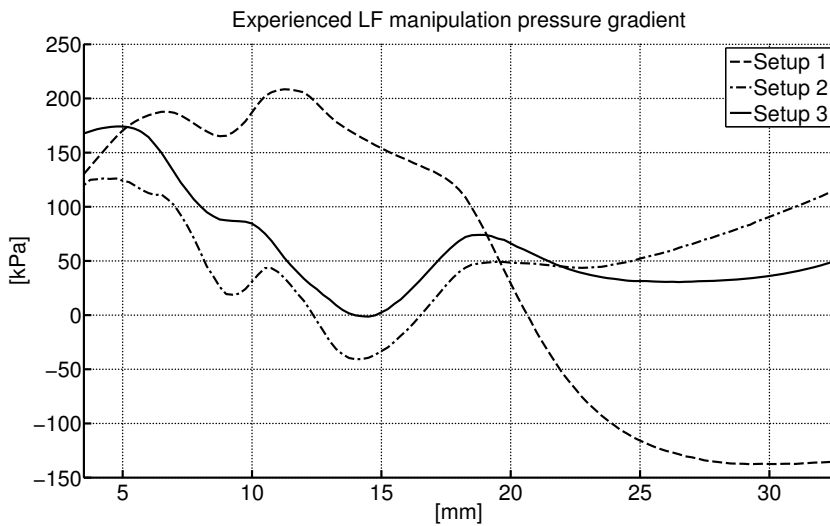


Figure C.6: LF manipulation pressure gradient experienced by the HF imaging pulse

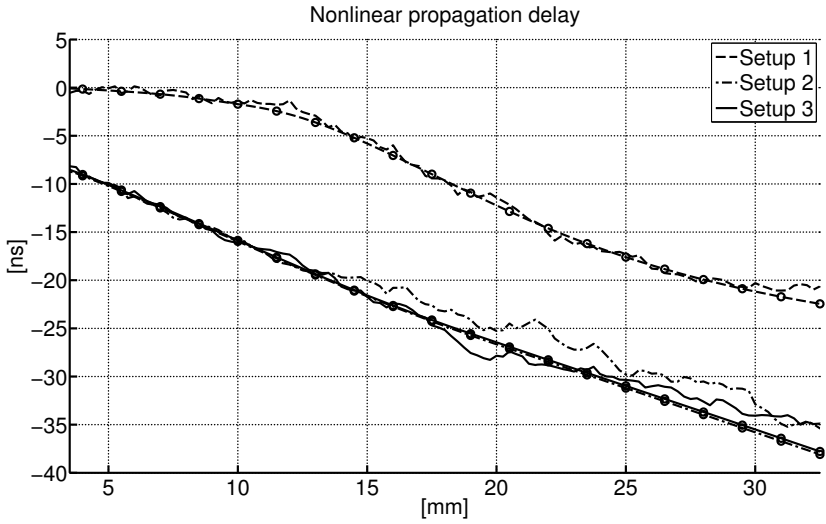


Figure C.7: Estimated and predicted nonlinear delay curves.

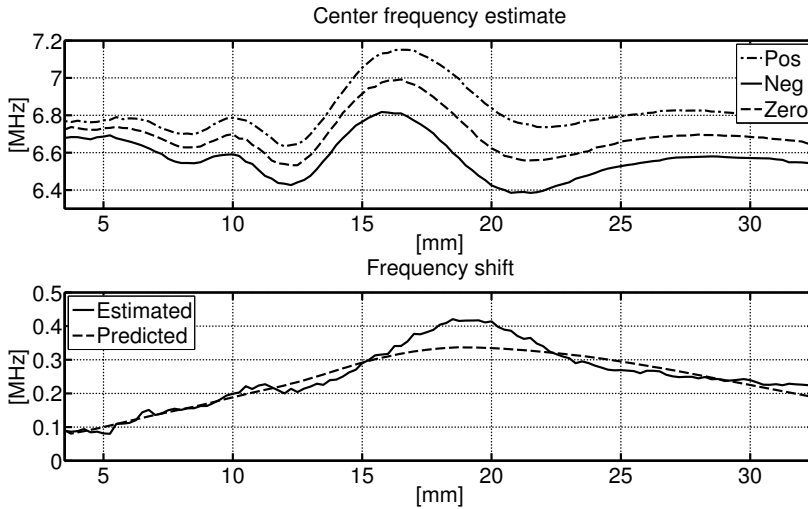


Figure C.8: Estimated center frequencies for Setup 1. Lower Panel: Estimated and predicted center frequency shifts.

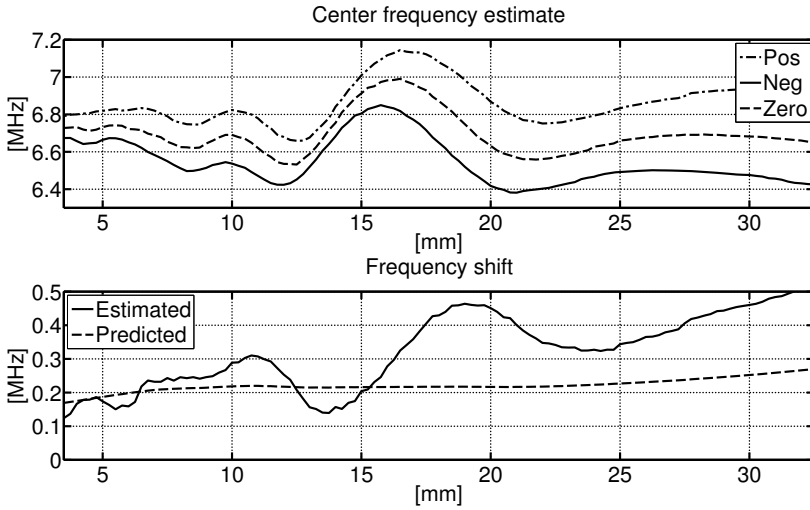


Figure C.9: Estimated center frequencies for Setup 2. Lower Panel: Estimated and predicted center frequency shifts.

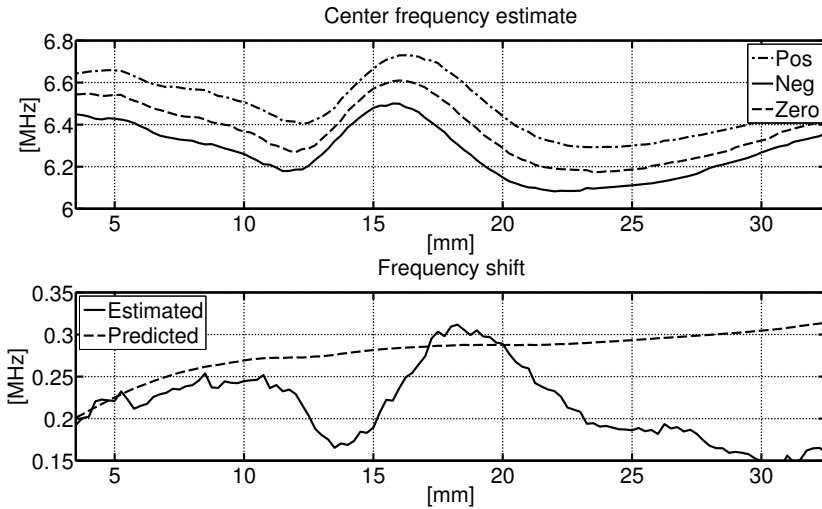


Figure C.10: Upper panel: Estimated center frequencies for for Setup 3. Lower Panel: Estimated and predicted center frequency shifts.

The difference in estimated center frequency between the positively and negatively manipulated pulses is shown in the lower panels of the same figures together with the predicted values based on the experienced LF pressure gradient.

One thing to notice in the figures of the nonlinear delay and center frequency shifts is the values at 3 mm. For the nonlinear delay, the accumulated delay for Setup 2 and 3 is 8 ns at 3mm. This indicates a much greater accumulation for the first 3 mm than for the following depths. This strong accumulation at shallow depths can be due to strong nonlinear propagation within the probe or nonlinear behavior of the HF piezo elements. The same can be seen for the estimated center frequencies, where the difference is ~ 0.2 MHz at 3 mm, which is a much greater accumulation than what is seen over the following depths. So the shifts in center frequency might not be as large as observed in the measurements.

The nonlinear propagation effects and the nonlinear aberration will produce different HF beams. The HF axis profiles are shown in Figure C.11, C.12 and C.13 for Setup 1, 2 and 3 respectively. The azimuth beam profiles for $z = 20$ mm for the three transmit settings are shown in Figure C.14, C.15 and C.16 respectively.

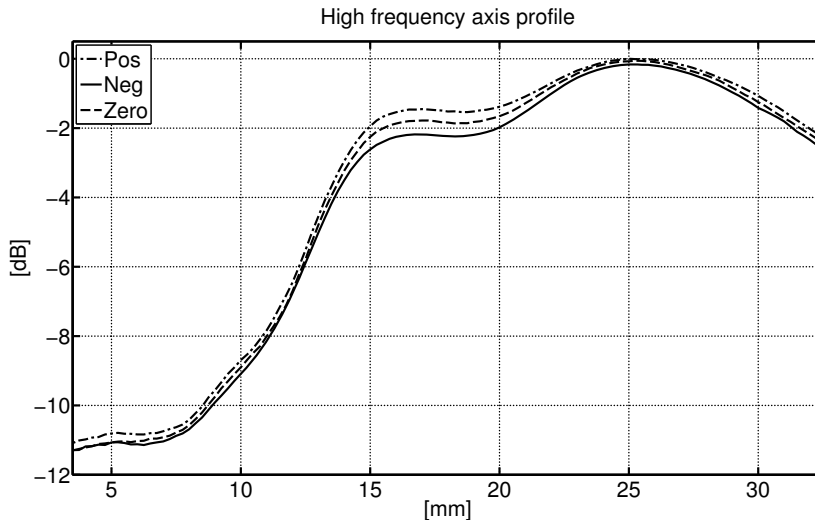


Figure C.11: Axis profile of the imaging pulse for Setup 1.

From the azimuth beam profiles, the beam width can be estimated. The beam width is defined as the -6dB width of the beam and is listed in Table C.2.

C.5 Discussion

The phase relationship between the LF manipulation pulse and the HF imaging pulse was calibrated to be zero at 20 mm. From Figure C.3 the phase relation is seen to be

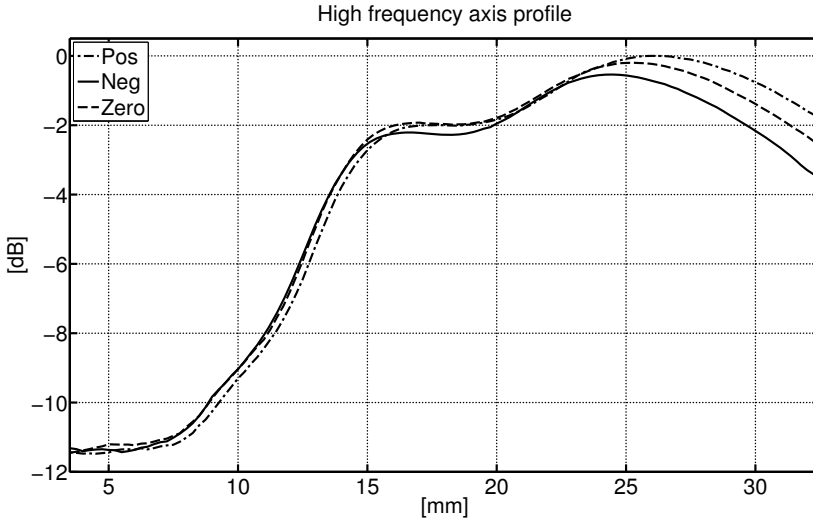


Figure C.12: Axis profile of the imaging pulse for Setup 2.

Setup	Pos	Zero	Neg
1	0.851 mm	0.863 mm	0.881 mm
2	0.826 mm	0.863 mm	0.905 mm
3	5.309 mm	5.366 mm	5.394 mm

Table C.2: Estimated -6dB beam widths

around -10 to -25 ns at 20 mm, which is within the resolution of delay control of the system, which is 25 ns.

It is seen that the phase relation between the HF and LF pulse for Setup 2 and 3 varies in the range $[-15, 8]$ and $[-30, 0]$ degrees of the LF respectively. If the LF had been an actual plane wave, the phase relation should have been constant. Limited aperture and the fact that the center row is focused in the elevation direction produces diffraction of the LF within the depth region, which produces a phase shift. The transmitted LF wave is the same for Setup 2 and 3 but the phase relations are not the same. This can be explained by that the transmitted HF is different for the two setups, which produces a different phase relation as defined by the weighted average over the HF envelope.

For Setup 1, a phase shift of 70-75 degrees from 3 mm to the focus is seen. From the analysis of a circular symmetric aperture, a 90 degree phase shift is expected, but since the elevation and azimuth focus depths are different this can not be expected for the linear array. But even so, there is substantial change in phase relation from the array to the focus. The HF is close to centered at the zero crossing of the LF near the array and slides up to the peak in the focus and continues to slide further after the focus. The sliding will continue until the pulses reaches the far field.

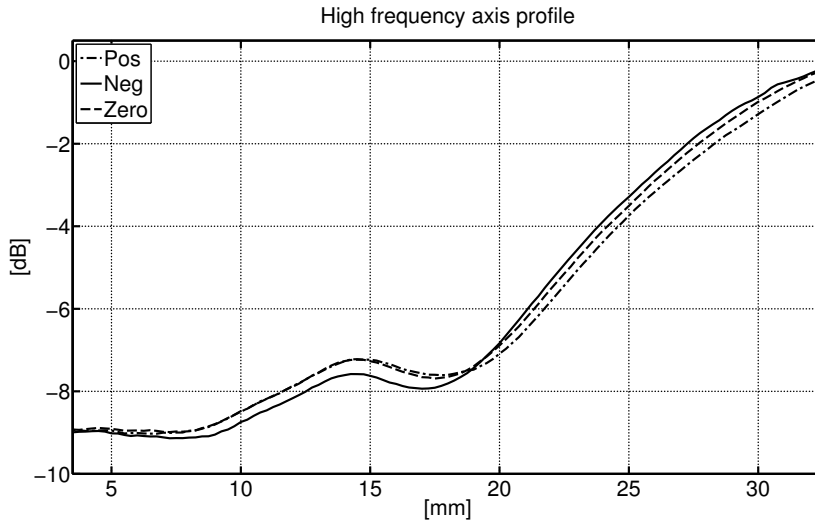


Figure C.13: Axis profile of the imaging pulse for Setup 3.

The transmitted LF pressure was calibrated such that the experienced LF pressure should be the same at 20 mm for all transmit settings, and from Figure C.5 it is seen that the pressure is close to equal at this depth.

The experienced LF pressure at each depth is a function of the LF pressure and the phase relation between the HF and LF pulse. From the experienced LF pressure shown in Figure C.5, one can see that for Setup 2 and 3 the experienced pressure is close to equal since the phase relationships for the two settings are almost the same. In the depth range [3,35] mm the experienced pressure varies from 390 to 510 kPa, which is less than a 2.5dB variation.

For the confocal setting, the experienced LF pressure increases from 3 mm to 18 mm. In this region the LF pressure increases while the HF pulse slides towards the top of the LF, both contributing to an increased experienced LF pressure. After focus the LF axis pressure decreases while the HF slides over the top of the LF thus experiencing a decreasing LF pressure.

The experienced LF pressure produces a nonlinear propagation delay, which can be estimated from the HF pulses and also predicted with knowledge of the material parameters. From Figure C.7 it is seen that for Setup 1 there is a good accordance between the estimated and predicted nonlinear delay. For this setting the relation between the nonlinear propagation delay and experienced pressure is well defined, and the delay can be predicted from the experienced pressure as long as the material parameters are known.

For Setup 2 the discrepancy between the estimated and predicted delay starts at around 12.5 mm. For this Setup the discrepancy can be due to several factors. When transmitting a focused HF together with an unfocused LF wave, the phase relation

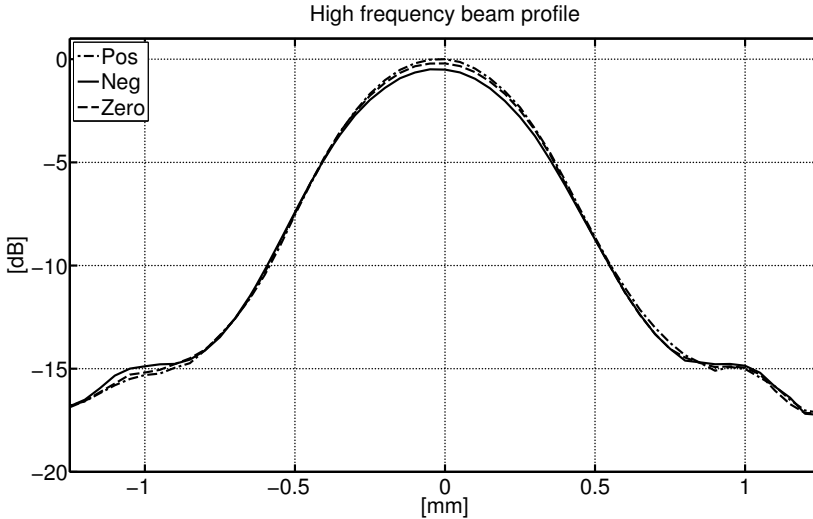


Figure C.14: Beam profile in $z = 20$ mm, of the imaging pulse for Setup 1.

and thus the experienced LF pressure will vary over the beam as seen in Figure C.2. The experienced LF pressure decreases off the axis, so these pulses have accumulated less nonlinear delay. The recorded pulse on the axis is a sum of pulses coming from different parts of the array, which has experienced different manipulation, but the predicted nonlinear delay is based on the experienced pressure on the axis, thus the value of the predicted nonlinear delay will be larger than the estimated delay. Another effect is the nonlinear aberration which shifts the focus of the positively and negatively manipulated beams relative to each other. This refocusing of the beam will produce different diffraction patterns, and since diffraction produces an incremental phase shift in the propagating pulse, this difference in phase shift can be observed as a false delay. From the upper panel of Figure C.9 the peaks in the center frequency estimates are shifted in depth relative to each other, which in addition to the shift in depth of the peak axis pressure seen in Figure C.12, is an indication of difference in diffraction.

For Setup 3 there is a good accordance between the estimated and predicted delays until 17.5 mm. At this depth the estimated delays increase relative to the predicted delay, before it crosses the predicted curve at 22.5 mm and accumulates at a slower rate until 35 mm. From the estimated center frequencies in the upper panel of Figure C.10, it is clear that there is a difference in diffraction between the two pulses; the peaks in the center frequencies at 17.5 mm is shifted in depth for the positively and negatively manipulated pulse, which indicates that the diffraction patterns for the two pulses are different. As mentioned above, diffraction produces a phase shift in the propagating pulse and if the diffraction patterns are different for the two pulses, this difference can introduce a false delay.

The noise in the estimated delay is assumed to be due to vibrations of the watertank

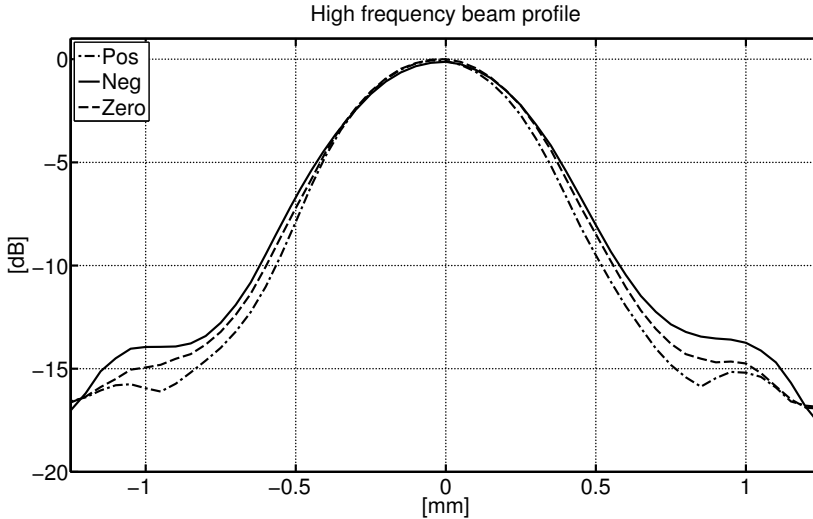


Figure C.15: Beam profile in $z = 20$ mm, of the imaging pulse for Setup 2.

and errors in positioning of the robot. When performing consecutive axis scans the robot is not placed at exactly the same position each time, introducing an error in the estimated delays.

The average experienced LF pressure over the HF pulse is said to produce a nonlinear propagation delay while the varying manipulation pressure produces a distortion of the pulse. If the experienced pressure gradient is constant over the HF pulse, this distortion will be a shift in frequency. If the variation of the LF pressure is more complex so will the distortion be.

For Setup 1, the gradient shown in Figure C.6, increases until ~ 12 mm and then decreases until it stabilizes at around 30 mm. The experienced gradient crosses zero close to 20 mm, which is as expected since the HF pulse is calibrated to be at the peak of the LF at this depth. In the lower panel of Figure C.8, the estimated together with the predicted center frequency shift is shown. It is seen that there is a good accordance between the estimated and predicted frequency shifts until ~ 12 mm. At this depth it can be seen from the upper panel of Figure C.8, that diffraction effects becomes significant. From the estimated center frequency from the non-manipulated pulse, it is seen that the diffraction introduces variations of the center frequency on the axis. This variation depends on the frequency of the pulse, the focus depth and aperture size. When the center frequencies of the positively and negatively manipulated pulses become different, then the diffraction patterns will differ. Different diffraction patterns will produce observed frequency shifts other than that generated by nonlinear propagation, giving a deviance between the estimated and predicted center frequency shifts.

For Setup 2 the agreement between the estimated and predicted center frequency

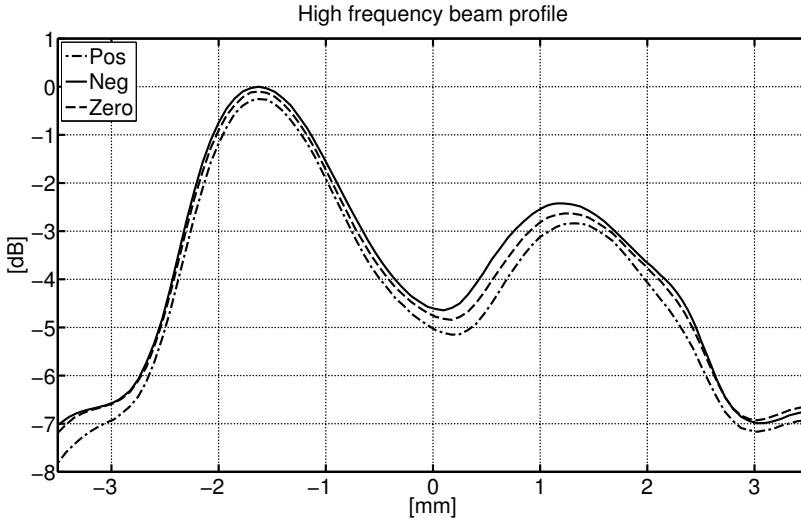


Figure C.16: Beam profile in $z = 20$ mm, of the imaging pulse for Setup 3.

shift seen in the lower panel of Figure C.9, is poor. This is, as for the nonlinear delay, due to the predicted center frequency shift being based on the pressure gradient seen on the axis, while the pressure gradient actually varies across the beam, producing a varying center frequency shift over the beam. The gradient increases off the axis so the predicted value based on the experienced gradient pressure on the axis will underestimate the center frequency shift. Another factor is the nonlinear aberration which shifts the focus. When the focus for the positively and negatively manipulated pulses is altered, so is the diffraction patterns. This can be seen quite clearly in the upper panel of Figure C.9; the peaks and troughs of the center frequency depth variations are not aligned for the positively and negatively manipulated pulses. From Figure C.12 it is also clearly seen that the axis profiles are shifted in depth relative to each other. It is also seen that the diffraction starts becoming significant at around 12 mm.

From the curves in the lower panel of Figure C.10 there is a poor agreement between the estimated and predicted center frequency shifts. The estimated center frequency shift has a break at 6 mm, and since the predicted values are accumulated based on the center frequency at the first depth, this jump introduces a difference between the estimated and predicted values. Except from the jump at 6 mm, the curves exhibit the same trend until 12 mm. But from 12 mm and on the estimated and predicted values deviates. This can again be explained by a difference in diffraction patterns due to shifts in center frequencies. From the upper panel of Figure C.10 it can be seen that the peaks in the center frequency estimates are shifted in depth relative to each other, which indicates a difference in diffraction.

The HF axis profiles of Setup 1 are shown in Figure C.11. The shape of the

profiles are close to equal except for an amplitude difference. The amplitude difference between the positively and negatively manipulated pulse has its maximum at around 16 mm, where it is ~ 0.4 dB. This difference in amplitude can also be explained by diffraction. When the center frequency increases, the beam gets narrower and the maximum amplitude on the axis increases. The positively manipulated pulse increases in frequency and so does the pressure on the axis. This is consistent with the estimated -6dB beam widths given in Table C.2, where it can be seen that the beam width for the positively manipulated pulse is 0.03 mm narrower than that of the negatively manipulated beam.

Also note that the axis profiles has two local maximums. This is due to the fact that the azimuth and elevation focus depth are different. The azimuth focusing gives a maximum at around 16 mm while the elevation focus gives a peak at 25 mm. The amplitude difference at the second peak is less than at the first. This is since the F-number for the azimuth aperture is larger, which gives a weaker focused beam and thus makes the diffraction effects less.

For Setup 2 the the nonlinear aberration produces a shift in focus depth as can be as seen in Figure C.12. For the positively manipulated beam, the manipulation pressure decreases from the center of the beam to the edges, focusing the beam further outwards. For the negatively manipulated pulse the edges of the wave experience a higher manipulation pressure, thus focusing the beam closer to the transducer. By focusing closer, the F-number will decrease, producing a narrower beam of higher amplitude. But on the contrary it is the positively manipulated beam which is narrower and of greater amplitude. This might be due to the fact that the positively manipulated pulse has a higher center frequency and since higher frequency produces a narrower beam of higher amplitude, the effect of the center frequency shift on amplitude and beam width is more dominating than the nonlinear aberration. From Table C.2 the negatively manipulated beam is 0.079 mm wider than the positively manipulated one. But keep in mind that the two beams are not focused at the same depth due to the nonlinear aberration, meaning that the beam profiles are recorded before and after their respective effective focus depths. The beam width at the effective focal depths of the two beams will be different.

This being a prototype probe there are some dead elements and other inhomogeneities in the HF array. It is therefore difficult to make a proper plane wave. From Figure C.16 it is seen that the edges of the beam has a different amplitude and that the profile is not symmetric. The positive beam is narrower, which is consistent with the higher frequency of the positively manipulated pulse than the negatively manipulated. From the beam profile of Figure C.13 it is seen that the negatively manipulated pulse has a higher amplitude than the positively manipulated which is because the center frequency of the negatively manipulated is lower, the near field limit becomes closer to the transducer and the natural diffraction occurs earlier. It is seen that the axis profile of the positively manipulated beam is shifted outwards compared to the negatively manipulated one which indicates differences in diffraction. The depth of which diffraction becomes significant decreases with decreasing center frequency for constant aperture and focus.

Diffraction poses a challenge when dealing with dual-frequency beamforming. One

of the intentions of transmitting an unfocused LF wave is to keep the phase relation constant and by placing the HF at the peak of the LF pulse minimize the pulse distortion. With limited aperture, keeping the phase relation constant, is not feasible due to diffraction of the LF wave. This produces a sliding of the HF along the LF pulse which gives an experienced pressure gradient for the HF pulse.

Even if it is not possible to achieve a constant phase relationship, the unfocused LF case is interesting since it gives less variation in the experienced LF pressure over the imaging region. For applications where it is of interest to have an even as possible experienced LF pressure, using an unfocused LF is suitable. Using an unfocused LF wave together with a focused HF will give nonlinear aberration which produces more nonlinear propagation effects.

To avoid nonlinear aberration and keep the experienced pressure as even as possible, an unfocused LF beam together with an unfocused HF can be utilized. This will give poor focusing on transmit and thus poor lateral resolution, but this can be compensated for using dynamic focusing on receive and spatial compounding [26].

Using a setting where both beams are focused will give a varying experienced pressure with depth, as the HF slides along the LF. If a high experienced pressure is desired in short depth range around the focus, this setting can be of interest. Since the LF is focused, a low transmitted pressure can be used to achieve a high pressure in the focus. Since the LF pressure will be low close to the transducer, the gradient will too, even if the HF is propagating on the maximum gradient of the LF.

C.6 Conclusion

In this paper three different beamforming strategies for dual-frequency band imaging using a large separation of center frequencies for the two bands are investigated. The nonlinear propagation delay and the center frequency shifts were estimated from the recorded pulses and predicted based on the estimated experienced LF pressure and pressure gradient.

The assumption that the nonlinear propagation effects could be limited to a nonlinear delay and frequency shift might not be valid. It is shown that the delay and frequency shift can be predicted to some extent by the experienced pressure and experienced pressure gradient. But as the frequency of the positively and negatively manipulated pulses becomes different, the diffraction of the two beams changes, yielding a deviance between the observed and predicted value. Difference in diffraction will also produce pulse form differences other than the nonlinear propagation effects.

In the case of nonlinear aberration, predicting the nonlinear propagation effect based on the experienced pressure and pressure gradient on the axis is difficult since the phase relation and thus manipulation varies across the HF beam.

What beamforming strategy is the optimal one is dependent on the application and care should be taken in designing the transmit beams. To achieve a high level of suppression of linear scattering the pulse form distortion and diffraction in addition to the nonlinear delay must be corrected for. Correcting for the nonlinear delay has been shown to be sufficient in pulse echo measurements [20], but correcting for the

distortion in pulse echo measurements should be investigated as these effects will limit the suppression of linear scattering.

The nonlinearity parameter β_n is connected to the nonlinear propagation delay and frequency shift through the experienced pressure and gradient pressure respectively. By knowledge of the experienced LF pressure and gradient, the linear wave velocity and the density of the material, estimates of the nonlinear propagation delay and center frequency shift can be used to derive the nonlinearity parameter. From the results presented here, using either Setup 1 or 3 could allow such estimation, but correction for diffraction should be performed to improve results further.

References

- [1] T. Muir and E. Carstensen, "Prediction of nonlinear acoustic effects at biomedical frequencies and intensities," *Ultrasound in Medicine & Biology*, vol. 6, no. 4, pp. 345–357, 1980.
- [2] E. Carstensen, W. Law, N. McKay, and T. Muir, "Demonstration of nonlinear acoustical effects at biomedical frequencies and intensities," *Ultrasound in Medicine & Biology*, vol. 6, no. 4, pp. 359–368, 1980.
- [3] M. Averkiou and D. Roundhill, "A new imaging technique based on the nonlinear properties of tissues," in *Ultrasonics Symposium, 1997. Proceedings., 1997 IEEE*, vol. 2, pp. 1561–1566 vol.2, 1997.
- [4] B. Haider and R. Chiao, "Higher order nonlinear ultrasonic imaging," in *Ultrasonics Symposium, 1999. Proceedings. 1999 IEEE*, vol. 2, pp. 1527–1531 vol.2, 1999.
- [5] K. Caidahl, E. Kazzam, J. Lidberg, G. Neumann-Andersen, J. Nordanstig, S. R. Dahlqvist, A. Waldenstrom, and R. Wikh, "New concept in echocardiography: harmonic imaging of tissue without use of contrast agent," *The Lancet*, vol. 352, pp. 1264–1270, Oct. 1998.
- [6] D. Simpson and P. Burns, "Pulse inversion doppler: a new method for detecting nonlinear echoes from microbubble contrast agents," in *Ultrasonics Symposium, 1997. Proceedings., 1997 IEEE*, vol. 2, pp. 1597–1600 vol.2, 1997.
- [7] C. Shen and P. Li, "Pulse-inversion-based fundamental imaging for contrast detection," *Ultrasonics, Ferroelectrics and Frequency Control, IEEE Transactions on*, vol. 50, no. 9, pp. 1124–1133, 2003.
- [8] R. J. Eckersley, C. T. Chin, and P. N. Burns, "Optimising phase and amplitude modulation schemes for imaging microbubble contrast agents at low acoustic power," *Ultrasound in Medicine & Biology*, vol. 31, pp. 213–219, Feb. 2005. PMID: 15708461.
- [9] S. Nasholm, R. Hansen, S.-E. Måsøy, T. Johansen, and B. Angelsen, "Transmit beams adapted to reverberation noise suppression using dual-frequency SURF

- imaging,” *Ultrasonics, Ferroelectrics and Frequency Control, IEEE Transactions on*, vol. 56, no. 10, pp. 2124–2133, 2009.
- [10] R. Hansen, S. Masoy, T. F. Johansen, and B. A. Angelsen, “Utilizing dual frequency band transmit pulse complexes in medical ultrasound imaging,” *The Journal of the Acoustical Society of America*, vol. 127, pp. 579–587, Jan. 2010.
- [11] S. Chiou, F. Forsberg, T. B. Fox, and L. Needleman, “Comparing differential tissue harmonic imaging with tissue harmonic and fundamental gray scale imaging of the liver,” *Journal of Ultrasound in Medicine: Official Journal of the American Institute of Ultrasound in Medicine*, vol. 26, pp. 1557–1563, Nov. 2007. PMID: 17957050.
- [12] M. Fatemi and J. F. Greenleaf, “Vibro-acoustography: An imaging modality based on ultrasound-stimulated acoustic emission,” *Proceedings of the National Academy of Sciences of the United States of America*, vol. 96, pp. 6603–6608, June 1999.
- [13] C. Cain, “Ultrasonic reflection mode imaging of the nonlinear parameter B/A: a theoretical basis,” in *IEEE 1985 Ultrasonics Symposium*, pp. 887–890, 1985.
- [14] H. Fukukita, “Ultrasound pulse reflection mode measurement of nonlinearity parameter B/A and attenuation coefficient,” *The Journal of the Acoustical Society of America*, vol. 99, no. 5, p. 2775, 1996.
- [15] C. X. Deng, F. L. Lizzi, A. Kalisz, A. Rosado, R. H. Silverman, and D. J. Coleman, “Study of ultrasonic contrast agents using a dual-frequency band technique,” *Ultrasound in Medicine & Biology*, vol. 26, no. 5, pp. 819 – 831, 2000.
- [16] A. Bouakaz, M. Versluis, J. Borsboom, and N. de Jong, “Radial modulation of microbubbles for ultrasound contrast imaging,” *Ultrasonics, Ferroelectrics and Frequency Control, IEEE Transactions on*, vol. 54, no. 11, pp. 2283–2290, 2007.
- [17] J. C. Buckey, D. A. Knaus, D. L. Alvarenga, M. A. Kenton, and P. J. Magari, “Dual-frequency ultrasound for detecting and sizing bubbles,” *Acta Astronautica*, vol. 56, no. 9-12, pp. 1041–1047, 2005.
- [18] R. Hansen and B. Angelsen, “SURF imaging for contrast agent detection,” *Ultrasonics, Ferroelectrics and Frequency Control, IEEE Transactions on*, vol. 56, no. 2, pp. 280–290, 2009.
- [19] M. Fatemi, L. E. Wold, A. Alizad, and J. F. Greenleaf, “Vibro-acoustic tissue mammography,” *IEEE Transactions on Medical Imaging*, vol. 21, pp. 1–8, Jan. 2002. PMID: 11838661.
- [20] S. Måsøy, O. Standal, P. Nasholm, T. Johansen, B. Angelsen, and R. Hansen, “SURF imaging: In vivo demonstration of an ultrasound contrast agent detection technique,” *Ultrasonics, Ferroelectrics and Frequency Control, IEEE Transactions on*, vol. 55, no. 5, pp. 1112–1121, 2008.

- [21] B. Angelsen, *Ultrasound imaging. Waves, signals and signal processing Vol I*. Trondheim: Emantec, 2000.
- [22] B. Angelsen, *Ultrasound imaging. Waves, signals and signal processing Vol II*. Trondheim: Emantec, 2000.
- [23] B. Angelsen and R. Hansen, “7A-1 SURF imaging - a new method for ultrasound contrast agent imaging,” in *Ultrasonics Symposium, 2007. IEEE*, pp. 531–541, 2007.
- [24] F. A. Duck, *Physical Properties of Tissues: A Comprehensive Reference Network*. Elsevier Science & Technology Books, Feb. 1990.
- [25] T. Johansen, J. Deibele, S. Måsøy, R. Hansen, and B. Angelsen, “Design and test of a Dual-Layer, Dual-Frequency SURF array,” *Proceedings of the 31st Scandinavian Symposium on Physical Acoustics*, vol. 31, 2001.
- [26] G. Montaldo, M. Tanter, J. Bercoff, N. Benech, and M. Fink, “Coherent plane-wave compounding for very high frame rate ultrasonography and transient elastography,” *Ultrasonics, Ferroelectrics and Frequency Control, IEEE Transactions on*, vol. 56, no. 3, pp. 489–506, 2009.

Imaging of Nonlinear Scattering using Dual-frequency Band Ultrasound

Thor Andreas Tangen² and Bjørn Angelsen¹

¹Department of Circulation and Medical Imaging, NTNU, Trondheim, Norway,

²Department of Engineering Cybernetics, NTNU, Trondheim, Norway

D.1 Introduction

Scattering particles which exhibit a nonlinear response to applied pressure are said to be nonlinear scatterers. Such scattering particles are either highly compressible or incompressible. An example of a highly compressible particle is a gas bubble, while a highly incompressible particle can be a micro calcification particle which is an important feature in the diagnosis of breast cancer [1].

In current practice nonlinear scattering phenomena is utilized in order to detect scattering from ultrasound contrast agents. The contrast agents are gas filled microbubbles and has a strong resonant behavior. The resonance frequency of the bubbles lies in the range 2 to 4 MHz [2] and when insonified at such frequencies the bubbles generate a backscattered signal which contains harmonics of the insonifying frequency. By suppression the linear scattered signal from tissue either by temporal filtering or using doppler techniques like pulse inversion or amplitude modulation, the nonlinear scattered signal from the bubbles can be detected [2, 3].

In the nonlinear regime, fluctuations in nonlinearity parameter as well as in the compressibility produces scattering of the ultrasound wave. Stiff particles embedded in soft tissue will exhibit a stronger nonlinear scattering than that of the surrounding tissue. Using the nonlinear wave equation presented in [4], the scattered wave is the quadratic of the incident pressure. In conventional single-band frequency imaging, nonlinear propagation generates accumulative harmonic self distortion of the forward propagating wave. The nonlinear scattering is generated by the same process as nonlinear propagation, but they differ in the way that the propagation is an accumulative effect while the scattering is local. In single-frequency band imaging, the nonlinear scattered signal has the same signature as the nonlinear propagation and can thus not be detected.

In dual-frequency band imaging, pulses consisting of a low-frequency (LF) manipulation pulse and a high-frequency imaging pulse is utilized [5]. The two pulses overlaps in time and the LF pulse is used to manipulate the propagation and scattering of the HF pulse. The nonlinear interaction between the two frequency bands will generate signal components at the sum and difference frequencies of the LF and HF, and the polarity of these signal components will be dependent on the polarity of the LF manipulation pulse. The forward propagation will generate these signal components accumulatively with depth, nonlinear scattering will generate the locally. By

transmitting two such dual-frequency band pulse complexes in each beam direction where the polarity of the LF pulse is inverted for the second pulse complex, the local nonlinear scattering can be detected. In order to detect the nonlinear scattering the nonlinear propagation must be estimated and corrected for.

The full nonlinear wave equation is presented in Section D.2.1. The nonlinear propagation and scattering is elaborated on in Section D.2.2 and D.2.3 respectively. In Section D.3 the effect of the HF-bandwidth/LF-frequency relationship on the ability to separate the nonlinear scattering from the nonlinear propagation is investigated. A method for estimating the nonlinear propagation is presented in Section D.2.5 together with a performance measure for this method. In order to suppress the linear scattering and detect the nonlinear scattering, a certain level of accuracy of the estimated nonlinear propagation is needed. This accuracy is dependent on certain properties of the transmit and receive wave fields. In Section D.4 the effect of beamforming parameters on the accuracy of the estimated nonlinear propagation is investigated using simulations.

D.2 Theory

D.2.1 Nonlinear wave equation

The nonlinear wave equation can be modeled as [6]

$$\underbrace{\nabla^2 p(\underline{r}, t) - \frac{1}{c_0^2(\underline{r})} \frac{\partial^2 p(\underline{r}, t)}{\partial t^2} + \frac{\beta_{na} \kappa_a}{c_0^2(\underline{r})} \frac{\partial^2 p^2(\underline{r}, t)}{\partial t^2}}_{\text{Nonlinear propagation}} - \underbrace{h_p \otimes_t \frac{1}{c_0^2(\underline{r})} \frac{\partial^2 p(\underline{r}, t)}{\partial t^2}}_{\text{Absorption}} = \underbrace{\frac{\sigma_l(\underline{r})}{c_0^2(\underline{r})} \frac{\partial^2 p(\underline{r}, t)}{\partial t^2} + \nabla(\gamma(\underline{r})) \nabla p(\underline{r}, t)}_{\text{Linear scattering}} - \underbrace{\frac{\sigma_n(\underline{r})}{2c_0^2(\underline{r})} \frac{\partial^2 p^2(\underline{r}, t)}{\partial t^2}}_{\text{Nonlinear scattering}} \quad (\text{D.1})$$

where $p(\underline{r}, t)$ is the pressure pulse at spatial position \underline{r} , $c_0^2(\underline{r}) = \frac{1}{\rho_a(\underline{r})\kappa_a(\underline{r})}$ is the linear propagation velocity, κ is the bulk compressibility, ρ is the mass density, β_n is the nonlinearity parameter and h_p is frequency dependent attenuation. The spatial variation of the material parameters can be modeled as an average, a , and fluctuating, f , component, where the average is taken over a few wavelengths.

$$\begin{aligned}
 \kappa(\underline{r}) &= \kappa_a + \kappa_f(\underline{r}) \\
 \rho(\underline{r}) &= \rho_a + \rho_f(\underline{r}) \\
 \beta(\underline{r}) &= \beta_{na} + \beta_{nf}(\underline{r}) .
 \end{aligned} \quad (\text{D.2})$$

The scattering coefficients are then given as

$$\begin{aligned}\sigma_l(\underline{r}) &= \frac{\kappa_f(\underline{r})}{\kappa_a(\underline{r})} \\ \gamma(\underline{r}) &= \frac{\rho_f(\underline{r})}{\rho(\underline{r})} \\ \sigma_n(\underline{r}) &= \{2\beta_{na}(2 + \sigma_l)\sigma_l + \beta_{nf}(1 + \sigma_l)^2\} \kappa_a.\end{aligned}\tag{D.3}$$

D.2.2 Nonlinear propagation

Introducing retarded time, $\tau = t - \frac{z}{c_0}$, in Equation (D.1) and neglecting the scattering terms, the nonlinear wave equation for propagation can be written as

$$\frac{\partial^2 p(\underline{r}, \tau)}{\partial z \partial \tau} = \frac{c_0(\underline{r})}{2} \nabla_{\perp}^2 p(\underline{r}, \tau) - h_p \otimes_t \frac{1}{c_0(\underline{r})} \frac{\partial^2 p(\underline{r}, \tau)}{\partial \tau^2} + \frac{\beta_{na} \kappa_a}{c_0(\underline{r})} \frac{\partial^2 p^2(\underline{r}, \tau)}{\partial \tau^2}.\tag{D.4}$$

Taking the Fourier transform in time of Equation (D.4) gives

$$\begin{aligned}\frac{\partial p(\underline{r}, \omega)}{\partial z} &= -i \frac{c_0(\underline{r})}{2\omega} \nabla_{\perp}^2 p(\underline{r}, \omega) - i \frac{\omega}{c_0(\underline{r})} H(\underline{r}, \omega) p(\underline{r}, \omega) \\ &\quad - i\omega \frac{\beta_{na} \kappa_a}{2c_0(\underline{r})} p(\underline{r}, \omega) \otimes_{\omega} p(\underline{r}, \omega).\end{aligned}\tag{D.5}$$

This is an integral equation, which can be solved numerically in different ways [7, 8]. One such solution is to use an iterative procedure like

$$\begin{aligned}p(r_{\perp}, z_{k+1}, \omega) &= p(r_{\perp}, z_k, \omega) \exp \left\{ -i \frac{c_0(\underline{r})}{2\omega} \int_{z_k}^{z_{k+1}} ds \frac{\nabla_{\perp}^2 p(r_{\perp}, s, \omega)}{p(r_{\perp}, s, \omega)} \right\} \\ &\quad \times \exp \left\{ -i \frac{\omega}{2c_0(\underline{r})} \int_{z_k}^{z_{k+1}} ds H(r_{\perp}, s, \omega) \right\} \\ &\quad \times \exp \left\{ -i\omega \frac{\beta_{na} \kappa_a}{2c_0(\underline{r})} \int_{z_k}^{z_{k+1}} ds \frac{p(r_{\perp}, s, \omega) \otimes_{\omega} p(r_{\perp}, s, \omega)}{p(r_{\perp}, s, \omega)} \right\}.\end{aligned}\tag{D.6}$$

This way of solving the nonlinear propagation shows very explicitly how the different terms in Equation (D.5) contributes to the propagation.

The quadratic term on the right hand side of Equation (D.4), which corresponds to the convolution term in Equation (D.5), represents the nonlinear propagation. This term is of specific interest for dual-frequency band imaging as it expresses the interaction between two frequency bands. The dual-frequency band pressure pulse is composed of a LF pulse and a HF pulse

$$p(\underline{r}, t) = p_L(\underline{r}, t) + p_H(\underline{r}, t).\tag{D.7}$$

Inserting the dual-band pressure pulse into the quadratic term of Equation (D.4) gives

$$\frac{\partial^2 p^2(\underline{r}, t)}{\partial t^2} = \frac{\partial^2}{\partial t^2} (p_L^2(\underline{r}, t) + p_L(\underline{r}, t) p_H(\underline{r}, t) + p_H^2(\underline{r}, t)),\tag{D.8}$$

were the first and third terms expresses nonlinear self distortion, *i.e.* harmonic distortion, of the LF and HF pulse respectively, and the second term expresses the interaction of the two frequency bands. Assuming that the low frequency pulse is a pure cosine over the HF pulse length, *i.e.*

$$p_L(\underline{r}, t) = p_{L0}(\underline{r}) \cos(\omega_L(t + \tau_L(\underline{r}))) \quad (\text{D.9})$$

where $\tau_L(\underline{r})$ is the position of the HF relative to the LF. If $\tau_L(\underline{r}) = 0$, the HF is centered at the peak of the LF oscillation. Taking the Fourier transform of the interaction term in Equation (D.8) gives

$$\begin{aligned} \text{F} \left\{ \frac{\partial^2 p_L(\underline{r}, t) p_H(\underline{r}, t)}{\partial t^2} \right\} &= p_{L0}(\underline{r}) \int d\tau e^{-i\omega\tau} \frac{\partial^2}{\partial \tau^2} \{ \cos(\omega_L(\tau + \tau_L(\underline{r}))) p_H(\underline{r}, \tau) \} \\ &= \frac{p_{L0}(\underline{r})}{2} \left[\int d\tau e^{-i\omega\tau} \frac{\partial^2}{\partial \tau^2} \left\{ e^{i\omega_L(\tau + \tau_L(\underline{r}))} p_H(\underline{r}, \tau) \right\} \right. \\ &\quad \left. + \int d\tau e^{-i\omega_L(\tau + \tau_L(\underline{r}))} \frac{\partial^2}{\partial \tau^2} \left\{ e^{-i\omega_L(\tau + \tau_L(\underline{r}))} p_H(\underline{r}, \tau) \right\} \right] \\ &= \frac{\omega^2 p_{L0}(\underline{r})}{2} \left[e^{i\omega_L \tau_L(\underline{r})} p_H(\underline{r}; \omega - \omega_L) + e^{-i\omega_L \tau_L(\underline{r})} p_H(\underline{r}; \omega + \omega_L) \right]. \end{aligned} \quad (\text{D.10})$$

From this it is seen that the nonlinear propagation generates signals components at the sum and difference frequencies of the HF and LF, in addition to harmonics of the HF and LF bands. The generation of signal components in the sum and difference bands is an accumulative process and is dependent on the material parameters and the manipulation pressure. The expression in Equation (D.10) can be analyzed further by expansion of the exponential terms

$$\begin{aligned} \text{F} \left\{ \frac{\partial^2 p_L(\underline{r}, t) p_H(\underline{r}, t)}{\partial t^2} \right\} &= \omega^2 p_{L0}(\underline{r}) \cos(\omega_L \tau_L(\underline{r})) p_H(\underline{r}; \omega) \\ &\quad + \frac{1}{2} \omega^2 p_{L0}(\underline{r}) \cos(\omega_L \tau_L(\underline{r})) [p_H(\underline{r}; \omega - \omega_L) + p_H(\underline{r}; \omega + \omega_L) - 2p_H(\underline{r}; \omega)] \\ &\quad + \frac{1}{2} i \omega^2 p_{L0}(\underline{r}) \sin(\omega_L \tau_L(\underline{r})) [p_H(\underline{r}; \omega - \omega_L) - p_H(\underline{r}; \omega + \omega_L)]. \end{aligned} \quad (\text{D.11})$$

Considering the exponent of the last exponential term in Equation (D.6), where the convolution term corresponds to the quadratic term and inserting the expression of

the interaction term from Equation (D.11) gives

$$\begin{aligned}
 -i\alpha(\omega) \int_{z_k}^{z_{k+1}} ds \frac{p(s, r_\perp, \omega) \otimes p(s, r_\perp, \omega)}{p(s, r_\perp, \omega)} = & \\
 i\alpha(\omega) \int_{z_k}^{z_{k+1}} ds \left\{ p_{L0}(\underline{r}) \cos(\omega_L \tau_L(\underline{r})) \frac{p_H(\underline{r}; \omega)}{p(\underline{r}, \omega)} \right\} & \\
 +i\alpha(\omega) \int_{z_k}^{z_{k+1}} ds \left\{ \frac{1}{2} p_{L0}(\underline{r}) \cos(\omega_L \tau_L(\underline{r})) \right. & \\
 \times \left. \frac{[p_H(\underline{r}; \omega - \omega_L) + p_H(\underline{r}; \omega + \omega_L) - 2p_H(\underline{r}; \omega)]}{p(\underline{r}, \omega)} \right\} & \quad (\text{D.12}) \\
 +i\alpha(\omega) \int_{z_k}^{z_{k+1}} ds \left\{ \frac{1}{2} p_{L0}(\underline{r}) \sin(\omega_L \tau_L(\underline{r})) \right. & \\
 \times \left. \frac{[p_H(\underline{r}; \omega - \omega_L) - p_H(\underline{r}; \omega + \omega_L)]}{p(\underline{r}, \omega)} \right\} + \dots &
 \end{aligned}$$

where $\alpha(\omega) = \frac{\beta_{na}\kappa_a}{2c_0(\underline{r})}\omega$, $p(\underline{r}, \omega) = p_L(\underline{r}, \omega) + p_H(\underline{r}, \omega)$, the self distortion terms has been omitted for notational convenience and the spatial position is combined in $\underline{r} = (s, r_\perp)$. The fraction in the first integral on the right hand side will be 1 over the HF band which means that the first term will produce an accumulative linear phase component over the HF band, *i.e.* introduce a nonlinear propagation delay compared to a non-manipulated HF pulse. The delay can be observed in the time domain as the delay of the part of the HF which is used as the reference point for τ_L . The second term will produce an accumulative broadening of the HF spectrum, while the third term will shift the HF band up or down in frequency depending on the polarity of the spatial gradient of the LF over the HF pulse. If the spatial gradient of the LF manipulation pressure over the HF pulse is positive, there will be a decrease in center frequency of the HF pulse and a increase if it is on a negative gradient.

Depending on the phase relation between the HF and LF pulse, the relative contribution of the different terms in Equation (D.11) will vary. For the special case when the HF pulse is centered at the peak or trough of the LF manipulation pulse, *i.e.* $\tau_L(\underline{r}) = 0$, the sine term is zero and there is a accumulative broadening of the HF spectrum in addition to a nonlinear propagation delay. If on the other hand the HF pulse is centered at the zero crossing of the LF manipulation pulse, there will be a shift in frequency [5].

D.2.3 Nonlinear scattering

Scattering of ultrasound waves is due to spatial fluctuation of the material parameters, where linear scattering is due to fluctuations in the density ρ as well as the compressibility κ , while nonlinear scattering is due to fluctuations in the nonlinear parameter β_n in addition to the compressibility. For soft tissue internally, the local fluctuations of the nonlinearity parameter is small, but for a stiff particle like *e.g.* a micro calcification particle embedded in soft tissue the local fluctuation can be significant.

Material	β_n	κ [Pa 10^{-12}]
Muscle	4.7	400
Fat	5.8	508
Micro calcification	0	0.85

Table D.1: Material parameters [6, 9]

As an example, consider ultrasound scattering from a muscle/fat (*mf*) interface and a micro calcification particle embedded in muscle tissue (*mc*). The material parameters are listed in Table D.1. For both cases the average nonlinearity and compressibility can be set to that of muscle, *i.e.* $\beta_{na} = 4.7$, $\kappa_a = 400 \times 10^{-12}$. The fluctuation in the nonlinearity parameter is then $\beta_{nf} = 1.1$ and $\beta_{nf} = -5$ for the muscle/fat and muscle/calcification interface respectively, while the linear scattering coefficient, σ_l , is 0.1 [6] and 0.87 [9, 10] respectively. The amplitude of the nonlinear scattering relative to the linear scattering is given as

$$\frac{\sigma_n}{\sigma_l - \gamma} p_L = \frac{2\beta_{na} (2 + \sigma_l) \sigma_l + \beta_{nf} (1 + \sigma_l)^2}{1.3\sigma_l} \kappa_a p_L \quad (\text{D.13})$$

where p_L is the LF manipulation pressure and the approximation $\sigma_l - \gamma \approx 1.3\sigma_l$ [6] has been employed. Using a LF manipulation pressure of 1 MPa, the ratio of nonlinear to linear scattering for the two cases are

$$\begin{aligned} mf : \quad & \frac{\sigma_n}{1.3\sigma_l} = 14.2 \times 10^{-3} \sim -36\text{dB} \\ mc : \quad & \frac{\sigma_n}{1.3\sigma_l} = 3.4 \times 10^{-3} \sim -49\text{dB}, \end{aligned}$$

while the relative amplitude of the nonlinear scattering from the micro calcification to the linear scattering from the muscle/fat interface is $\sim -30\text{dB}$ and the nonlinear scattering from the micro calcification is $\sim 6\text{dB}$ stronger than that of the muscle/fat interface. Thus in order to detect the nonlinear scattering from the micro calcification, the linear scattering from tissue must be suppressed more than 30 dB.

From the nonlinear wave equation (D.1) it is seen that the nonlinear scattering term also is quadratic in the pressure. This means that the nonlinear propagation and scattering are equal processes, but they differ in the way that the nonlinear propagation is a cumulative process while the nonlinear scattering is a local effect.

From the discussion of nonlinear propagation in Section D.2.2, the nonlinear generated signal components from the interaction of the two frequency bands will be dependent on the sign of the polarity of the LF manipulation pulse. By transmitting two dual-frequency band complexes along the same beam direction and flipping the polarity of the LF pulse for the second complex, the generated sum and difference bands will have a phase shift in the frequency domain of π from the first to the second pulse complex. The two pulse complexes will be denoted the positively and negatively manipulated pulse respectively, referring to the polarity of the LF manipulation pulse.

If the bandwidth of the HF pulse is less than the center frequency of the LF band, *i.e.* the frequency bands at the sum and difference frequencies will not overlap with the fundamental band, the cumulative propagation effect transfers energy from the fundamental band into the sum and difference bands without distorting the fundamental band. In this case the nonlinear propagation and scattering generates signals with equal signature, which makes the two effects inseparable.

If the bandwidth of the HF is increased to above the center frequency of the LF band, the sum and difference bands will mix with the fundamental band. For the forward propagated pulses, the phase of the fundamental and sum/difference bands will mix in the overlap regions, and the phase difference between the positively and negatively manipulated pulse in these overlapping bands will be different from π . But for the nonlinear scattering, which is a local effect, the nonlinear scattered signal will have a phase shift of π from the positive to the negative manipulated pulse for the sum and difference bands. By finding the appropriate correction which compensates for the nonlinear propagation, the nonlinear scattering can be separated from the linear scattered signal.

In the limiting case where the HF pulse becomes so short compared to the LF period that the LF pressure can be approximated as a hydrostatic pressure, the nonlinear propagation will be limited to a nonlinear propagation delay and the nonlinear scattering will have the same form as the fundamental signal with the polarity following the LF pulse polarity.

D.2.4 Received Signal Model

The forward propagated wave field at the spatial location (r_{\perp}, z) for the positive and negative manipulated pulses are denoted

$$U_{t+/-}(\omega; r_{\perp}, z), \quad (\text{D.14})$$

where the subscript t , denotes the transmitted field, while the subscript r in the following derivations will denote the received wave field. The received signal can then be modeled as

$$\begin{aligned} Y_{+/-}(\omega) &= \int_V dr_{\perp} dz U_{r,+/-}(r_{\perp}, z, \omega) \sigma(r_{\perp}, z) \\ U_{r,+/-}(r_{\perp}, z, \omega) &= -\omega^2 H_r(\omega; r_{\perp}, z) U_{t+/-}(\omega; r_{\perp}, z), \end{aligned} \quad (\text{D.15})$$

where H_r is the receive spatial frequency response and σ are the scatterers. In some parts of the following analysis it is convenient to consider scatterers in a plane at depth z . The received signal will then be modeled as

$$\begin{aligned} Y_{+/-}(\omega; z) &= \int_R dr_{\perp} U_{r,+/-}(\omega; r_{\perp}, z) \sigma(r_{\perp}, z) \\ U_{r,+/-}(\omega; r_{\perp}, z) &= -\omega^2 H_r(\omega; r_{\perp}, z) U_{t+/-}(\omega; r_{\perp}, z). \end{aligned} \quad (\text{D.16})$$

D.2.5 Correction of nonlinear propagation

In order to detect nonlinear scattering, the nonlinear propagation must be corrected for. Let the received signal from the interval $[-T, T]$ centered around $t_n = \frac{2z_n}{c_0}$ be

$$\begin{aligned} Z_{+,n}(\omega) &= Y_{+,n}(\omega) + N_{+,n}(\omega) \\ Z_{-,n}(\omega) &= Y_{-,n}(\omega) + N_{-,n}(\omega), \end{aligned} \quad (\text{D.17})$$

where $N_{+/-}(\omega)$ is additive white noise.

The nonlinear propagation effects can be corrected for by applying a filter, denoted $G(\omega)$, which makes the linear scattered signal from the negatively manipulated pulse equal to that of the positively manipulated pulse. Taking the signal over the specified interval from one scan line, then there exists a filter which makes the two signals equal. Such a filter can be

$$\hat{G}_{1n} = \frac{Z_{+,n}(\omega)}{Z_{-,n}(\omega)}. \quad (\text{D.18})$$

Note that this filter will not only suppress the linear scattered signal but also the local nonlinear scattered signal. The two signals will become identical, *i.e.* subtraction of the two signals will give zero. By assuming that there are few strong nonlinear scatterers in the image, which can be true for micro calcifications, one can find the filter which minimizes the difference between the received signal from the positive and negative manipulated pulses over a region in the image in a minimum least squares fashion. In this sense the sparse nonlinear scattering is to be considered as a special type of noise. The optimal filter in the minimum mean squares sense is the filter $G_n(\omega)$ which minimizes

$$\begin{aligned} J &= \left\langle |Z_{+,n}(\omega) - G_n(\omega) Z_{-,n}(\omega)|^2 \right\rangle \\ &= \left\langle [Z_{+,n}(\omega) - G_n(\omega) Z_{-,n}(\omega)] [Z_{+,n}(\omega) - G_n(\omega) Z_{-,n}(\omega)]^* \right\rangle \end{aligned} \quad (\text{D.19})$$

where $\langle \cdot \rangle$ denotes statistical averaging over an ensemble of measurements. The filter which minimizes this functional is given as

$$\hat{G}_n(\omega) = \frac{\langle Z_{+,n}(\omega) Z_{-,n}^*(\omega) \rangle}{\langle |Z_{-,n}(\omega)|^2 \rangle} \quad (\text{D.20})$$

By assuming uncorrelated white noise the expression in Equation (D.20) can be written as

$$\begin{aligned} \hat{G}_n(\omega) &= K_-(\omega) \frac{\langle Y_{+,n}(\omega) Y_{-,n}^*(\omega) \rangle}{\langle |Y_{-,n}(\omega)|^2 \rangle} \\ K_-(\omega) &= \frac{1}{1 + \frac{\langle |N_{-,n}(\omega)|^2 \rangle}{\langle |Y_{-,n}(\omega)|^2 \rangle}} \end{aligned} \quad (\text{D.21})$$

The minimum error is found by inserting Equation (D.20) into the expression in (D.19)

$$\begin{aligned}
 J_{min} &= \langle |Z_{+,n}(\omega)|^2 \rangle - \hat{G}_n^*(\omega) \langle Z_{+,n}(\omega) Z_{-,n}^*(\omega) \rangle \\
 &\quad - \hat{G}_n(\omega) \langle Z_{+,n}^*(\omega) Z_{-,n}(\omega) \rangle - |\hat{G}_n(\omega)|^2 \langle |Z_{-,n}(\omega)|^2 \rangle \\
 &= \langle |Z_{+,n}(\omega)|^2 \rangle \left(1 - |\hat{G}_n(\omega)|^2 \frac{\langle |Z_{-,n}(\omega)|^2 \rangle}{\langle |Z_{+,n}(\omega)|^2 \rangle} \right).
 \end{aligned} \tag{D.22}$$

The relative minimum error is found by dividing the minimum error by $\langle |Z_{+,n}(\omega)|^2 \rangle$

$$\frac{J_{min}}{\langle |Z_{+,n}(\omega)|^2 \rangle} = 1 - \frac{\langle Z_{+,n}(\omega) Z_{-,n}^*(\omega) \rangle^2}{\langle |Z_{+,n}(\omega)|^2 \rangle \langle |Z_{-,n}(\omega)|^2 \rangle}. \tag{D.23}$$

By the assumption of white uncorrelated noise, this can further be expanded to

$$\begin{aligned}
 \frac{J_{min}}{\langle |Z_{+,n}(\omega)|^2 \rangle} &= 1 - K_-(\omega) K_+(\omega) \frac{\langle Y_{+,n}(\omega) Y_{-,n}^*(\omega) \rangle^2}{\langle |Y_{+,n}(\omega)|^2 \rangle \langle |Y_{-,n}(\omega)|^2 \rangle} \\
 &= 1 - K_-(\omega) K_+(\omega) |\rho_{+/-}(\omega)|^2
 \end{aligned} \tag{D.24}$$

where

$$|\rho_{+/-}(\omega)| = \frac{\langle Y_{+,n}(\omega) Y_{-,n}^*(\omega) \rangle}{\sqrt{\langle |Y_{+,n}(\omega)|^2 \rangle \langle |Y_{-,n}(\omega)|^2 \rangle}} \tag{D.25}$$

is the correlation coefficient between the received positive and negative manipulated signal over the ensemble. The factors $K_{+/-}(\omega)$ are dependent on the SNR and limits the minimum achievable error. In order to achieve the minimum error, the modulo of the correlation coefficient should be equal to 1.

The expression in Equation (D.22) can be interpreted as the maximum achievable average suppression of linear scattering over the region, using the filter estimate given in Equation (D.20). The expression in Equation (D.23) gives an indication of the required correlation over the ensemble needed to achieve a certain level of suppression. To achieve an average of X dB suppression, the correlation coefficient must be

$$|\rho_{+/-}(\omega)| = \sqrt{1 - 10^{\frac{X}{10}}}. \tag{D.26}$$

In order to achieve a suppression of -40 dB, the correlation coefficient has to be ≈ 0.99995 .

Considering scatterers in a plane at depth z and using the received signal model in Equation (D.16) the crosscorrelation and autocorrelation expressions in (D.21) be-

comes

$$\begin{aligned} \langle Y_{+,n}(\omega; z) Y_{+,n}^*(\omega; z) \rangle &= \int_R dr_\perp dr_{\perp 1} U_{r,+}(r_\perp, z; \omega) U_{r,-}^*(r_\perp, z; \omega) \langle \sigma(r_\perp, z) \sigma(r_{\perp 1}, z_1) \rangle \\ \langle |Y_{+/-,n}(\omega; z)|^2 \rangle &= \int_R dr_\perp dr_{\perp 1} |U_{r,+/-}(r_\perp, z; \omega)|^2 \langle \sigma(r_\perp, z) \sigma(r_{\perp 1}, z_1) \rangle . \end{aligned} \quad (\text{D.27})$$

Assuming δ -correlated scatterers, *i.e.*

$$\langle \sigma(r_\perp, z) \sigma(r_{\perp 1}, z_1) \rangle = \sigma^2 \delta(r_\perp - r_{\perp 1}, z - z_1) \quad (\text{D.28})$$

the correlations in Equation (D.27) becomes

$$\begin{aligned} \langle Y_{+,n}(\omega) Y_{-,n}^*(\omega) \rangle &= \int_R dz dr_\perp U_{r,+}(r_\perp, z; \omega) U_{r,-}^*(r_\perp, z; \omega) \\ \langle |Y_{+/-,n}(\omega)|^2 \rangle &= \int_R dz dr_\perp |U_{r,+/-}(r_\perp, z; \omega)|^2 . \end{aligned} \quad (\text{D.29})$$

Schwarz inequality states that [11]

$$\begin{aligned} \left| \int_R dr_\perp U_{r,+}(r_\perp, z; \omega) U_{r,-}^*(r_\perp, z; \omega) \right|^2 &\leq \\ &\int_R dr_\perp |U_{r,+}(r_\perp, z; \omega)|^2 \int_R dr_\perp |U_{r,-}(r_\perp, z; \omega)|^2 . \end{aligned} \quad (\text{D.30})$$

In order to achieve optimal suppression, *i.e.* $|\rho_{+/-}(\omega)|^2 = 1$, it can be seen from Equation (D.23) that the Schwarz inequality has to be satisfied with equality, which means that

$$U_{r,+}(r_\perp, z; \omega) = \alpha(\omega) U_{r,-}(r_\perp, z; \omega) , \quad (\text{D.31})$$

i.e. the relation between the positive and negative receive wave field must be spatially invariant.

To analyze what this result implies for the transmitted wave field, one can insert the relation between the receive and transmit field in Equation (D.16) into the correlation expressions in (D.27)

$$\begin{aligned} \langle Y_{+,n}(\omega) Y_{+,n}^*(\omega) \rangle &= \int_R dz dr_\perp |H_r(r_\perp, z; \omega)|^2 U_{t,+}(r_\perp, z; \omega) U_{t,-}^*(r_\perp, z; \omega) \\ \langle |Y_{+/-,n}(\omega)|^2 \rangle &= \int_R dz dr_\perp |H_r(r_\perp, z; \omega)|^2 |U_{r,+/-}(r_\perp, z; \omega)|^2 . \end{aligned} \quad (\text{D.32})$$

Applying Schwartz inequality and viewing the spatial frequency response of the receive beam, $|H_r(r_\perp, z; \omega)|$, as a weighting function in a scalar product gives

$$\begin{aligned} \left| \int_R dz dr_\perp |H_r(r_\perp, z; \omega)|^2 U_{t,+}(r_\perp, z; \omega) U_{t,-}^*(r_\perp, z; \omega) \right|^2 &\leq \\ &\int_R dz dr_\perp |H_r(r_\perp, z; \omega)|^2 |U_{t,+}(r_\perp, z; \omega)|^2 \\ &\times \int_R dz dr_\perp |H_r(r_\perp, z; \omega)|^2 |U_{t,-}(r_\perp, z; \omega)|^2 , \end{aligned} \quad (\text{D.33})$$

where equality is found when

$$U_{t,+}(r_{\perp}, z; \omega) = \alpha(\omega) U_{t,-}(r_{\perp}, z; \omega). \quad (\text{D.34})$$

This implies that the relation between the forward propagated positive and negative manipulated wave fields must be spatially invariant over the receive beam. The receive beam can thus be used to limit the area over which the relation in Equation (D.34) must hold. The Schwartz inequality is satisfied in particular when one can approximate

$$U_{t,+/-}(r_{\perp}, z; \omega) = U_{t,+/-}(z_n; \omega), \quad (\text{D.35})$$

i.e. the beam is homogenous over the receive scatterer volume. For scatterers in a plane at depth z , equality in can be achieved if the transmitted wave field is homogenous over the receive beam. The transmit beams must thus be designed with this in mind in order to achieve optimal suppression.

D.3 Differentiating nonlinear scattering from nonlinear propagation

D.3.1 Introduction

From the discussion in Section D.2.3 it is indicated that the ability to differentiate nonlinear scattering from the nonlinear propagation is related to the bandwidth of the HF pulse relative to the center frequency of the LF pulse. In this section a simulation study is presented where the ability to detect nonlinear scattering as a function of the absolute bandwidth of the HF relative to the center frequency of the LF pulse is investigated. Different frequency relationships between the HF and LF are investigated and for each relationship the bandwidth of the HF pulse is varied.

D.3.2 Simulations

1D simulations has been performed using Abersim [8, 12]. Four different frequency relationships between the HF and LF has been investigated, and for each relationship the bandwidth of the HF pulse has been varied. The center frequency of the LF pulse has been kept constant at 1MHz for all simulations with a -6dB bandwidth of 40%, while the HF frequencies used are 7-10 MHz at 1MHz steps. For each combination of HF frequency and LF frequency, -6dB bandwidths for the HF of [3.5, 5, 6.5, 8, 10, 13, 17, 20, 30, 40, 60, 80] % is simulated. The transmitted pressures was set to 0.5 MPa for both the LF and HF pulse.

For all simulations the HF pulse is centered at the peak or trough of the LF pulse and two simulations are performed for each combination of frequency relation and HF bandwidth where the polarity of the LF is inverted from the first to the second simulation.

Since there is no diffraction in 1D simulations the phase relationship between the HF and LF pulse will remain constant with depth. The nonlinear propagation effects

are dependent on this phase relationship, as is the nonlinear scattering. As mentioned in Section D.2.3, the nonlinear propagation and scattering are equal processes if the phase relationship during propagation and scattering is the same. In order to demonstrate the fact that these two effects are separable even if these two processes are the same, the diffraction is neglected. In the case of diffraction where the phase relationship will vary with depth, the accumulative nonlinear propagation will be different from the local nonlinear scattering effect, which complicates the analysis.

The linear and nonlinear scattered pulses are computed by taking the second derivative of the forward propagated pulse. No scaling of the scattering is performed as the absolute strength of the scattered signal is not of interest, but the relative strength between the different transmit pulse setups. The pulses were propagated until 20 mm without attenuation, and the processing was done for the pulses at the final depth.

D.3.3 Processing

All processing was done using MATLAB (The Mathworks, Massachusetts, USA). The scattered signal was computed as

$$\begin{aligned} S_{lin,+/-}(\omega) &= -\omega^2 U_{t,+/-}(\omega) \\ S_{nl,+/-}(\omega) &= -\omega^2 (U_{t,+/-}(\omega) \otimes U_{+/-}(\omega)) \end{aligned} \quad (D.36)$$

where $U_{t,+}(\omega)$ and $U_{t,-}(\omega)$ is the forward propagated pulse for the positive and negative manipulated pulse at depth $z = 20$ mm respectively. The total scattered signal was computed by adding the linear and nonlinear scattered component

$$S_{+/-}(\omega) = S_{lin+/-}(\omega) + S_{nl,+/-}(\omega). \quad (D.37)$$

The filter correcting for the nonlinear propagation effects of the linear scattered signal was computed as

$$G_{lin}(\omega) = \frac{S_{lin,+}(w)}{S_{lin,-}(w)}. \quad (D.38)$$

The detected nonlinear signal can then be computed as

$$D_{nl}(\omega) = S_+(\omega) - G_{lin}(\omega) S_-(\omega). \quad (D.39)$$

The relation between the nonlinear scattered signals is defined in the same way as the nonlinear propagation

$$G_{nl}(\omega) = \frac{S_{nl,+}(w)}{S_{nl,-}(w)}. \quad (D.40)$$

The scattered signals were bandpass filtered with a FIR filter centered around the respective HF pulse frequency with a 100 % bandwidth. The detectable nonlinear signal ratio (DNR) is computed as

$$DNR = \frac{\int d\omega |BP(w) D_{nl}(\omega)|}{2 \int d\omega |BP(w) S_{nl,+}(\omega)|}, \quad (D.41)$$

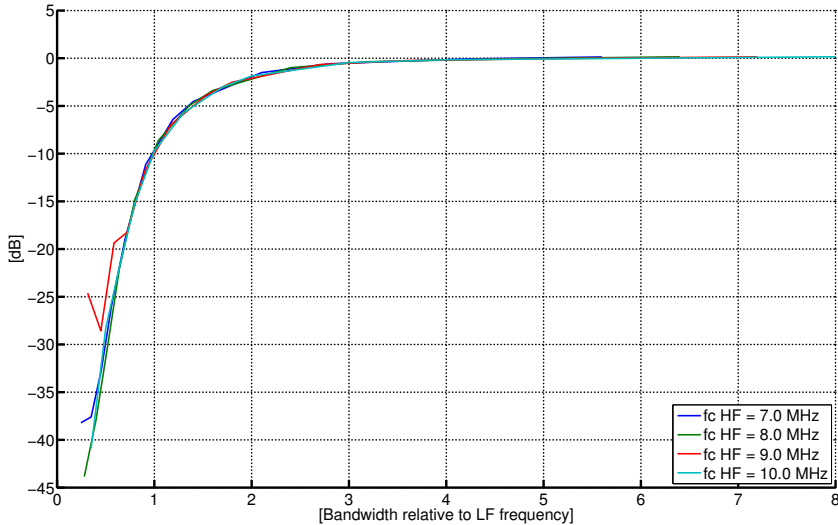


Figure D.1: Detectable nonlinear energy vs bandwidth of the HF pulse relative to the center frequency of the LF pulse.

where $BP(w)$ is the bandpass filter used to remove the low frequency components. The nonlinear to linear scattered signal ratio (NLR) was computed as

$$NLR = \frac{\int d\omega |BP(w) S_{nl,+}(\omega)|}{\int d\omega |BP(w) S_{lin,+}(\omega)|}. \quad (\text{D.42})$$

D.3.4 Results

In Figure D.1 the detectable scattered nonlinear energy relative to the total scattered nonlinear energy (DNR) as a function of absolute bandwidth of the HF pulse relative to the LF pulse is shown. As an example of this bandwidth relationship consider a 10MHz pulse with 6dB relative bandwidth of 30%, which is 3MHz absolute bandwidth. The absolute bandwidth relative to the LF center frequency of 1MHz is then 3. In this way the results for the simulations using different center frequency of the HF can be plotted along a common axis.

In order to determine if the inability to detect nonlinear scattering is due to the actual presence of nonlinear scattering or the ability to differentiate between nonlinear scattering and propagation, it is of interest to investigate the strength of the nonlinear vs linear scattering as a function of the bandwidth. In Figure D.2 the nonlinear scattered energy relative to the linear scattered energy is shown (NLR). The values in Figure D.2 are normalized to the HF bandwidth with the maximum value for each HF frequency, as it is the relative level of NLR between the different bandwidths which is of interest and not the absolute amplitude difference between the nonlinear and linear scattering. The absolute level of nonlinear to linear scattering is dependent on the

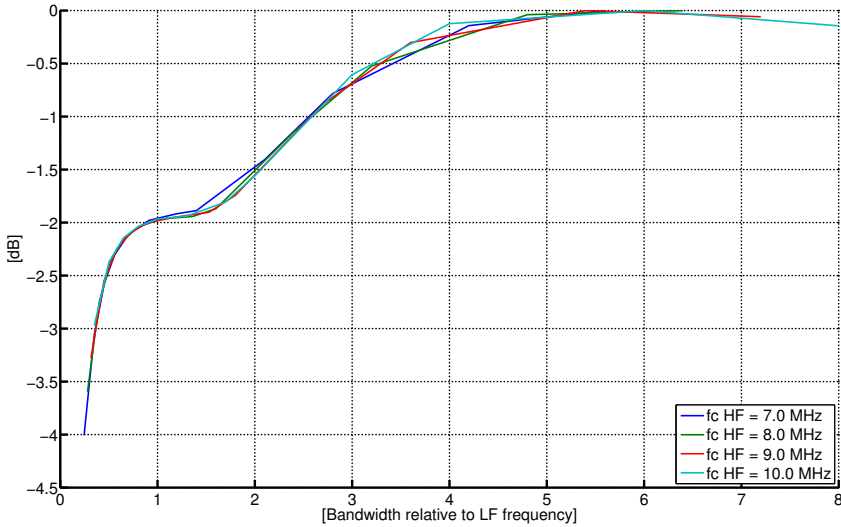


Figure D.2: Scattered nonlinear energy relative to scattered linear energy

actual scatterer and the surrounding medium.

As an example case, the amplitude spectrum of the nonlinear detection signal, the nonlinear scattered signal and the linear scattered signal from a non-manipulated pulse, is shown in Figure D.3 and D.4, for 3.5% and 10% HF bandwidths respectively. The center frequency of the HF pulse is 10MHz for the two cases, which gives a HF bandwidth to LF center frequency of 0.5 and 1 respectively.

In order to detect nonlinear scattering the difference in nonlinear propagation between the positive and negative manipulated pulse must be different than the difference in the nonlinear scattered signal, *i.e.* the relations computed according to Equation (D.38) and (D.40) must be different. The phase difference between the accumulated nonlinear propagation effects, computed according to Equation (D.38), and the nonlinear scattering effect (D.40) is shown in Figure D.5 for four different bandwidths using a center frequency of 10MHz for the HF. The difference in amplitude between the two relations is shown in Figure D.6.

D.3.5 Discussion

From the level of detectable nonlinear scattering shown in Figure D.1, it is seen that as the bandwidth of the HF pulse increases, so does the level of detected nonlinear scattered energy. When the -6dB absolute bandwidth of the HF pulse is greater than two times the center frequency of the LF pulse, the nonlinear scattering can be well separated from the linear scattering if the nonlinear propagation can be adequately corrected for. Increasing the bandwidth above two times the center frequency of the LF pulse gives little gain in detection, but will improve radial resolution.

Even though the -6dB limits of the frequency bands does not overlap, there will

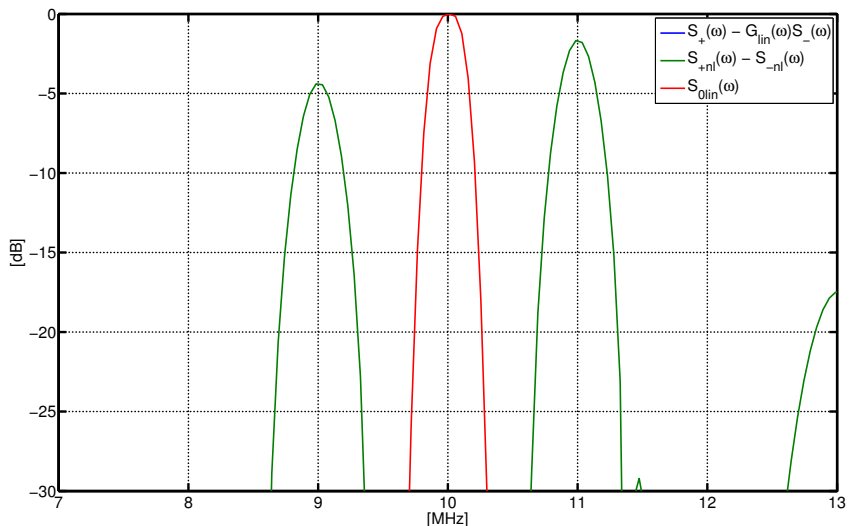


Figure D.3: Spectrums for the detections signals. The center frequency of the HF pulse is 10MHz and the -6dB bandwidth is 3.5%, which is a relative bandwidth of 0.35 to the center frequency of the LF pulse. The propagation distance is 20mm.

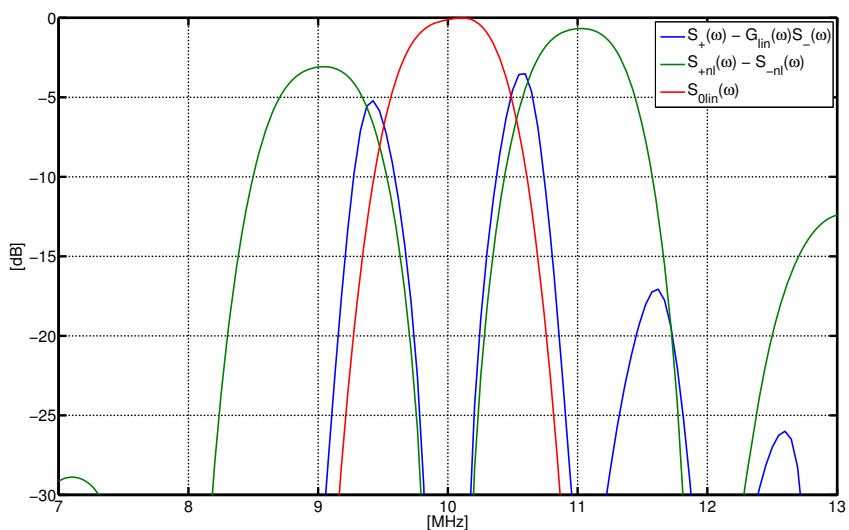


Figure D.4: Spectrums for the detections signals. The center frequency of the HF pulse is 10MHz and the -6dB bandwidth is 10%, which is a relative bandwidth of 1.0 to the center frequency of the LF pulse. The propagation distance is 20mm.

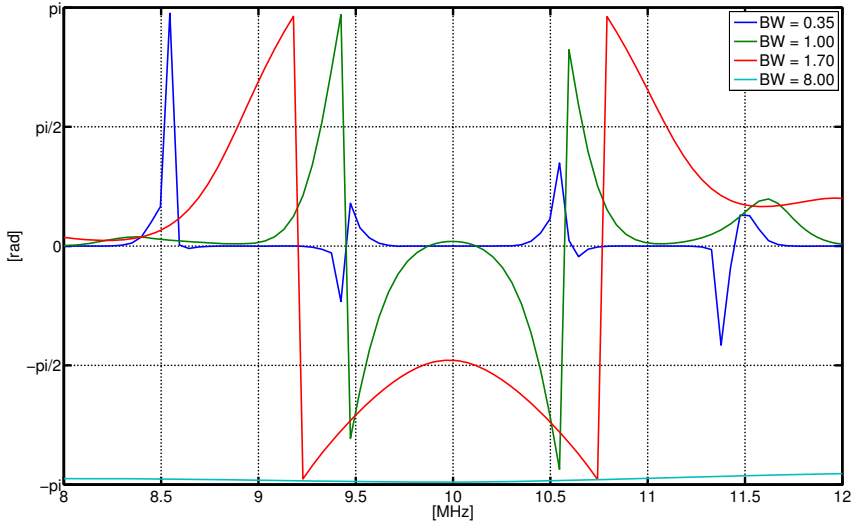


Figure D.5: Phase difference between the nonlinear scattering and nonlinear accumulated propagation at $z=20$ mm.

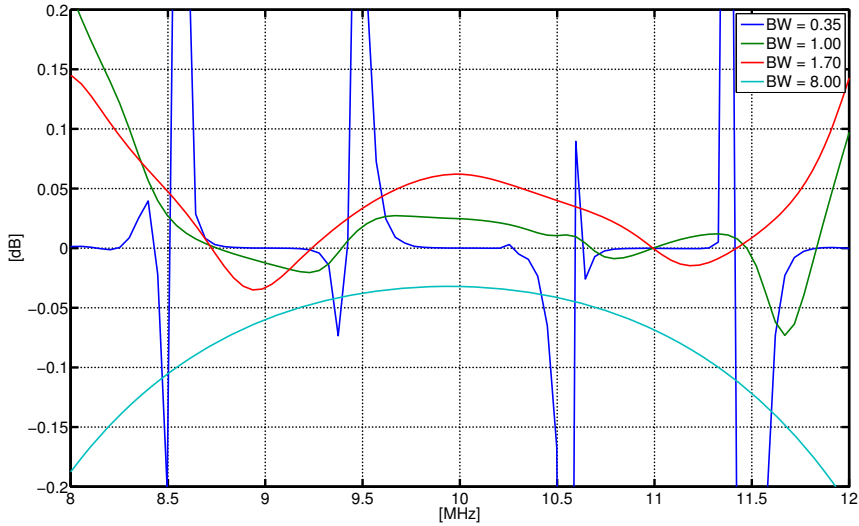


Figure D.6: The amplitude of the relation between the nonlinear scattered signal as defined by (D.40)

still be some degree of overlap at frequencies of low amplitude. There is thus no clear threshold on the bandwidth where the nonlinear scattering can be detected. But as the -6dB bandwidth of the HF becomes less than half of the center frequency of the LF, there is no significant detection of nonlinear scattering.

It should also be noted that the detection curves for all frequency relations are more or less identical. This means that there the ability to detect nonlinear scattering is not related to the frequency relationship but to the absolute bandwidth of the HF pulse relative to the center frequency of the LF pulse.

From the relative nonlinear to linear scattering energy (NLR) shown in Figure D.2, it is seen that the nonlinear scattering is indeed present for all bandwidths, but the problem is that of separating it from the nonlinear propagation.

As shown in Figure D.1, the nonlinear scattering is detectable when HF bandwidth relative to the center frequency increases above one. This means that the generated bands at the sum and difference frequencies overlaps with the fundamental band. This fact is seen clearly in Figure D.4 where the -6dB bandwidth of the HF relative to the center frequency of the LF pulse is 1. The energy of the detectable nonlinear signal lies in the intersection of the sum and difference bands, at 9 and 11 MHz, and the fundamental band at 10MHz. For a HF bandwidth relative to the LF center frequency of 0.35, shown in Figure D.3, there is no overlap of the bands down to -30 dB and from Figure D.1, it is seen that the nonlinear signal cannot be detected.

The signal components generated at the sum and difference band follows the polarity of the LF pulse when the HF pulse is centered at the peak or trough of the LF. When the sum and difference bands does not overlap with the fundamental band, the nonlinear scattered signal is not separable from the linear scattering, *i.e.* the accumulated nonlinear propagation is equal to the local nonlinear scattering. Specifically the phase of the relations defined in Equation (D.38) and (D.40) must be different in order for the nonlinear scattering to be detected. In Figure D.5 the phase difference between these two relations are shown for HF bandwidths relative to the LF center frequency of 0.35, 1.0, 1.7 and 8.0. For the bandwidth relation of 0.35 there is, as shown in Figure D.3, no overlap between the sum and difference bands and the fundamental band, and the phase difference is approximately zero, *i.e.* there is no difference between the accumulated nonlinear propagation and the local nonlinear scattering.

As the bandwidth of the HF increases, the phase difference increases which makes the nonlinear scattering detectable. For a bandwidth relation of 8.0, one can see that there is approximately π phase difference, which indicates a switch in polarity. This means that the sum and difference band overlaps with the fundamental band in such a way that the accumulated nonlinear propagation is no longer only a generation of signal components in the sum and difference bands with polarity following the LF pulse polarity, but a more complex interaction between the fundamental band and and sum and difference bands, while the local nonlinear scattering generates signal components with polarity following the LF pulse.

From Figure D.6 it is seen that there is little difference in amplitude of the relations given in Equations (D.38) and (D.40), so the ability to detect the nonlinear scattering lies mainly in the differences in the phase of these two relations.

D.3.6 Conclusion

In this section it is shown that nonlinear scattering can be differentiated from the nonlinear propagation effects when the bandwidth of the HF pulse is larger than the center frequency of the LF pulse. In the time domain this corresponds to the pulse length of the HF being less than the period of the LF pulse. The nonlinear scattering and accumulation of nonlinear propagation are equal processes and the nonlinear interaction between the LF and HF pulse generates signal components at the sum and difference frequencies of the LF and HF, and these signal components has the same polarity as the LF pulse. When the absolute bandwidth of the HF increases above the center frequency of the LF, the sum and difference bands overlaps with the fundamental band and the accumulated nonlinear propagation becomes different than the local nonlinear scattering which makes the to effects separable.

D.4 Effect of beamforming parameters on accuracy of nonlinear propagation correction

D.4.1 Introduction

In Section D.3 it is shown that the nonlinear scattering can be separated from the nonlinear propagation if the bandwidth of the HF pulse is larger than the center frequency of the LF. But even though this bandwidth relation is satisfied, the nonlinear propagation must be estimated and corrected for in order to detect the nonlinear scattering.

In Section D.2.5 a method for estimating the nonlinear propagation is presented. The method is based on finding the filter which minimizes the sum of squared differences between the received signal from the positive and negative manipulated pulses over a region in the image. Using this method, the on average maximum achievable level of suppression is limited by the correlation between the positive and negative manipulated pulses over the averaging region. As noted in Section D.2.5, in order to achieve optimal suppression, the relation between the positive and negative manipulated wave field should be spatially invariant across the receive beam. One way to achieve this is to make the transmitted HF wave field homogenous across the receive beam.

In this section, the effect of HF f-number and aperture size fraction between the HF and LF in the relation to the maximum achievable suppression of linear scattering is investigated for an annular array. In addition a simulation based on the design of a prototype dual-frequency band linear array is presented in order to investigate what is achievable with the currently available equipment.

D.4.2 Simulations

In order to investigate the effect of beamforming parameters on the performance measure given in Equation (D.23), simulations using an annular array setup was used.

The beamforming parameters investigated are the relative size between the HF and LF apertures and the size of the HF aperture.

The simulations involves two steps; First the forward propagated wave fields are simulated using Abersim [12]. Then the spatial impulse responses for the receive beam are calculated for each position and the receive wave field computed as

$$U_{+/-,r}(r_{\perp}, z; \omega) = H_r(r_{\perp}, z; \omega; F_z) U_{+/-,t}(r_{\perp}, z; \omega), \quad (\text{D.43})$$

where $H_r(r_{\perp}, z; \omega)$ is the spatial frequency response for the receive beam focused at depth F_z , and $U_{+/-,t}(r_{\perp}, z; \omega)$ is the Fourier transform of the forward propagated wave field. For an annular array, the spatial frequency response is given as [6]

$$H\left(r_{\perp}, z; k = \frac{\omega}{c_0}; F_z\right) = \frac{a^2 e^{-2kr}}{2r} \frac{2J_1(kar_{\perp}/F_z)}{kar_{\perp}/F_z} \quad (\text{D.44})$$

where $r = \sqrt{z^2 + r_{\perp}^2}$, $a = \frac{D}{2}$ is the aperture radius, and J_1 is the first order Bessel function [13].

For all the simulation setups, the center frequencies are set to 1 and 8 MHz for the LF and HF pulses respectively, while the relative bandwidth is 70% for both pulses. The pulses where propagated until 30 mm and the temporal sampling frequency was set to 100 MHz, while the spatial sampling interval was 50 μm . The geometrical focus was set to 20 mm for both the LF and HF.

In the first set of simulations, the effect of HF f-number on the level of suppression is investigated. The HF transmit beam f-number is varied over the range 2.0 to 4.5 at steps of 0.5. The size of the LF aperture is chosen in order to make the diffraction for the LF and HF beams as equal as possible. This implies that the Fresnel-number, which is defined as [6]

$$SN = \frac{4F_z\lambda}{D^2},$$

where F_z is the focal depth, λ is the wavelength and D is the aperture size, should be equal for the two beams. Setting the Fresnel numbers to be equal gives the following size relationship between the LF and HF apertures

$$D_{LF} = \sqrt{\frac{f_{HF}}{f_{LF}}} D_{HF}.$$

For the frequencies chosen here, the relative aperture size which yields equal Fresnel-numbers is ~ 2.8 . By setting the Fresnel-numbers equal, the depth at which the geometric beam definition and the diffraction cone intersects, becomes equal as well [6]. Using this size relationship, the transmit f-numbers for the LF for the first set of simulations is [0.53, 0.71, 0.88, 1.06, 1.24, 1.41].

For the second set of simulations, the f-number of the LF is fixed to 1.1, while the HF f-number is varied over the range 1.5 to 4.0 at steps of 0.5. The relative aperture sizes then becomes [1.4, 1.8, 2.3, 2.7, 3.2, 3.6]. This set of simulations investigates the effect of relative size of the LF and HF apertures on the level of signal suppression.

For all the simulations in the first and second set, weak apodization is applied in using a tukey window with $\alpha = 0.1$ to suppress the strongest edge waves. On receive, dynamic focusing is used for all simulations, *i.e.* $F_z = z$, and the f-number is set to 1.5. The transmitted pressure for the LF pulse was calibrated in order for the LF pressure to be 0.5 MPa at 20 mm for all setups, and the phase relation between the HF and LF at transmit was calibrated in order for the HF to be centered at the peak of the LF in 20 mm.

For the circular focused aperture, the pulse at the geometrical focus F , is the spatial derivative of the excitation pulse $f(t)$ [6]

$$\hat{p}(\omega, F) = i\omega \hat{f}(\omega) \rho U_n \frac{e^{ikF}}{2\pi F} A, \quad (\text{D.45})$$

where $k = \frac{\omega}{c}$ is the wave number, U_n is the normal velocity at the transducer, and A is the vibrating surface area. That is, diffraction will produce a phase shift of $\lambda/4$ from the transducer to the focus. In order to have the HF pulse at the peak or trough of the LF at the focus, the HF pulse must be centered at the zero crossing of the LF at transmit. This also means that the phase relationship between the HF and LF will vary with depth, and this variation will be a function of the chosen LF aperture size. For a large aperture, most of the phase shift will occur close to the focus, while it will for a small aperture start at and earlier depth.

In order to analyze the effect of beamforming parameters, annular arrays are convenient, but most modern scanners today use linear arrays. A dual-frequency band linear array has been designed where the HF and LF part are placed behind each other in a stack [14]. The array is manufactured by Vermon (Tours, France). The center frequency of the array is 1 and 8 MHz for the HF and LF part respectively. The elevation aperture is 4 mm for the HF and has a fixed focus of 20 mm using an acoustic lens. The LF elevation aperture is 8 mm, where the central 4 mm has a fixed focus of 20 mm, while the outer 2 mm on each side is unfocused. If the acoustic lens should have covered the whole LF aperture, the lens covering the central part would become thick and introduced a substantial loss in the HF beam. To demonstrate the difference between an annular and linear array, one simulation using an azimuth F-number of 3 and 1.1 for the HF and LF apertures respectively has been performed. The LF transmit pressure and the phase relationship between the HF and LF is adjusted in the same way as for the annular simulations. For computation of the spatial frequency responses of the receive beam, Field II [15] was used.

D.4.3 Processing

All processing was done using MATLAB (The Mathworks, Massachusetts, USA). The forward propagated pulses were filtered with a 100 tap bandpass filter with cutoff frequencies [5, 15] MHz and [0.1, 2] MHz to extract the HF and LF pulses respectively.

For comparing the different transmit beams setups, the correlation coefficient de-

finned in Equation (D.25) together with the expression in Equation (D.32)

$$\rho_{+/-}(z, \omega) = \frac{\langle Y_+(z, \omega) Y_-^*(z, \omega) \rangle}{\sqrt{\langle |Y_+(z, \omega)|^2 \rangle \langle |Y_-^*(z, \omega)|^2 \rangle}} \quad (\text{D.46})$$

where the ensemble average is computed over the plane at depth z , *i.e.* the scatterers are assumed to be in a plane at depth z as discussed in relation to Equation (D.16).

The filter for correcting for the nonlinear propagation is estimated as

$$\hat{G}(z; \omega) = \frac{\langle Y_+(z, \omega) Y_-^*(z, \omega) \rangle}{\langle |Y_-^*(z, \omega)|^2 \rangle}. \quad (\text{D.47})$$

The average signal suppression was then computed as

$$\text{SUP} = \frac{\int_{-\infty}^{\infty} d\omega \langle Y_+(z, \omega) - \hat{G}(z; \omega) Y_-(z, \omega) \rangle}{\int_{-\infty}^{\infty} d\omega \left[\sqrt{\langle |Y_+^*(z, \omega)|^2 \rangle \langle |Y_-^*(z, \omega)|^2 \rangle} \right]}. \quad (\text{D.48})$$

For the linear array simulation, the correlation coefficient and average signal suppression are computed along the azimuth and elevation axis only. The azimuth and elevation plane can be analyzed separately by letting the integral in (D.32) run over the corresponding coordinate.

The experienced LF manipulation pressure by the HF pulse on the beam axis, $r_{\perp} = 0$, was computed by taking the weighted average of the LF pressure over the HF pulse using the envelope of the HF pulse as the weight

$$pe_{LF}(z) = \frac{\int_{-\infty}^{\infty} dt \text{env}_{HF}(0, z, t) p_{LF}(0, z, t)}{\int_{-\infty}^{\infty} dt \text{env}_{HF}(0, z, t)}, \quad (\text{D.49})$$

where the HF envelope, env_{HF} is computed by taking the absolute value of the analytic signal which was computed using the MATLAB Hilbert transform.

D.4.4 Results

In Figure D.7 the value of the correlation coefficient at the center frequency of the HF pulse is shown. The value is plotted as $10 \log_{10} \left(1 - |\rho_{+/-}(\omega)|^2 \right)$ in order to show what level of suppression the correlation value corresponds to, as described in Section D.2.5.

While the the correlation coefficient in Figure D.7 yields the suppression at the center frequency, Figure D.8 shows the average level of signal suppression over the whole frequency band, computed according to Equation (D.48).

The interaction between the HF and LF pulse generates the nonlinear scattering, and the strength of the nonlinear scattered signal is proportional to the experienced LF

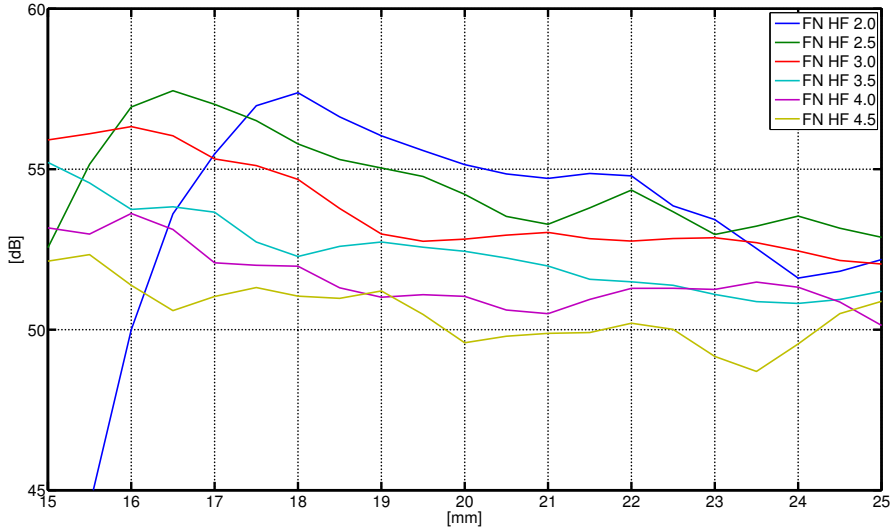


Figure D.7: Correlation coefficient at the center frequency for the first set of simulations, where the size relationship between the HF and LF is chosen in order to get equal Fresnel-numbers for the HF and LF. Plotted as $10 \log_{10} \left(1 - |\rho_{+/-}(\omega)|^2 \right)$.

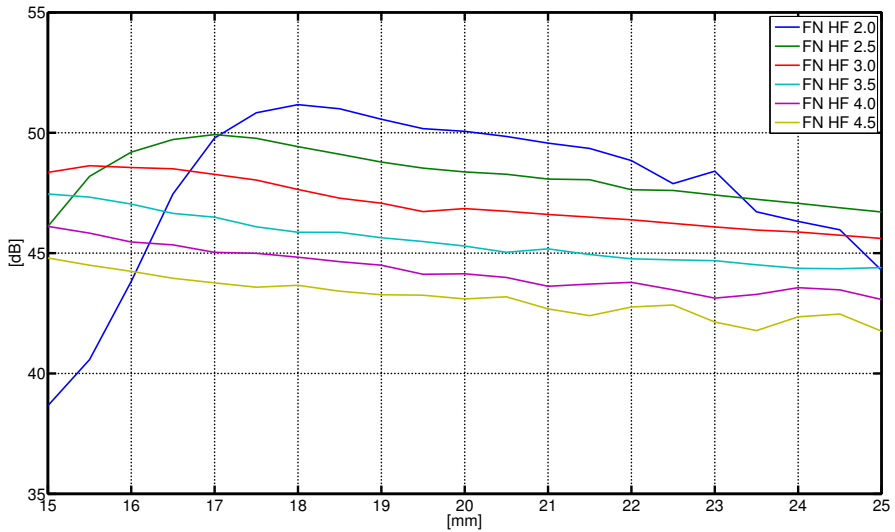


Figure D.8: Suppression of signal using the average filter for the first set of simulations, where the size relationship between the HF and LF is chosen in order to get equal Fresnel-numbers for the HF and LF.

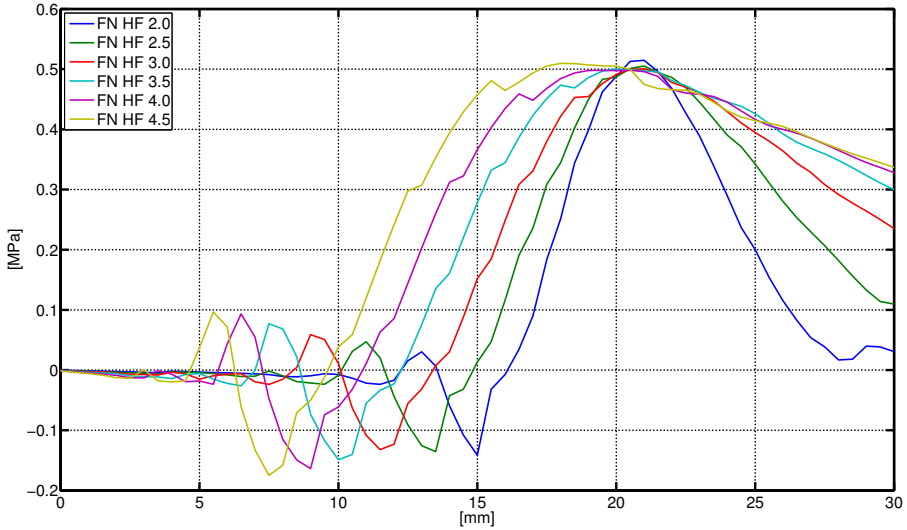


Figure D.9: Manipulation pressure experienced by the HF pulse for the first set of simulations, where the size relationship between the HF and LF is chosen in order to get equal Fresnel-numbers for the HF and LF.

manipulation pressure. The experienced LF pressure by the HF pulse thus indicates the sensitivity to nonlinear scattering and is shown in Figure D.9. The experienced LF pressure also shows the manipulation of the forward propagating pulse which can be an indication of the amount of accumulated nonlinear propagation effects.

For the first set of simulations, the apertures of the LF and HF beam is chosen in order for the diffraction of the beams to be as equal as possible, *i.e.* the Fresnel-numbers are set to be equal. Equal diffraction should produce equal axis profiles and the axis profiles for the HF and LF are shown in Figure D.10.

In the second set of simulations the F-number of the LF beam is held constant at 1.1 while the f-number for the HF beam is varied over 1.5-4.0 which yields aperture size relationships of [1.8, 2.3, 2.7, 3.2, 3.6]. These simulations were performed in order to compare the level of suppression for different aperture size relationships. The level of suppression at the center frequency given by the correlation coefficient is plotted in Figure D.11, while the total level of suppression over the whole frequency band of the HF is plotted in Figure D.12. The axis profiles for the different HF beams and the LF beam are shown in the upper and lower panel respectively of Figure D.13.

For the linear array simulations, the level of suppression at the center frequency and the whole frequency band is shown in Figure D.14 and D.15 respectively. The figures show the values for the total field and for the elevation and azimuth axis separately. This separation is made since the apertures are different in the two dimensions and that dynamic focusing is only applied in the azimuth dimension.

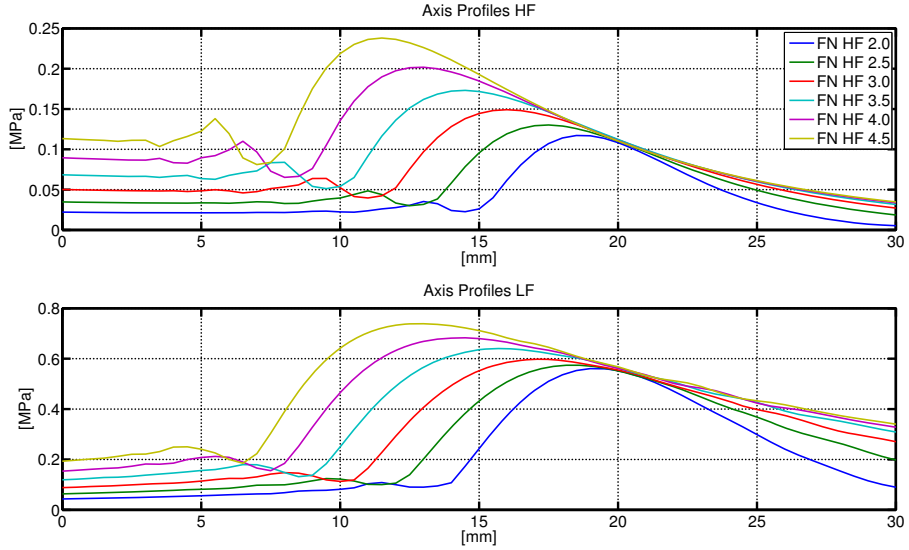


Figure D.10: Axis profiles for the HF (top panel), and LF (bottom panel) for the first set of simulations, where the size relationship between the HF and LF is chosen in order to get equal Fresnel-numbers for the HF and LF.

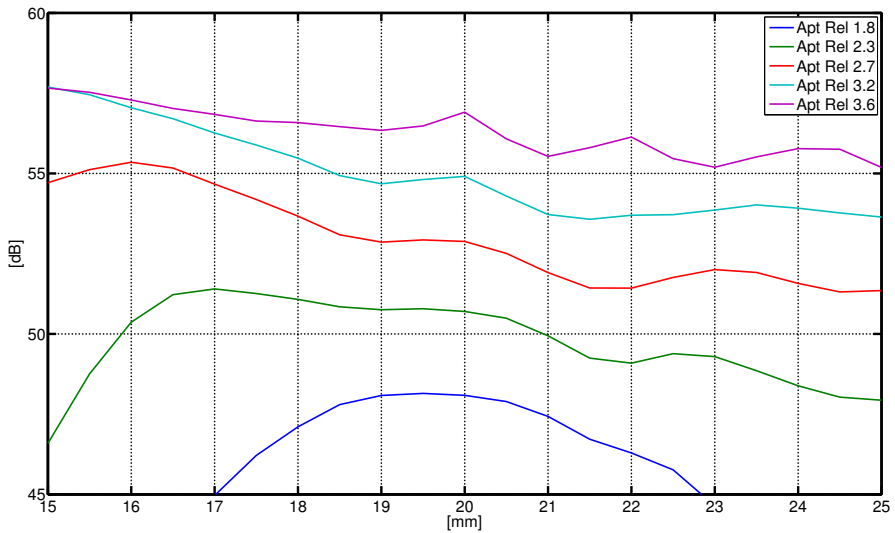


Figure D.11: Correlation coefficient at the center frequency for the second set of simulations, where the LF F-number is held constant while the HF F-number is varied. Plotted as $10 \log_{10} \left(1 - |\rho_{+/-}(\omega)|^2 \right)$.

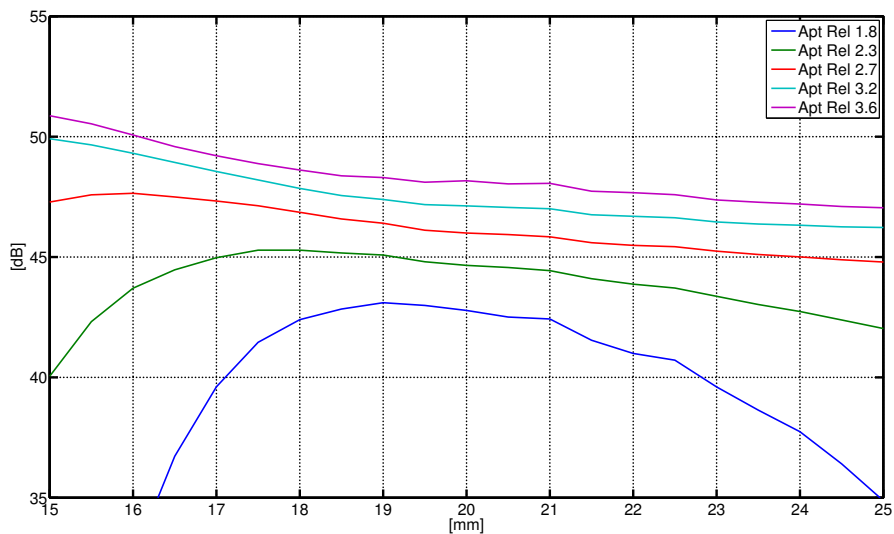


Figure D.12: Suppression of signal using the average filter for the second set of simulations, where the LF F-number is held constant while the HF F-number is varied.

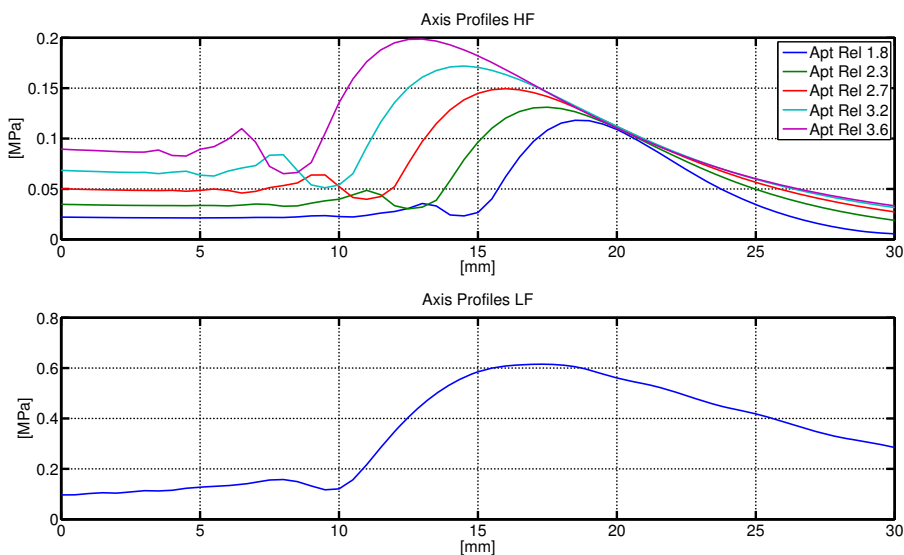


Figure D.13: Axis profiles for the HF (top panel), and LF (bottom panel) for the second set of simulations, where the LF F-number is held constant while the HF F-number is varied.

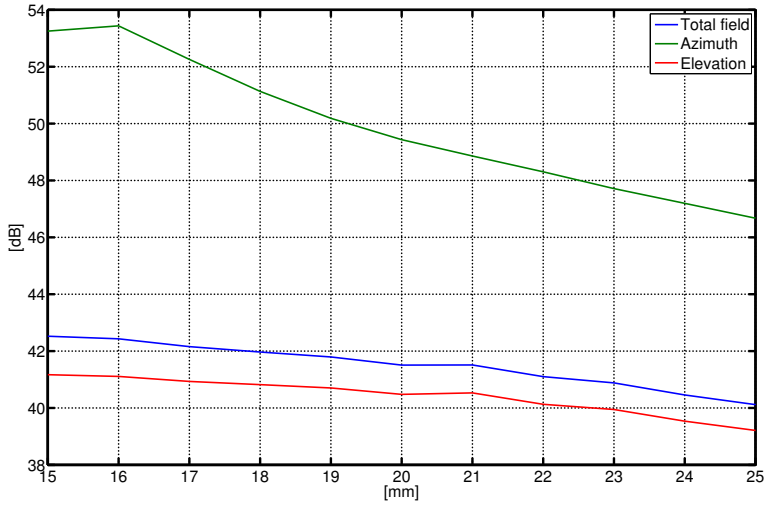


Figure D.14: Correlation coefficient at the center frequency for the linear array simulation. The correlation coefficient is shown separately for the azimuth and elevation direction and for the total field. Plotted as $10 \log_{10} \left(1 - |\rho_{+/-}(\omega)|^2 \right)$.

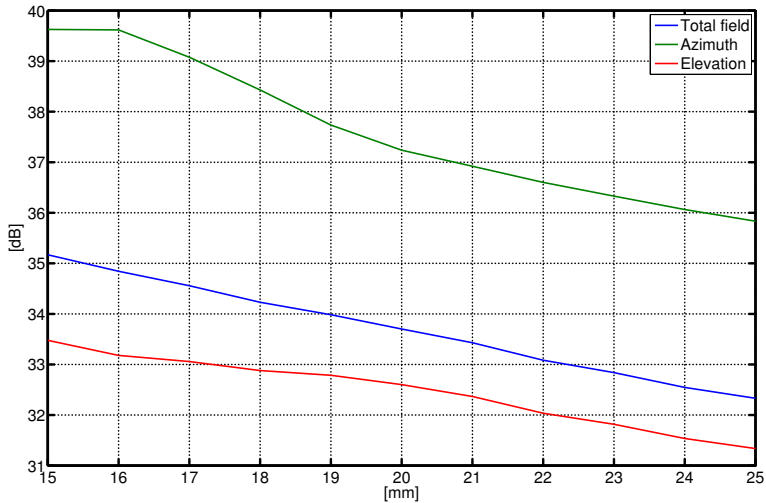


Figure D.15: Suppression of signal using the average filter for the linear array simulation. The suppression is shown separately for the azimuth and elevation direction and for the total field.

D.4.5 Discussion

In the first set of simulations the F-number of the HF was varied over the range 2 to 4.5 and the size of the LF aperture was chosen in order for the Fresnel-numbers of the two beams to be equal. The reasoning behind this is that equal Fresnel-numbers should give equal diffraction, which will produce dual-band frequency beams where the phase fronts of the HF and LF beam are aligned. This should produce a uniform distortion of the HF across the beam and thus produce beams where a high level of suppression of linear scattering can be achieved as discussed in Section D.2.5.

Equal diffraction should produce axis profiles with the same shape. From the axis profiles shown in Figure D.10, this is not exactly achieved. The depth at which the beam reaches maximum intensity is not aligned for the corresponding HF and LF beams, and the HF pressure seems to decrease more rapidly for the HF. This difference can be explained by the difference in attenuation. As attenuation increases close to linearly with frequency, there will be a significant difference in attenuation for the HF and LF using a frequency relation of 1:8. This can be seen by the peaks of the HF occurring at a more shallow depth than for the corresponding LF beam and that the HF pressure decreases more rapidly than the LF. Attenuation will also contribute to a downsliding in frequency, which will also affect the diffraction.

As discussed in relation to signal suppression in Section D.2.5, a narrower beam should provide better signal suppression. This is confirmed by the correlation values in Figure D.7. When decreasing the transmit F-number from 4.5 to 2, the level of signal suppression decreases with ~ 5 dB at the center frequency in the focus, while the total level of suppression increases with ~ 7 dB (Figure D.8). Decreasing the F-number of the HF and thus decreasing the F-number of the LF gives a shorter depth region where the experienced LF pressure is high, which can be seen in Figure D.9. As the nonlinear scattered signal is proportional to the manipulation pressure, a lower F-number on the LF will give a shorter depth region where there is good sensitivity for nonlinear scattering.

To achieve the same experienced LF pressure in the focus for the different aperture sizes, the transmitted LF pressure must increase with increasing f-numbers. Thus for increasing f-numbers, the experienced LF pressure in the near-field will increase and produce more nonlinear propagation effects, which must be estimated and corrected for. A lower f-number of the LF will produce a high experienced manipulation pressure in a small region around the focus depth, while minimizing the propagation effects in the near-field. In order to achieve a large depth region of high sensitivity to nonlinear scattering, several pulses must be transmitted in each scan line direction where the focus depth is changed for each transmission.

In the second set of simulations the F-number of the LF is set constant to 1.1, while the F-number of the HF beam is set to vary over the range 1.5 to 4.0 at steps of 0.5, giving aperture size relationships of [1.8, 2.3, 2.7, 3.2, 3.6]. This is done to investigate the effect of aperture size relationship on the level of suppression and to see if the aperture size relationship which yields equal Fresnel-numbers for the two beams (~ 2.8 for this setting), is optimal.

From Figure D.11 and D.12 it is seen that the level of suppression increases with

increasing size relationship. From the first set of simulations it was shown that the level of suppression increased with decreasing F-number of the HF beam, if the size relationship was kept constant. From these two observations it is noted that increasing the HF aperture, which gives a narrower HF beam, does not provide a higher level of signal suppression unless the LF beam is increased accordingly.

In the first set of simulations the size relationship was chosen to be $\sqrt{\frac{f_{HF}}{f_{LF}}} \approx 2.8$ which yields equal Fresnel-numbers and thus equal diffraction of the two beams. But from Figure D.12 the level of suppression is seen to decrease even when the size relationship increases above 2.8, which indicates that setting the Fresnel-numbers equal is not necessarily the optimal size relationship. As the f-numbers increases, the depth at which the beam is at its narrowest moves closer to the transducer, and from this depth on the beam spreads out and becomes wider. This narrowest point of the beam can thus be seen as a secondary source where the HF beam is transmitted from. This secondary transmit source is unfocused and narrow, which means that the beam spreads out as an approximate spherical wave. If the LF beam is wide compared to the transmitted HF beam, this gives a homogenous HF beam with a close to constant LF pressure over the HF beam, and thus a high level of suppression. The problem of using a small transmit aperture is that the depth at which the beam has its maximum on the axis is moved close to the transducer and the pressure decreases from this depth on, as seen in Figure D.13, which can pose a challenge in relation to SNR.

As discussed in relation to Figure D.10, the diffraction of the two beams are not necessarily, even if the Fresnel-number is set to be equal. The optimal aperture size relationship might thus not be the one that yields equal Fresnel-numbers, which the second set of simulations indicates. If a setup using a finite focus depth is chosen, as in these simulations, it is not well defined what size relationship is the optimal.

In the last simulation a linear array setup which corresponds to an existing prototype probe, has been investigated. The aperture size relationship in the azimuth dimension is chosen to give equal Fresnel-numbers for the HF and LF beams, and the HF F-number is set to 3.0. This aperture setup is comparable to the simulation in the first set where the HF F-number is 3.0. Comparing the correlation coefficient for the azimuth dimension with that of the corresponding simulation for the annular array, it is seen that the level of suppression is about 5 dB higher for the annular array. This can be due to the fact that the sidelobes of a linear array is 4.5 dB higher than that of an annular array [6]. From Figure D.15, the level of suppression in the elevation direction is seen to be ~ 4.5 dB lower than for the azimuth direction. In the elevation direction the HF transmit and receive F-number is 5.0, and there is fixed focus on receive. From the previous discussion for the annular array, a transmit F-number for the HF of 5.0 and using an aperture size relationship of 2, should yield good results but the lack of good receive focusing limits the level of suppression.

Also, for the linear array there is a larger difference in the suppression at the center frequency and the total level of suppression. While it for the annular simulations are in the range 5-6 dB, it is around 12 dB for the annular array. This can be caused by the off axis impulse response of the linear array introducing larger variations over the beam than what is the case for the annular array. The one way side lobe levels for

the annular array is also 4.5 dB lower than that of the annular array, so the off axis variations are not as well suppressed for the linear array case as for the annular array.

D.4.6 Conclusion

In this section the effect of beamforming parameters on the level of suppression of linear scattering has been investigated. The focus of the investigation has been on the relative aperture size relationship between the HF and LF, and the HF transmit beam F-number. As diffraction depends on the size of the aperture and frequency of the transmitted pulse, the size of the apertures for the HF and LF does not necessarily have to be equal in order to achieve a high level of suppression.

Keeping the focus depth constant and increasing the HF aperture while increasing the LF aperture accordingly in order to keep the size relationship constant, shows that the level of suppression increases with increasing aperture. This is due to a narrow HF beam and an LF pressure which is high only in a short depth region around the focus. But increasing the HF aperture to get a narrower beam without increasing the LF aperture does not improve the level of suppression, which shows that the size relationship is crucial for achieving good suppression.

The hypothesis that beams with equal Fresnel-numbers would give optimal suppression was not true, the level of suppression continued to increase with increasing relative aperture size and was not bounded by the relationship $\sqrt{\frac{f_{HF}}{f_{LF}}}$. By increasing the F-number of the HF, the depth at which the beam is the narrowest moves closer to the transducer, and from this depth on the beam spreads out in an approximately spherical wave. If the LF beam is wider than the HF beam, the LF pressure will vary little over the HF beam, producing a homogenous distortion over the beam, and thus good suppression of linear scattering using the proposed method for estimation of nonlinear propagation. Attenuation will effect the HF and LF beam differently since attenuation increases with frequency which will alter the diffraction patterns of the two beams, which can also be a reason why setting the Fresnel-numbers equal did not provide the optimal setting.

From the simulation study presented here it should be clear that diffraction poses a challenge in designing transmit beams for dual-frequency band imaging. When using a large separation in frequency between the LF and HF, it is difficult to design beam where the diffraction of the two beams are equal. Different diffraction will introduce a varying LF pressure over the HF beam which can be seen as a kind of aberration. This aberration will give differences in accumulated nonlinear propagation over the beam and introduce inhomogeneities over the HF beam. When altering the transmit phase relationship between LF and HF, the HF beam will be affected by the nonlinear propagation effects in a different way thus changing the diffraction of the positive and negatively manipulated HF pulse.

In order to satisfy the Schwarz inequality in Equation (D.33), the relationship between the positive and negative manipulated pulse must be constant over the beam. If this relationship varies over the beam, the optimal correction filter for each realization of the received signal will be dependent on the actual scatterer distribution within the

beam. The proposed method for estimating the correction filter finds the on average optimal filter, which is not necessarily optimal for each realization of the received signal. With the requirement of more than 30 dB suppression of linear scattering the proposed method is highly sensitive to variations of the relationship between the positive and negative manipulated pulse over the beam.

In Section D.2.3 it was indicated that in order to detect the nonlinear scattering the linear scattering would have to be suppressed at least 30 dB. From the results presented here, this is possible using an annular array, where the suppression of linear scattering of around 45 dB is achieved. For the linear array, the level of suppression is approximately 32 dB in the geometrical focus. This is at the limit of what is needed in order to detect nonlinear scattering. In the practical case where there exist aberrations and reverberations, detection of nonlinear scattering with the setup presented here may not be possible.

References

- [1] T. Nagashima, H. Hashimoto, K. Oshida, S. Nakano, N. Tanabe, T. Nikaido, K. Koda, and M. Miyazaki, “Ultrasound demonstration of mammographically detected microcalcifications in patients with ductal carcinoma in situ of the breast,” *Breast Cancer*, vol. 12, no. 3, pp. 216–220, 2005.
- [2] R. J. Eckersley, C. T. Chin, and P. N. Burns, “Optimising phase and amplitude modulation schemes for imaging microbubble contrast agents at low acoustic power,” *Ultrasound in Medicine & Biology*, vol. 31, pp. 213–219, Feb. 2005. PMID: 15708461.
- [3] D. Simpson and P. Burns, “Pulse inversion doppler: a new method for detecting nonlinear echoes from microbubble contrast agents,” in *Ultrasonics Symposium, 1997. Proceedings., 1997 IEEE*, vol. 2, pp. 1597–1600 vol.2, 1997.
- [4] B. Angelsen, *Ultrasound imaging. Waves, signals and signal processing Vol II*. Trondheim: Emantec, 2000.
- [5] R. Hansen, S. Masoy, T. F. Johansen, and B. A. Angelsen, “Utilizing dual frequency band transmit pulse complexes in medical ultrasound imaging,” *The Journal of the Acoustical Society of America*, vol. 127, pp. 579–587, Jan. 2010.
- [6] B. Angelsen, *Ultrasound imaging. Waves, signals and signal processing Vol I*. Trondheim: Emantec, 2000.
- [7] M. Anderson, “A 2D nonlinear wave propagation solver written in open-source MATLAB code,” in *Ultrasonics Symposium, 2000 IEEE*, vol. 2, pp. 1351–1354 vol.2, 2000.
- [8] T. Varslot and G. Taraldsen, “Computer simulation of forward wave propagation in soft tissue,” *Ultrasonics, Ferroelectrics and Frequency Control, IEEE Transactions on*, vol. 52, no. 9, pp. 1473–1482, 2005.
- [9] D. E. Grenoble, J. L. Katz, K. L. Dunn, R. S. Gilmore, and K. L. Murty, “The elastic properties of hard tissues and apatites,” *Journal of Biomedical Materials Research*, vol. 6, no. 3, pp. 221–233, 1972.

- [10] A. Fandos-Morera, M. Prats-Esteve, J. M. Tura-Soteras, and A. Traveria-Cros, "Breast tumors: composition of microcalcifications.," *Radiology*, vol. 169, pp. 325–327, Nov. 1988.
- [11] I. S. Gradshteyn, I. M. Ryzhik, A. Jeffrey, and D. Zwillinger, *Table of integrals, series and products*. Academic Press, 2007.
- [12] D. of Circulation, N. U. o. S. Medical Imaging, and T. (NTNU), "Abersim - ultrasound simulation software." <http://www.ntnu.no/isb/abersim>.
- [13] M. Abramowitz and I. A. Stegun, *Handbook of mathematical functions with formulas, graphs, and mathematical tables*. Courier Dover Publications, 1964.
- [14] T. Johansen, J. Deibele, S. Måsøy, R. Hansen, and B. Angelsen, "Design and test of a Dual-Layer, Dual-Frequency SURF array," *Proceedings of the 31st Scandinavian Symposium on Physical Acoustics*, vol. 31, 2001.
- [15] J. Jensen and N. Svendsen, "Calculation of pressure fields from arbitrarily shaped, apodized, and excited ultrasound transducers," *Ultrasonics, Ferroelectrics and Frequency Control, IEEE Transactions on*, vol. 39, no. 2, pp. 262–267, 1992.